Title
Multiscale Modeling of Dislocation-Based Crystal Plasticity within a Multiphysics Framework

Author
Huang, Yue

Publication Date
2018

UNIVERSITY OF CALIFORNIA
Los Angeles

Multiscale Modeling of Dislocation-Based Crystal Plasticity within a Multiphysics Framework

A dissertation submitted in partial satisfaction
of the requirements for the degree
Doctor of Philosophy in Mechanical Engineering

by

Yue Huang

2018

ABSTRACT OF THE DISSERTATION

Multiscale Modeling of Dislocation-Based Crystal Plasticity within a Multiphysics Framework

by

Yue Huang
Doctor of Philosophy in Mechanical Engineering
University of California, Los Angeles, 2018
Professor Nasr M. Ghoniem, Chair

Simulation-based design and design-by-analysis methods are important tools in the development of modern complex systems due to their impact on attaining shorter manufacturing and construction cycles and lower testing cost. The research in this thesis is devoted to the development of a multiphysics-multiscale FEM framework to provide precise analysis of complex energy conversion structural components with relatively high computational efficiency. The main focus is on applications where the incident heat flux on component surfaces is extreme. This motivation leads to four major contributions. Firstly, various widely-used multiphysics simulation strategies and algorithms are assessed, and recommendations on how to select a suitable multiphysics modeling strategy are made. Fully-coupled 3D CFD and heat transfer simulations are found to be necessary in forced-convection cooling in channels under single-sided heat load. Secondly, two multiscale methods for coupling heterogeneous constitutive models in coupled global-local domains are proposed for self-consistent structural analysis. The first is based on the Hu-Washizu variational principle that leads to accurate matching of all stress components across a global-local interface. This matching cannot be achieved by conventional sub-modeling methods. The second method couples the crystal plasticity framework with conventional continuum plasticity by matching the plastic slip at the coupling interface. These two methods have been shown to be accurate and numerically convergent. The superiority of the proposed approaches is demonstrated by comparison to three conventional sub-modeling methods from the literature. Thirdly, an advanced dislocation-based crystal plasticity model has been developed. The model is sensitive to the material microstructure, and can be readily incorporated into the multiscale framework. The model is validated by micro-indentation experiments, where the force-displacement curve, lattice rotations, and dislocation patterns obtained from experiment are quantitatively reproduced. The developed comprehensive multiphysics-multiscale modeling framework has been successfully implemented in the design of three real-life critical components for energy conversion in fusion energy power plants, demonstrating the practical feasibility of the framework.

The dissertation of Yue Huang is approved.

Vijay Gupta

Christopher S. Lynch

Jaime Marian

Giacomo Po

Nasr M. Ghoniem, Committee Chair

University of California, Los Angeles

2018

To my mother Bin,
who has always loved me unconditionally,
and taught me to work hard for the things that I aspire to achieve.

TABLE OF CONTENTS

LIST OF FIGURES

LIST OF TABLES

ACKNOWLEDGMENTS

I would like to thank Professor Ghoniem for his generous support and insightful guidance during my research. I also would like to extend my appreciation to other members on my doctoral committee, Professor V. Gupta, Professor J. Marian, the late Professor W. Klug, and Professor C. S. Lynch, for their efforts and time to participate in my oral exam and final defense. My thanks also are due to Dr. Giacomo Po for his generous help and guidance on my research. Finally, I would like to express my appreciation to members of the UCLA Matrix Lab: John, Ben, David, Chris, Andrew, Edward, Yinan, Mohammad, Arian, Warren and Dylan, for the great time we spent together.

VITA

1991	Born, Nanjing, Jiangsu, China.
2009–2013	B.S. (Mechanical Engineering), Nanjing University of Science and Technology.
2013-2015	M.S. (Mechanical Engineering and Aerospace), UCLA.

PUBLICATIONS

1. Huang, Yue, M. S. Tillack, and N. M. Ghoniem. ”Tungsten monoblock concepts for the Fusion Nuclear Science Facility (FNSF) first wall and divertor.” *Fusion Engineering and Design* (2017).
2. Huang, Yue, M. S. Tillack, N. M. Ghoniem, J. P. Blanchard, L. A. El-Guebaly, and C. E. Kessel. ”Multiphysics modeling of the FW/Blanket of the US fusion nuclear science facility (FNSF).” *Fusion Engineering and Design* (2017).
3. Rivera, David, Y. Huang, G. Po, and N. M. Ghoniem. ”A dislocation-based crystal viscoplasticity model with application to micro-engineered plasma-facing materials.” *Journal of Nuclear Materials* 485 (2017): 231-242.
4. Huang, Yue, F. Cismondi, E. Diegele, G. Federici, A. Del Nevo, F. Moroc, N. M. Ghoniem. ”Thermo-structural Design of the European DEMO Water-Cooled Blanket with a Multiscale-Multiphysics Framework.” submitted to *Fusion Engineering and Design* (2018).
5. Po, Giacomo, Y. Huang, N. M. Ghoniem, ”A continuum dislocation model of wedge microindentation of single crystals.” submitted to *Int. J. Plasticity* (2018).

CHAPTER 1

Introduction and Thesis Objectives

Modern approaches to the design and analysis of complex engineering components are converging towards utilization of massive computer simulations of entire components or engineering systems before final production. The near-real computer simulations afforded by high fidelity physics and robust computational methodologies are playing increasingly important roles in shortening the component development cycle, reducing the cost of expensive testing especially in severe or prohibitive environments, and helping in the production of more reliable components. Such astounding advances have not been possible only a few years ago. Physics-based approaches to design and analysis are expected to continue to grow for the foreseeable future, and will only accelerate as more understanding of coupled physics simulations improves.

Simultaneously with the advent of multi-phyiscs modeling capabilities, greater demands on materials performance necessitated more accurate descriptions of failure phenomena. Within the framework of multi-physics, a highly stressed component may suffer significant deformation beyond the elastic regime that can result in reduced reliability and early failure. For these reasons, recent efforts have focused on including information on the microstructure of the material in the analysis of its mechanical state under thermal and mechanical loads. These efforts have culminated in the development of the so called ”multi-scale” modeling strategy, where information gained at lower length scales are incorporated into higher length scales for more accurate representation. For example, a very large structure may be mostly operating in a safe fashion, with the exception of a few small zones, where the stress may build up resulting in plastic deformation and fracture. Since there are inherent variabilities in the material microstructure (grain size, distribution of grain orientations, and the dislocation microstructure, failure may be difficult to predict with certainty if one utilizes a macroscopic theory that ignore the microstructure completely. Therefore, significant efforts are being made in recent years in the arena of "multi-scale modeling," with various techniques and strategies.

1.1 Multiphysics of High Heat Flux Components

We can describe what happens in the world using sets of physical laws. The real world is multiphysics in nature. Real-world systems are typically characterized by multiple, interacting physical processes, interactions that occur on a wide range of both temporal and spatial scales. Multiphysics problems are encountered when the response of a system is affected by the interaction between several distinct physics fields. A multiphysics capable simulation tool is required to correctly capture the coupling effects to provide deeper insight into the performance designs, leading to more economical and safer products, and also to a better understanding of the causes and consequences of natural phenomena. Simulations that couple multiple physical phenomena are as old as simulation themselves, considering computing thermal stress as the simplest example. However, multiphysics simulations deserve a fresh assessment, in light of steadily increasing computational capabilities and greater aspirations for simulations in domains of scientific prediction and engineering design. The issue of coupling models of different phenomena at different scales and governed by different physical laws is largely wide-open and represents an enormously challenging endeavor for future research.

A multiphysics system consists of more than one component governed by its own principles for evolution or equilibrium, typically conservation or constitutive laws. A major classification in such systems is whether the coupling occurs in the bulk (e.g., through source terms or constitutive relations that are active in overlapping domains of the individual components), or whether it occurs over an idealized interface that is lower dimensional or a narrow buffer zone (e.g., through boundary conditions that transmit fluxes, pressures, or displacements).

A promising application of multiphysics simulations is in high temperature/high heat flux components in nuclear energy systems where the environmental and operational conditions are the harshest among any technological applications. Other similar applications where the severe environment of high temperature and high heat flux is met are found in jet engine technology, space propulsion, defense applications, and re-entry vehicles of supersonic aircraft. A typical multiphysics system of high heat flux components includes heat transfer, structural mechanics, and computational fluid dynamics. These systems depend on each other and can be coupled by various interactions. These can be limited to the same domain, or can occur across boundaries with heterogeneous physics. Take the plasma facing component with coolant in a fusion power plant as an example. The fluid flow determines how effective heat transfer is, and heat transfer determines the structural response. The coolant flow needs to be considered as non-isothermal flow, since its temperature variations are significant in this case. When a fluid is subjected to a temperature change, its material properties, such as density and viscosity, change accordingly. The variations in these properties could directly affect its fluid dynamic performance. In addition, since the fluid transports heat, the temperature field is, in turn, affected by changes in the flow field, which means that heat transfer and fluid dynamics are two-way coupled. This two-way coupling between fluid flow and heat transfer is a phenomenon that is prevalent in processes in which components are cooled by a fluid. Thus, we cannot consider each physics separately for the purpose of design or analysis of high heat flux components.

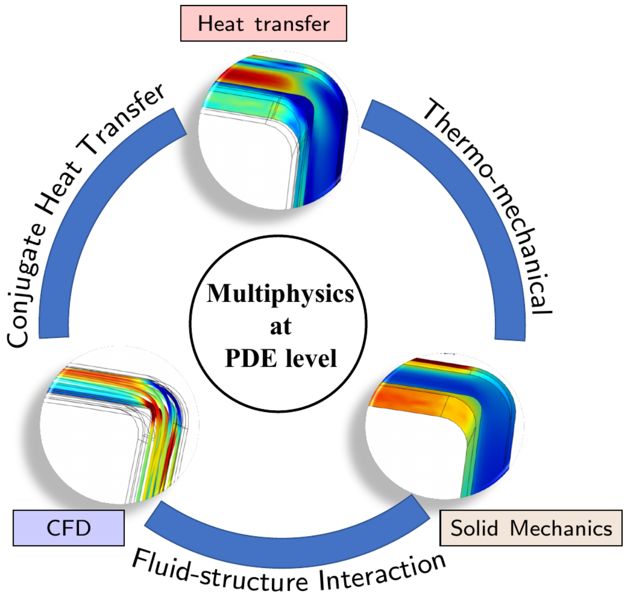

Figure 1.1: Schematic of a typical multiphysics simulation

1.2 Multiscale Modeling Strategies

Multiscale modeling, where the same component is described by more than one formulation at different length scales is another important computational strategy that can be combined with multiphysics to obtain more precise results. For example, Figure 1.2 illustrates a typical hierarchy of mechanics models at different scales. In traditional approaches to modeling, we tend to focus on one particular scale. However, traditional monoscale approaches have proven to be inadequate, because of the range of scales and the prohibitively large number of variables involved. Usually, the microscale model looks into more details and it is more complex than macro-scale models. In other words, macroscale models are not accurate enough compared to the micro-scale models, and the general trend is to embed micro-scale models of material behavior.

The traditional multiscale modeling hierarchy is based on a bottom-up method; meaning that the effects of smaller scales are incorporated through the constitutive relations into larger scales, while the effects of larger scales are neglected. However, the philosophy of multiphysics-multiscale modeling in the research proposed here is based on a top-down method. By discarding the explicit representation of the microstructure, the macroscale approach loses the capability to model the state of the material in terms of direct mapping between the microstructure and properties. Thus, we need the help of microscale models to capture the accurate behavior of the material when empirical macroscale models are inadequate. However, it is inefficient to do the microscale analysis over the entire system. Actually, it is unnecessary to do so, since in many situations, the system of interest can be described adequately by a large-scale model except in some small regions where more detailed information is needed. The small regions may contain some local critical events, such as the behavior of cracks and defects. In such cases, coupling of models at different length scales in different regions may enable us to develop efficient modeling strategies comparable to large-scale models, as well as an accuracy that is comparable to that of the more detailed small-scale models. Generally, we hope to arrive at a reasonable compromise between accuracy and efficiency. Thus, there is a growing need to develop systematic modeling and simulation approaches for multiscale problems.

Multiscale modeling strategies of structural mechanics is a key focus of this dissertation. A set of commonly used models at different scales are shown in Fig. 1.2. Based on the bottom-up multiscale strategy, recent work have attempted to couple molecular dynamics (MD) with dislocation dynamics (DD) [4, 5] and DD with continuum mechanics [6, 7]. As circled in Fig. 1.2, this dissertation focuses on the coupling between the mesoscopic and macroscopic scales within the finite element method (FEM) framework. Macroscopic models include multiphsyics models discussed in Sec. 1.1, where traditional elastic, elasto-plastic mechanics models are used for structural analysis. Mesoscopic models include a dislocation-based crystal plasticity model, which explicitly treats discrete grains and slip systems, accounting for the anisotropy of single crystal properties and crystallographic texture.

The macroscale approach is typically used to solve large boundary value problems since the approach uses a reduced number of Degrees of Freedom (DOFs) to represent the material response at each continuum point. Mesoscale approaches, like crystal plasticity analysis, are more predictive and robust than macroscropic approaches, but are also computationally expensive. The need to investigate crystal plasticity stems from the fact that the behavior

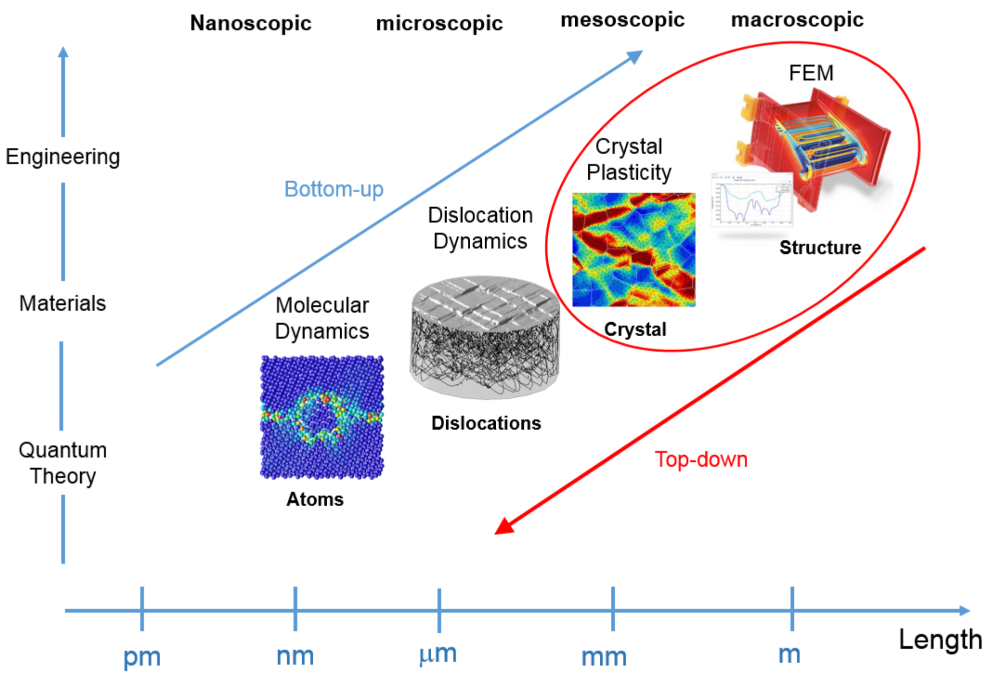

Figure 1.2: Commonly used mechanics models at different length and time scales

at the macrolevel, in particular plastic anisotropy, is controlled by features (dislocations within crystals) at the microscopic level. Moreover, crystal plasticity provides a theory that links the constitutive response to key microstructural features to model plastic anisotropy. The models at two different length scales are linked via a top-down coupling approach, meaning that we start from the macroscale model on the entire domain of interest and pick small regions where local events may occur for detailed mesoscale modeling with boundary conditions provided by the macroscale.

Multiscale and multiphyscis approaches can be combined to solve complex systems with many distinct physical processes. Fig. 1.3 is an example of multiscale-multiphysics design for jet engines. Turbine blades are critical components in jet engines since the operating temperature is high and the blade undergoes cyclic loading that can eventually lead to fatigue failure. Hot air flows around the blade with coolant inside thus resulting in a multiphysics problem. First, there is conjugate heat transfer between air and the blade structure, which requires heat transfer coupling at the fluid-structure interface. The resulting temperature field determines the air material properties. In addition, the flowing air exerts pressure on the blade, which leads to a fluid-structure interaction (FSI) problem. The temperature gradient due to conjugate heat transfer and pressurization due to the coolant flow induce mechanical and thermal stresses in the blade structure. On the multiscale side, thermal fatigue cracking may be observed in some local regions due to thermal cyclic loading. Thus a global-local multiphysics-multiscale strategy is necessary to provide accurate simulation results for design in a relatively efficient way.

Generally, today's problems, unlike traditional science and engineering, do not involve physics processes covered by a single traditional discipline of physics. The issue of coupling models of different events at different scales and governed by different physical laws is largely wide open and represents an enormously challenging area for future research.

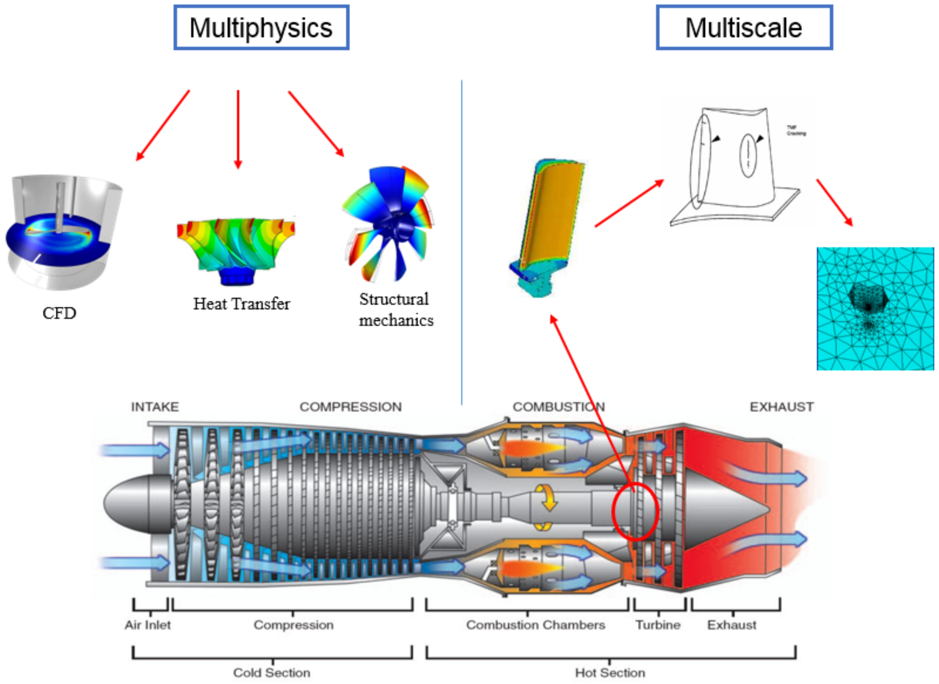

Figure 1.3: Example of Multiscale-Multiphysics design of turbine blades in modern jet engines

The objectives of the present research are:

1. To develop a multiphysics strategy suitable for the design of high heat flux components, and asses the computational issues of coupling between three branches of physics: fluid

mechanics, heat transfer, and solid mechanics.

2. To develop and apply a heterogeneous multiscale modeling strategy that combines the meso- and macro-scales of plastic deformation and fracture of materials. In this method, different sets of equations are sued in different zones of sturtcures to model elasto-plastic deformation and fracture, including a description of the microstructure.

3. To advance the science of crystal plasticity by the development of dislocation-based large deformation framework that is validated by indentation experiments.

4. To apply the developed multiscale-multiphysics framework to real engineering design of critical components in fusion energy systems, namely the first wall, blanket and divertor of the most recent Demonstration power plant (DEMO), designed by the European community (EuroFusion).

In the following chapters, a review of the state of the art in Multi-physics and Multiscale methodologies will be presented in Chapter 2. The major emphasis of the multiphysics is on modeling high heat flux components, while the focus of multiscale modeling is on microstructure-based plasticity and fracture. A novel approach in multiphysics, where the need to couple fluid flow and heat transfer become important will be discussed. On the basis of this analysis, guidance for the selection of of computationally-efficient multiphysics computational strategies will be presented in Chapter 3. The specific focus of a new multisclae computational model is on the description of plasticity in Chapter 4. Here, microstructure information (i.e. dislocations and grains) are accounted for in assessing the distribution of plastic flow and potential fracture sites during high heat flux transients. Advanced design applications of the methodology will then be given in Chapter 5, and finally conclusions will be discussed in Chapter 6. Several publications during the course of this study deal with either multiphysics alone, or multiscale modeling of dislocation-based plasticity are found in references [8, 9, 10, 11, 12].

CHAPTER 2

The Multiphysics Framework and the Multiscale Approach

2.1 A Review of Multiphysics Algorithms

A multiphysics system consists of more than one component governed by its own principles for evolution or equilibrium; typically in the form of conservation or constitutive laws. In addition, most real-life multiphysics problems are inevitably nonlinear, where the solution methods require solving a series of linear subproblems. We review here the solution methods of linear problems, followed by methods for nonlinear problems. The objective is to highlight the key algorithms used in the simulation of multiphysics problems. We will introduce the governing equations of each typical physics, specifically required for the simulation of high heat flux components.

2.1.1 Solution Methods of Linear Problems

Consider the system of linear equations:

$$\boldsymbol{K}\boldsymbol{x} = \boldsymbol{b}, \quad \boldsymbol{K} \in \mathbb{R}^{N\times N}, \quad \boldsymbol{x},\ \boldsymbol{f} \in \mathbb{R}^{N} \tag{2.1}$$

Eq. 2.1 can represent an entire multiphysics problem or some subproblem encountered in a multiphysics solution algorithm. There are two fundamental classes of algorithms that are used to solve for system of linear equations: Direct and iterative methods.

- Direct Solvers

A number of algorithms for the direct solution of the set of linear equations Eq. 2.1 are available today. These include the MUMPS [13], PARDISO [14] and SPOOLES [15] alogorithms. All of them are based on the LU decomposition method of solving a linear algebraic system. All direct solvers will arrive at the same answer for a well-conditioned finite element problem, but differ primarily in the relative speed. PARDISO tends to be the fastest and SPOOLES the slowest. However, SPOOLES tends to use the least memory of all direct solvers. A typical direct solver consists of three distinct steps based on the LU factorization with Partial Pivoting (LUP) [16]:

ALGORITHM 1. Direct solver Method

1. Left multiply $\boldsymbol{K}$ by a permutation matrix $\boldsymbol{P}$ so that LU factorization can be done.
2. Numerical factorization that computes the $\boldsymbol{L}$ and $\boldsymbol{U}$ factors such that $\boldsymbol{LUx} = \boldsymbol{Pb}$
3. Solve the equation $\boldsymbol{Ly} = \boldsymbol{Pb}$ for $\boldsymbol{y}$.
4. Solve the equation $\boldsymbol{Ux} = \boldsymbol{y}$ for $\boldsymbol{x}$.

- Iterative Solvers

Contrary to direct solvers, iterative methods approach the solution gradually, rather than in one large computational step. If direct solvers are computationally expensive, then iterative methods may be considered. There are a variety of iterative methods, the currently most popular ones belong to the class of Krylov subspace methods. Most iterative methods are all essentially similar to a conjugate gradient method [17]. The variations include the Generalized Minimum Residual (GMRES) method and the bi-conjugate gradient stabilized method (BiCGStab).

Take the conjugate gradient method as an example. A typical iterative solver algorithm is explained as follows. Again, consider the system of linear equations shown in Eq. 2.1, where $\boldsymbol{K}$ is a real, symmetric, positive-definite matrix (the case that conjugate gradient method is suitable for).

ALGORITHM 2. Conjugate Gradient Method

```
1. $\boldsymbol{p}_0 = \boldsymbol{r}_0 = \boldsymbol{b} - \boldsymbol{K}\boldsymbol{x}_0$, where $\boldsymbol{x}_0$ is the initial guess of the solution.

2. Do while ($\boldsymbol{r}_{k+1} >$ tolerance)
       $\alpha_k = \frac{\boldsymbol{r}_k^T \boldsymbol{r}_k}{\boldsymbol{p}_k^T \boldsymbol{A} \boldsymbol{p}_k}$
       $\boldsymbol{x}_{k+1} = \boldsymbol{x}_k + \alpha_k \boldsymbol{p}_k$
       $\boldsymbol{r}_{k+1} = \boldsymbol{r}_k - \alpha_k \boldsymbol{A} \boldsymbol{p}_k$
       $\beta_k = \frac{\boldsymbol{r}_{k+1}^T \boldsymbol{r}_{k+1}}{\boldsymbol{r}_k^T \boldsymbol{r}_k}$
       $\boldsymbol{p}_{k+1} = \boldsymbol{r}_{k+1} + \beta_k \boldsymbol{p}_k$
       $k = k + 1$
   end
   The result is $\boldsymbol{x}_{k+1}$.
```

The advantage of iterative solvers over direct ones is that the memory usage is significantly less. But the disadvantage is that they are not very robust and different physics do require different iterative solver settings.

2.1.2 Solutions to nonlinear problems

Most real-life problems are nonlinear. Solvers for linear problems can be extended for nonlinear systems by using Newton's method. Each step of Newton's method can be solved by either direct or iterative solvers discussed in Section 2.1.1. Iterative methods for nonlinear equations can be described in terms of the transition from a current iterate x_i to a new iterate x_{i+1}. In another words, Newton's method is based on the following iteration scheme [18]:

$$\boldsymbol{J}(\boldsymbol{x}_i) \cdot (\boldsymbol{x}_{i+1} - \boldsymbol{x}_i) = F(\boldsymbol{x}_i) \tag{2.2}$$

where $F(\boldsymbol{x}) = \boldsymbol{K}\boldsymbol{x} - \boldsymbol{b}$ represents the system of nonlinear equations. $\boldsymbol{J}$ is the Jacobian which computes the derivative of F: $\boldsymbol{J}(\boldsymbol{x}_i) = F'(\boldsymbol{x}_i) = \partial F / \partial \boldsymbol{x}|_{\boldsymbol{x}=\boldsymbol{x}_i}$.

Similar to the direct method, LU factorization is used for $\boldsymbol{J}(\boldsymbol{x}_i)$ to solve for $\boldsymbol{x}_{i+1}$. The inputs of the algorithm are the initial iterate $\boldsymbol{x}_0$, the nonlinear map F, and a vector of termination tolerances $\boldsymbol{\tau} \in \mathbb{R}^2$.

ALGORITHM 3. Newton's Method

```
1. $r_0 = ||F(\boldsymbol{x}_0)||$
2. Do while $(||F(\boldsymbol{x}_i)|| > \boldsymbol{\tau})$
       Compute $\boldsymbol{J}(\boldsymbol{x}_i)$
       Factor $\boldsymbol{J}(\boldsymbol{x}_i) = \boldsymbol{LU}$
       Solve $\boldsymbol{LUs} = -F(\boldsymbol{x}_i)$
       $\boldsymbol{x}_{i+1} = \boldsymbol{x}_i + \boldsymbol{s}$
       Evaluate $F(\boldsymbol{x}_{i+1})$
       $i = i + 1$
   end
```

The algorithm works properly only when the initial iterate is sufficiently near the solution. The solution procedure can fail to converge if the initial condition is too far away from solution.

2.1.3 Solutions of multiphysics problems

Algorithms that used for solving systems of linear and nonlinear equations can be extended to solving multiphysics problems, where multiple different interdependent physics is solved within the same domain.

Take the simplest multiphysics problem — two-physics system as an example:

$$\begin{cases} F_1(\boldsymbol{x}_1, \boldsymbol{x}_2) = \boldsymbol{K}_1\boldsymbol{x}_1 - \boldsymbol{b}_1 = 0 \\ F_2(\boldsymbol{x}_1, \boldsymbol{x}_2) = \boldsymbol{K}_2\boldsymbol{x}_2 - \boldsymbol{b}_2 = 0 \end{cases} \tag{2.3}$$

Unlike the uniphysics systems where the system matrix depends on variables of its own physics, the system matrix of each individual physics in a multiphysics problem can be dependent on the variables of other physics, introducing the coupling effects.

- Segregated approach

Segregated approach preserves the integrity of the two uniphysics problems, solving the first equation for the first unknown given the second unknown, and the second equation for the second unknown given the first. The multiphysics coupling is taken into account by iteration over the pair of problems. This iteration method is considered as loosely coupled. When the iteration converges, the accuracy of the solution can be improved by continuing the iterations. One typical algorithm belongs to segregated approach is Gauss-Seidel method [19].

ALGORITHM 4. Gauss-Seidel Multiphysics Coupling

```
1. Given initial iterate $\{\boldsymbol{x}_1^0, \boldsymbol{x}_2^0\}$, $\boldsymbol{r}^0 = (||F_1(\boldsymbol{x}_1^0, \boldsymbol{x}_2^0)||,\ ||F_2(\boldsymbol{x}_1^0, \boldsymbol{x}_2^0)||)$

2. Do while $(\boldsymbol{r}^k > (\tau_1, \tau_2))$
       Solve for $\boldsymbol{v}$ in $F_1(\boldsymbol{v}, \boldsymbol{x}_2^k) = 0$; set $\boldsymbol{x}_1^{k+1} = \boldsymbol{v}$
       Solve for $\boldsymbol{w}$ in $F_2(\boldsymbol{x}_1^{k+1}, \boldsymbol{w}) = 0$; set $\boldsymbol{x}_2^{k+1} = \boldsymbol{w}$
       $k = k + 1$
   end
```

Generally, the segregated approach treats each physics sequentially, using the results of the previously solved physics to evaluate the variables for the next physics being solved. The great advantage to the segregated approach is that the optimal solver can be used in each substep and a smaller problem is solved at each step.

- Fully-coupled approach

Alternatively, a fully-coupled method can be used to solve the multiphysics problem, assuming that all of the couplings between the physics are considered at the same time. There is no conceptual difference between solving a single physics nonlinear problem and solving a coupled-physics problem using fully-coupled approach. It usually requires more memory-intense direct solvers.

Here, the problem is formulated in terms of a single residual that includes all components in the multiphysics problems.

$$F(\boldsymbol{x}) = \begin{Bmatrix} F_1(\boldsymbol{x}_1, \boldsymbol{x}_2) \\ F_2(\boldsymbol{x}_1, \boldsymbol{x}_2) \end{Bmatrix} = \begin{bmatrix} \boldsymbol{K}_1 & 0 \\ 0 & \boldsymbol{K}_2 \end{bmatrix} \begin{bmatrix} \boldsymbol{x}_1 \\ \boldsymbol{x}_2 \end{bmatrix} - \begin{bmatrix} \boldsymbol{b}_1 \\ \boldsymbol{b}_2 \end{bmatrix} = 0 \tag{2.4}$$

where $\boldsymbol{x} = (\boldsymbol{x}_1, \boldsymbol{x}_2)$. Since solving multiphysics problems by fully-coupled approach is conceptually similar to solving a nonlinear uniphysics problem, Newton's method demonstrated in *Algorithm* 3 can be applied here. However, due to the interactions between different physics, non-zero off-diagonal blocks will be included in the Jacobian $\boldsymbol{J}$.

$$\boldsymbol{J} = \begin{bmatrix} \frac{\partial F_1}{\partial x_1} & \frac{\partial F_1}{\partial x_2} \\ \frac{\partial F_2}{\partial x_1} & \frac{\partial F_2}{\partial x_2} \end{bmatrix} \tag{2.5}$$

The segregated approach will usually take more iterations to converge; however, the memory and time requirements for each sub-step will be lower, so the total solution time and memory usage can be lower with the segregated approach. On the other hand, fully-coupled approach is more memory-intensive, but is necessary for multiphysics problems that have very strong interactions between the various physics being solved.

2.2 Multiphysics Elements for Extreme Heat Flux

As discussed in Chapter 1, a typical multiphysics system of high heat flux components include heat transfer, structural mechanics and computational fluid dynamics, as Fig. 1.1 shows. The governing equations and boundary conditions of each physics are reviewed as follows. The interactions between different physics will be introduced in Chapter 3.

2.2.1 Heat Transfer

Heat transfer is thermal energy in transit due to a spatial temperature difference. Three typical heat transfer modes are: conduction, convection and radiation. Heat transfer is a critical physics in engineering problems, such as plasma-facing component in fusion power plant. Conduction refers to the heat transfer that occur across the medium, while convection refers to the heat transfer that occur between a surface and a moving fluid when they are at different temperatures. Therefore, conduction problems are usually solved by domain PDEs while convection problems are modeled as boundary conditions.

Based on the first law of thermodynamics, the governing equation of conduction assuming no mass transfer or radiation can be expressed as a parabolic partial differential equation as follows [20].

$$\rho C_p \frac{\partial T}{\partial t} - \nabla \cdot (k \nabla T) = \dot{Q} \tag{2.6}$$

where ρ is the density of medium, C_p is the heat capacity, k is the thermal conductivity and $\dot{Q}$ is the volumetric heat source.

The PDE can be written in the weak variational form suitable for FEM implementation by multiplying with a test function δT, integrating over the domain, using integration by parts, and applying Gauss's theorem to change volume to surface integrals. The procedure gives:

$$\int_\Omega \left(\rho C_p \frac{\partial T}{\partial t} + \nabla \cdot (-k \nabla T) - \dot{Q} \right) \delta T d\Omega = 0 \tag{2.7}$$

$$\int_\Omega \left(\rho C_p \frac{\partial T}{\partial t} - \dot{Q} \right) \delta T \delta\Omega + k \nabla T \cdot \delta \nabla T d\Omega - \int_S k \nabla T \cdot \boldsymbol{n} \delta T dS = 0 \tag{2.8}$$

The first part of Eq. 2.8 is the weak formulation over the domain if δT is replaced by the test function (denoted as test(T) or $\tilde{T}$), while the second part is the surface integral over the boundaries, served as boundary conditions.

The dependent variable T is prescribed when Dirichlet boundary conditions are prescribed. These conditions appear as constraints in formulas.

$$T = T_0 \quad \rightarrow (T_0 - T) \cdot \text{test}(-T) \quad \text{on} \quad \partial\Omega_T \tag{2.9}$$

Alternatively, the heat flux q is prescribed when Neumann boundary conditions are applied.

$$q = -k \nabla T \cdot \boldsymbol{n} = q_0 \quad \rightarrow q_0 \cdot \text{test}(T) \quad \text{on} \quad \partial\Omega_q \tag{2.10}$$

If convection occurs on the Neumann boundary, then q_0 can be expressed as $h \cdot (T_{\text{ext}} - T)$, where h is the heat transfer coefficient.

2.2.2 Fluid Flow

The fundamental equations of fluid dynamics are based on the conservation laws, such as conservation of mass, conservation of momentum and conservation of energy (used for heat transfer in fluids).

Mass conservation is often regarded as continuity equation. The differential form is:

$$\frac{\partial \rho}{\partial t} + \nabla \cdot (\rho \boldsymbol{u}) = 0 \tag{2.11}$$

By the divergence theorem, it can be converted into integral form:

$$\frac{\partial}{\partial t} \int_{\Omega} \rho d\Omega = - \oint_{S} \rho \boldsymbol{u} \cdot d\boldsymbol{S} \tag{2.12}$$

The integral form can be interpreted as the rate of change of fluid mass inside a control volume must be equal to the net rate of fluid flow into the volume.

The conservation of momentum equations for compressible, viscous flow case are called Navier-Stokes equation, which applies Newton's second law to fluid motion, with the assumption that the stress in fluid is the sum of a viscous term and a pressure term.

$$\rho \frac{D\boldsymbol{u}}{Dt} = \rho \frac{\partial \boldsymbol{u}}{\partial t} + \rho \boldsymbol{u} \cdot \nabla \boldsymbol{u} = \nabla \cdot \left[-p\mathbf{I} + \underbrace{\mu(\nabla \boldsymbol{u} + \nabla \boldsymbol{u}^T) - \frac{2}{3}\mu(\nabla \cdot \boldsymbol{u})\mathbf{I}}_{\text{viscous stress } \boldsymbol{\tau}} \right] + \boldsymbol{F} \tag{2.13}$$

Transfer Eq. 2.11 and Eq. 2.13 into the weak form expression:

$$\int_{\Omega} \left((\frac{\partial \rho}{\partial t} + \nabla \cdot (\rho \boldsymbol{u}) \right) \delta p \; d\Omega = 0 \tag{2.14}$$

$$\int_{\Omega} \left(\rho \frac{\partial \boldsymbol{u}}{\partial t} + \rho \boldsymbol{u} \cdot \nabla \boldsymbol{u} - \nabla \cdot [-p\mathbf{I} + \boldsymbol{\tau}] - \boldsymbol{F} \right) \cdot \delta \boldsymbol{u} \; d\Omega = 0 \tag{2.15}$$

$$\int_{\Omega} \left((\rho \frac{\partial \boldsymbol{u}}{\partial t} + \rho \mathbf{u} \cdot \nabla \boldsymbol{u} - \boldsymbol{F}) \cdot \delta \boldsymbol{u} + [-p\mathbf{I} + \boldsymbol{\tau}] : \delta \nabla \boldsymbol{u} \right) d\Omega - \int_{S} [-p\mathbf{I} + \boldsymbol{\tau}] \cdot \boldsymbol{u} \cdot \boldsymbol{n} \; \delta \boldsymbol{u} \; dS = 0 \tag{2.16}$$

Eq. 2.14 and the first part of Eq. 2.16 are the weak formulations over the domain, while the second part of Eq. 2.16 is the surface integral over the boundaries, served as boundary conditions.

The inlet and outlet need to be specified with either Dirichlet or Neumann boundary conditions. When Dirichlet boundary conditions are applied, velocity vector $\boldsymbol{u}$ is specified on the boundary.

$$\boldsymbol{u} = \boldsymbol{u}_0 \quad \rightarrow (\boldsymbol{u}_0 - \boldsymbol{u}) \cdot \text{test}(-\boldsymbol{u}) \ \text{ on } \ \partial\Omega_u \tag{2.17}$$

Neumann boundary conditions are applied when pressure p is specified on the boundary.

$$[-p\mathbf{I} + \boldsymbol{\tau}] \cdot \boldsymbol{n} = -p_0\boldsymbol{n} \quad \rightarrow -p_0\boldsymbol{n} \cdot \boldsymbol{u} \cdot \text{test}(\boldsymbol{u}) \ \text{ on } \ \partial\Omega_p \tag{2.18}$$

2.2.3 Solid mechanics

Large-deformation elasto-plasticity model is introduced here since this provides the fundamental computational framework of crystal plasticity, which will be reviewed in the next section.

We represent the positions of material points relative to an arbitrary origin in the reference configuration by the vector $\boldsymbol{X}$. As a result of deformation, this vector is mapped into the current configuration $\boldsymbol{x} = \boldsymbol{X} + \boldsymbol{u}$, where $\boldsymbol{u}$ is the displacement vector. These vectors are related by the total deformation gradient tensor $\boldsymbol{F}$, which is a two-point tensor which involves both the reference and present configurations:

$$\boldsymbol{F} = \frac{\partial \boldsymbol{x}}{\partial \boldsymbol{X}} = \nabla \boldsymbol{u} + \boldsymbol{I} \tag{2.19}$$

The deformation of the material causes changes in the material density. The ratio between current and initial volume is given by:

$$\frac{\mathrm{d}V}{\mathrm{d}V_0} = \frac{\rho_0}{\rho} = \det(\boldsymbol{F}) = J \tag{2.20}$$

Thus the determinant of the deformation gradient tensor $\boldsymbol{F}$ is always positive, which implies that $\boldsymbol{F}$ is invertible. $J = 1$ implies an isochoric process, meaning no volume change.

Applying a right polar decomposition of deformation gradient tensor $\boldsymbol{F}$ gives an insight into how much stretch and rotation a unit volume of material has suffered. That is $\boldsymbol{F} = \boldsymbol{R}\boldsymbol{U}$, where $\boldsymbol{R}$ is a proper orthogonal tensor (det($\boldsymbol{R}$=1, and $\boldsymbol{R}^{-\mathbf{1}} = \boldsymbol{R}^{\boldsymbol{T}}$)), and $\boldsymbol{U}$ is the right stretch tensor given in the material frame. The right Cauchy-Green deformation tensor $\boldsymbol{C}$ is defined by:

$$\boldsymbol{C} = \boldsymbol{F}^{\boldsymbol{T}}\boldsymbol{F} = \boldsymbol{U}^{\boldsymbol{2}} \tag{2.21}$$

is a symmetric and positive definite tensor, which accounts for the strain but not for the rotation. Also, the Green-Lagrange strain tensor is a symmetric tensor:

$$\boldsymbol{E} = \frac{1}{2}(\boldsymbol{C} - \boldsymbol{I}) \tag{2.22}$$

When plasticity is considered, the total deformation gradient tensor can be multiplicatively decomposed into elastic and plastic component:

$$\boldsymbol{F} = \boldsymbol{F}^{E} \cdot \boldsymbol{F}^{P} \tag{2.23}$$

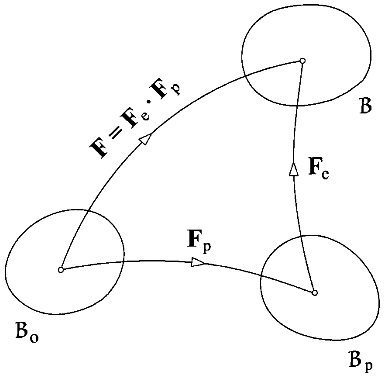

Figure 2.1: Elastoplastic deformation gradient decomposition

The elastic and plastic Green-Lagrange strain tensor are computed from the elastic and plastic deformation gradient tensor respectively:

$$\boldsymbol{E}^{E} = \frac{1}{2}(\boldsymbol{F}^{E^T}\boldsymbol{F}^{E} - \boldsymbol{I}), \quad \boldsymbol{E}^{P} = \frac{1}{2}(\boldsymbol{F}^{P^T}\boldsymbol{F}^{P} - \boldsymbol{I}) \tag{2.24}$$

The total, plastic and elastic Green-Lagrange strain tensors are related as[1]:

$$\boldsymbol{E}^{E} = \boldsymbol{F}^{P^{-T}}(\boldsymbol{E} - \boldsymbol{E}^{P})\boldsymbol{F}^{P^{-1}} \tag{2.25}$$

---

[1] $E^E = \frac{1}{2}(F^{E^T}F^E - I) = \frac{1}{2}(F^{P^{-T}}F^TFF^{P^{-1}} - I) = \frac{1}{2}(2F^{P^{-T}}EF^{P^{-1}} + F^{P^{-T}}F^{P^{-1}} - I) => F^{P^T}E^EF^P = E + \frac{1}{2}I - \frac{1}{2}F^{P^T}F^P = E - E^P => E^E = F^{P^{-T}}(E - E^P)F^{P^{-1}}$

The elastic deformation gradient $\boldsymbol{F}^E$ is the component due to the reversible response to external loads and displacements, while the plastic deformation gradient $\boldsymbol{F}^P$ is an irreversible permanent deformation that persists when all external loads and displacements are removed. As a result, transformation of the reference frame by $\boldsymbol{F}^P$ leads to an intermediate frame which is obtained from the current configuration by destressing to zero stress (free from external stresses). In this intermediate configuration, a strain energy density per unit intermediate volume $\tilde{W}_s$ exists, and it's a function of elastic deformation only:$\tilde{W}_s = \tilde{W}_s(\boldsymbol{E}^E)$.

Several commonly used strain energy density equations for different material models are listed in Table 2.1.[2]

Neo-Hookean [21]	St.Venant-kirchhoff [22]	Ciarlet [23]
$\frac{1}{2}\mu(I_1 - 3) - \mu\ln(J) + \frac{1}{2}\lambda[\ln(\mathrm{J})]^2$	$\frac{1}{2}(\lambda + 2\mu)I_1^2 - 2\mu I_2$	$\frac{\lambda}{4}(I_3 - 1) - \frac{\lambda+2\mu}{4}\ln I_3$

Table 2.1: Commonly used strain energy models

The total potential energy equals to the internal strain energy minus the work of external forces:

$$\Pi = \int_{\Omega_0} \tilde{W}_s(\boldsymbol{E}^E)J^p \mathrm{d}\Omega_0 - \oint_{\partial\Omega_0} t_i u_i dA_0 \tag{2.26}$$

The displacement $\boldsymbol{u}$ should minimize the potential energy Π, which implies:

$$\delta\Pi = \int_{\Omega_0} \frac{\partial \tilde{W}_s}{\partial E^E_{\alpha\beta}} \frac{\partial E^E_{\alpha\beta}}{\partial F^E_{j\gamma}} \frac{\partial F^E_{j\gamma}}{\partial F_{iJ}} \delta F_{iJ} J^p \mathrm{d}\Omega_0 - \oint_{\partial\Omega_0} ti\delta u_i \mathrm{d}A_0 = 0 \tag{2.27}$$

Introduce the second Piola stress: $S_{KL} = \frac{\partial \tilde{W}_s(\boldsymbol{E}^E)}{\partial E_{KL}}$ and first Piola stress: $P_{iJ} = F_{iK}S_{KJ}$. Simplify Eq. 2.27 to be[3]:

$$\delta\Pi = \int_{\Omega_0} P_{iJ}\delta u_{i,J} \mathrm{d}\Omega_0 - \oint_{\partial\Omega_0} t_i \delta u_i \mathrm{d}A_0 = 0 \tag{2.28}$$

The dependent variable displacement $\boldsymbol{u}$ is prescribed when Dirichlet boundary conditions are applied.

$$\boldsymbol{u} = \boldsymbol{u}_0 \quad \rightarrow (\boldsymbol{u}_0 - \boldsymbol{u}) \cdot \mathrm{test}(-\boldsymbol{u}) \;\; \text{on} \;\; \partial\Omega_u \tag{2.29}$$

---

[2] $I_1(\boldsymbol{C}) = \mathrm{tr}(\boldsymbol{C}) \quad I_2(\boldsymbol{C}) = \frac{1}{2}(I_1^2(\boldsymbol{C}) - \mathrm{tr}(\boldsymbol{C}^2)) \quad I_3(\boldsymbol{C}) = \det(\boldsymbol{C})$

[3] $\frac{\partial E_{KL}}{\partial F_{iJ}} = \frac{\partial \frac{1}{2}(F_{iK}F_{iL} - I_{KL})}{\partial F_{iJ}} = \frac{1}{2}\delta_{KJ}F_{iL} + \frac{1}{2}F_{iK}\delta_{LJ}, \quad \delta F_{iJ} = \delta u_{i,J}$

Alternatively, the traction $\boldsymbol{t}$ is prescribed when Neumann boundary conditions are applied.

$$\boldsymbol{t} = \boldsymbol{P} \cdot \boldsymbol{n} = \boldsymbol{t}_0 \quad \rightarrow \boldsymbol{t}_0 \cdot \text{test}(\boldsymbol{u}) \;\; \text{on} \;\; \partial\Omega_t \tag{2.30}$$

The different types of boundary conditions used in each physics are summarized in Table 2.2.

	Heat transfer	Fluid dynamics	Solid mechanics
Dirichlet B.C.	Temperature [K]	Velocity [m/s]	Displacement [m]
Neumann B.C.	Heat flux [W/m^2]	Pressure [Pa]	Traction [N/m^2]

Table 2.2: Summary of boundary conditions for each commonly used physics

2.3 Review of Multiscale Methods of Elasto-plastic Deformation

Recent developments in the simulation of complex systems lead to larger and larger numbers of equations. Although computational capabilities have improved significantly recent years, new numerical methods are required to achieve greater efficiency. Global-local methods combined with finite element analysis were developed for solving differential equations using a hierarchy of discretization. It is well known that displacement-formulated finite elements converge in displacement much faster than in stress, meaning that coarser meshes can achieve a good convergence in displacement though not in stress. Based on the fast convergent nature of FEM in displacement, a global-local method was developed where the global displacement solution is utilized as boundary conditions for a local region of interest. In the local region, a refined mesh is used for further analysis to improve the accuracy of the solution in stresses. Generally speaking, the procedure of the global-local method involves two steps. The first step is called global analysis which gives a reasonably good solution in displacements. The second step is local analysis which is performed locally, utilizing the global analysis results to obtain more accurate stresses in the region of interest.

The global-local methods discussed above can be classified as either homogeneous or heterogeneous, based on the equations applied in global and local regions. In homogeneous systems, the same conservation and constitutive equations are applied in the global and local regions but local regions have a finer mesh, and thus could provide higher resolution. These kinds of methods are usually known as grid refinement methods [24, 25, 26]. On the other hand, in heterogeneous systems, the global and local domains are described by the same conservation equations but with different constitutive laws thus creating an incompatibility of either displacement or traction at their interface. Previous work on heterogeneous global-local methods includes references [27, 28]. This section will have a review of different global-local methods, starting first with homogeneous systems.

2.3.1 Multi-grid Method for Homogeneous Systems

Before coupling two different constitutive models at different scales, multi-grid methods which solve the same model on different meshes are reviewed here, since they provide the basic idea of global-local finite element analysis procedure.

Several previous studies [24, 25, 26] proposed global-local multi-grid methods which can achieve greater speed than the conventional finite element analysis. Generally, the procedure consists of two steps of computation. Take the rectangle panel with a center crack as an example, where the region of interest is near the crack as shown in Fig. 2.2 labeled as ABCD. The first step is a global analysis of the displacement field in the whole structure using a coarse mesh. The second step is the stress analysis of local regions with refined meshes using the global displacements $\boldsymbol{u}_{\text{global}}$ as boundary conditions on the global-local interface boundaries $\partial\Omega_{\text{int}}$ for the local regions. Due to the mesh refinement in the local region, additional nodes are introduced on the interface boundary which leads to the mismatch of the nodes. Thus the displacement boundary conditions for the local region need to be derived from the global solution. One convenient method is to interpolate the displacements at the refined nodes employing the shape function used in the global analysis. Note that if the traction is prescribed on part of the boundaries of the local region, then the traction boundary condition should be incorporated in the local analysis.

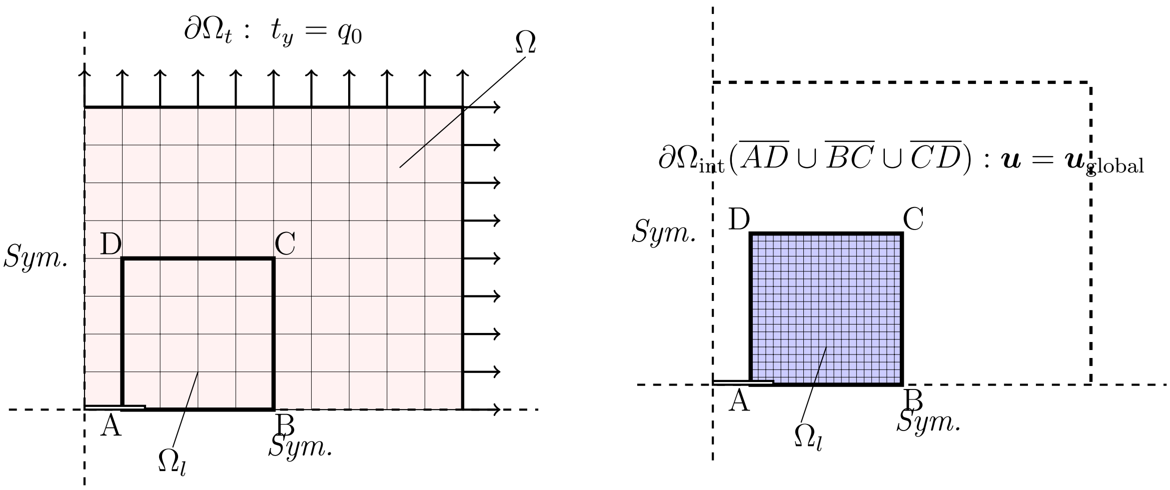

(a) Global analysis with coarse mesh

(b) Local analysis with finer mesh

Figure 2.2: Global-local multi-grid method

Here we present two test cases based on the work of Sun *et al.* [24, 25], both of which are applied to the solution of a center-cracked panel problem, described in Fig. 2.2. The panel is under uniform loading at its edges, with a traction $t_y = q_0$. Test case 1 is for linear elastic constitutive laws in the both the local and global domains, while test case 2 is extended to for an elasto-plastic model.

- Test case 1: Elastic analysis of a cracked panel

The cracked panel problem described in Fig. 2.2 was solved by three different methods to analyze the stress distribution near the crack tip, which are elastic analysis with global coarse meshes (120 quadrilateral elements), elastic analysis with global fine meshes (3000 quadrilateral elements) and global-local method (100 quadrilateral elements in the local region).

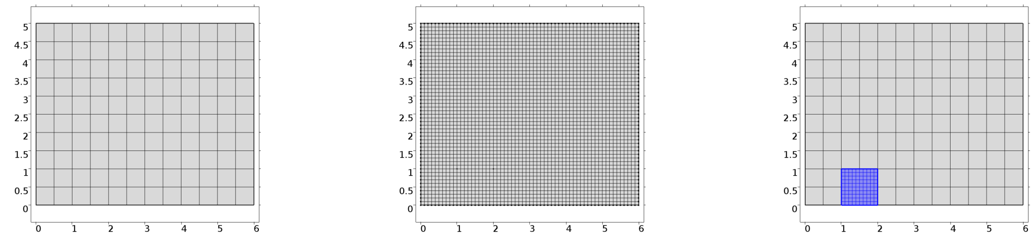

(a) (b) (c)

Figure 2.3: (a) Coarse mesh (b) Fine mesh (c) Global-local method mesh

Half panel side length [in]	Load [lbf/in]	Crack length [in]	Young's Modules [psi]	Poisson ratio
10	6	1	2.4×10^6	0.2

Table 2.3: Details about the test case 1 model

The stresses near the crack tip along the x-direction are plotted for comparison as presented in Fig 2.4 and 2.5. The comparison in Fig 2.4 and 2.5 indicates that while global coarse mesh is not able to give accurate results, the global-local solution agrees well with the fine mesh solution up to the crack tip.

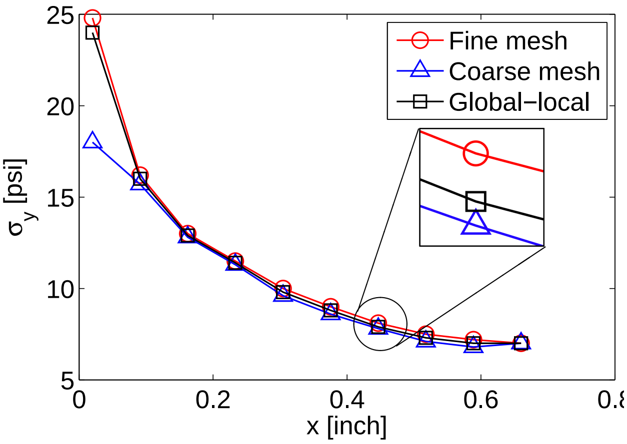

Figure 2.4: σ_{yy} near crack tip

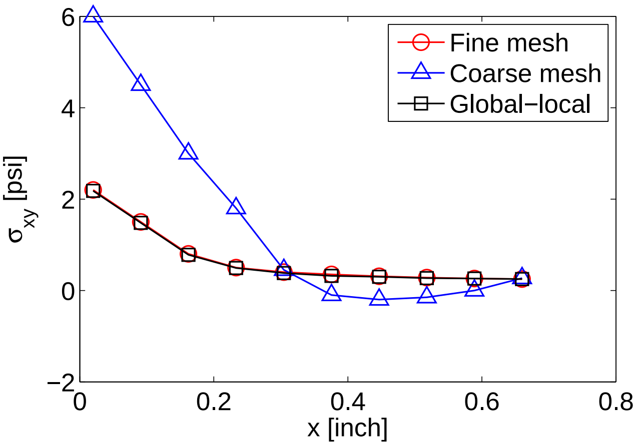

Figure 2.5: σ_{xy} near crack tip

This homogeneous multi-grid method can be used to achieve great time savings for computations without losing too much accuracy. However, the limitation of this homogeneous multi-grid method is that it is only suitable for cases where the global and local regions share the same constitutive equations but different meshes. In addition, due to significant improvements in the computational capabilities in recent years, this method is gradually losing its advantages.

- Test case 2: Elasto-plastic analysis of a cracked panel

The homogeneous multi-grid method discussed above can be extended to solve non-linear elasto-plastic problems [25]. The basic idea is the same as the method described for elastic problems, which is based on a two-step procedure that involves two sets of meshes of different sizes. But due to the nonlinear nature of the elasto-plastic problem, the global-local analyses need to be performed several times. The procedure is as follows.

ALGORITHM 5. Elasto-plastic Multigrid Method

Step 1. Perform the global analysis on the global mesh.

Step 2. The local analysis is performed on the local mesh by using displacements from the global analysis as boundary conditions iteratively.

Step 3. At the end of the iteration process of the local analysis, the updated stress at Gaussian points of local mesh are used to interpolate the stresses at the Gaussian points of the global mesh.

Step 4. The stresses obtained from *Step 3.* are in turn used to update the stiffness matrix for the global analysis in the next load increment.

As indicated in *Step 4.* above, the global stiffness matrix needs to be updated during each incremental load step. Assuming the Von Mises yield criteria with a hardening function $H(\bar{\epsilon}^p)$, where $d\bar{\epsilon}^p$ is the effective incremental plastic strain. The incremental stress can be computed from incremental elastic strain.

$$d\sigma_{ij} = D_{ijkl} d\epsilon^e_{kl} = D_{ijkl}(d\epsilon_{kl} - d\epsilon^p_{kl}) \tag{2.31}$$

where the plastic part of the incremental strain is obtained from the associated flow rule:

$$d\epsilon^p_{ij} = d\lambda \frac{\partial \bar{\sigma}}{\partial \sigma_{ij}} = d\bar{\epsilon}^p \frac{\partial \bar{\sigma}}{\partial \sigma_{ij}} \tag{2.32}$$

Introduce $H' = dH(\bar{\epsilon}^p)/d\bar{\epsilon}^p = d\bar{\sigma}/d\bar{\epsilon}^p$, then

$$d\epsilon^p_{kl} = \frac{1}{H'}\frac{\partial\bar{\sigma}}{\partial\sigma_{ij}}d\sigma_{ij}\frac{\partial\bar{\sigma}}{\partial\sigma_{kl}} = \frac{1}{H'}\frac{\partial\bar{\sigma}}{\partial\sigma_{ij}}D_{ijmn}(d\epsilon_{mn} - d\epsilon^p_{mn})\frac{\partial\bar{\sigma}}{\partial\sigma_{kl}} \tag{2.33}$$

$$(\delta_{km}\delta_{ln} + \frac{1}{H'}\frac{\partial\bar{\sigma}}{\partial\sigma_{ij}}D_{ijmn}\frac{\partial\bar{\sigma}}{\partial\sigma_{kl}})d\epsilon^p_{mn} = \frac{1}{H'}\frac{\partial\bar{\sigma}}{\partial\sigma_{ij}}D_{ijmn}\frac{\partial\bar{\sigma}}{\partial\sigma_{kl}}d\epsilon_{mn} \tag{2.34}$$

$$d\sigma_{ij} = \left(D_{ijmn} - \frac{D_{ijmn}\frac{\partial\bar{\sigma}}{\partial\sigma_{qr}}D_{qrst}\frac{\partial\bar{\sigma}}{\partial\sigma_{kl}}}{H'\delta_{ks}\delta_{lt} + \frac{\partial\bar{\sigma}}{\partial\sigma_{qr}}D_{qrst}\frac{\partial\bar{\sigma}}{\partial\sigma_{kl}}}\right)d\epsilon_{mn} \tag{2.35}$$

The expression inside the bracket in Eq. 2.35 indicates how the stiffness matrix for the global analysis is updated during each load increment.

Similar as the test case of homogeneous multi-grid method for elastic problem, a center-cracked panel subjected to a uniform tensile stress was considered as test case here. To demonstrate the efficiency of the global-local approach, three schemes are adopted for the analysis of the crack problem. The first scheme is the elasto-plastic analysis with coarse mesh. The second scheme is the global-local method using coarse meshes in the global analysis and local region near the crack tip in the local analysis. The third scheme is the elasto-plastic analysis using fine meshes over the whole domain. These three different mesh configurations are same as the ones used in the Test case 1, as shown in Fig. 2.3. The model set-up, including geometric parameters, loading condition and material properties is summarized in Table 2.4.

Half panel length [in]	Half panel width [in]	Load [ksi]	Crack length [in]
6	5	18	1
Young's Modulus [psi]	Poisson ratio	Tangent modulus [psi]	Yield strength [psi]
10×10^6	0.3	2.5×10^6	45×10^3

Table 2.4: Details about the test case 2 model

The displacement in the y direction obtained from both global fine and coarse mesh along the top boundary of local region is shown in Fig. 2.6. A max error around 5% is observed. The Von mises stresses near the crack tip along the x direction obtained from three different schemes are plotted in Fig. 2.7. It can be clearly seen that global-local analysis result agrees well with the global fine mesh result while the results obtained from global coarse mesh significantly underestimate the stresses near the tip. It can be concluded that the error in the global displacements doesn't significantly affect the accuracy of the local stress results.

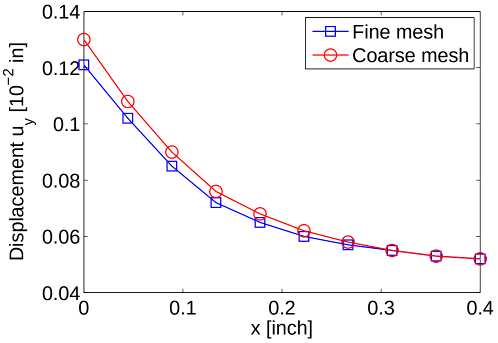

Figure 2.6: Vertical displacements along y=0.2 in.

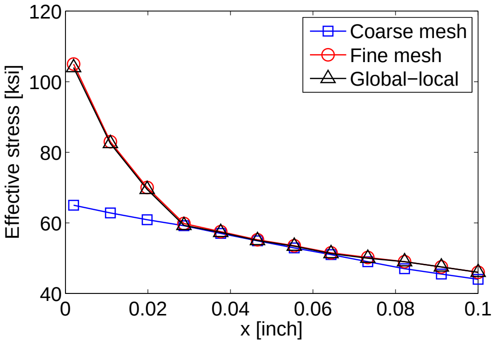

Figure 2.7: Effective stress along y=0.028 in near crack tip

The global-local multigrid method for homogeneous systems discussed in this section saves computation time and provides reliable results that agree well with the results of a fine global mesh. However, this method is gradually losing its advantages due to the significant improvements in the computational capabilities in recent years. The global-local methods for heterogeneous systems, where the constitutive equations in one domain are different from another, are more challenging, and thus will be discussed next.

2.3.2 The Local Defect Correction Method for Heterogeneous Systems

If the constitutive equations in the global and local domains are different, the simplest example of which is of an elasto-plastic model in the local domain but a purely elastic model in the global domain. Here, there will be a mismatch of stresses and tractions occurring on the global-local interface boundaries, even if the displacements are continuous. To solve this problem, an algorithm based on multi-grid iteration was proposed by W. Hackbusch [27] to reduce the mismatch.

Fig. 2.2 can also be used to explain this local defect correction method since it is based on the multi-grid framework. The procedure is as follows.

ALGORITHM 6. Local Defect Correction Method (LDC)

Step 1. Solve the boundary value problem in the global domain Ω_g.

$$L(\boldsymbol{u}) = f^i; \quad f^0 = f; \tag{2.36}$$

Let $\boldsymbol{u}^i$ be the solution of the boundary value problem. i is the iteration index which is zero initially.

Step 2. Interpolate the boundary values on $\partial\Omega_{\text{int}}$ based on the result of $\boldsymbol{u}^i$.

$$\boldsymbol{u}_l^i = \boldsymbol{I}\boldsymbol{u}^i; \tag{2.37}$$

where $\boldsymbol{I}$ describes some interpolation of $\boldsymbol{u}^i$ in the Ω_g (for instance, using shape functions as introduced in Sec. 2.3.1) at the boundary points of $\partial\Omega_{\text{int}}$.

Step 3. Solve the boundary value problem in local domain Ω_l, with the boundary conditions determined based on the global domain solution.

$$L_l(\boldsymbol{u}_l) = f_l, \quad \boldsymbol{u}_l = \boldsymbol{u}_l^i \text{ on } \partial\Omega_{\text{int}}; \tag{2.38}$$

Step 4. Interpolate $\boldsymbol{u}_l$ on the global nodes of Ω.

$$\tilde{\boldsymbol{u}} = \boldsymbol{J}\boldsymbol{u}_l; \tag{2.39}$$

where $\boldsymbol{J}$ describes some interpolation of $\boldsymbol{u}_l$ on global nodes in Ω_g.

Step 5. Compute the defect in Ω_l:

$$d = L(\tilde{\boldsymbol{u}}) - f^i; \tag{2.40}$$

Step 6. Define the next right-hand side by:

$$f^{i+1} = f + d \text{ in } \Omega_l; \quad f^{i+1} = f \text{ in } \Omega \backslash \Omega_l \tag{2.41}$$

Step 2. to *Step 6.* are iterated until the defect falls into the tolerance.

- Test case 3: Global-elastic local-plastic analysis of a wedge microindentation

A wedge indentation problem, which plays an important role in the mechanical characterization of materials, was selected for testing the local defect correction method for the reason that an obvious plastic zone under the indenter is expected. Fig. 2.8 shows the geometry and FEM mesh used in the simulation. A simulation domain of width $W = 600\ \mu m$ and height $H = 550\ \mu m$. The refined local domain Ω_l is highlighted in blue and located just beneath the indenter with a dimension of $150\ \mu m \times 55\ \mu m$, on which constitutive equations for linear hardening plasticity is applied. Constitutive equations for elasticity is formulated on global domain with a coarse mesh.

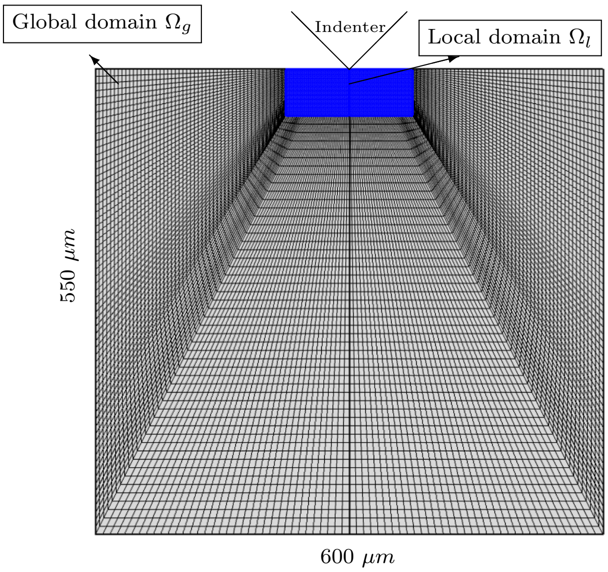

Figure 2.8: Mesh for global and local domain

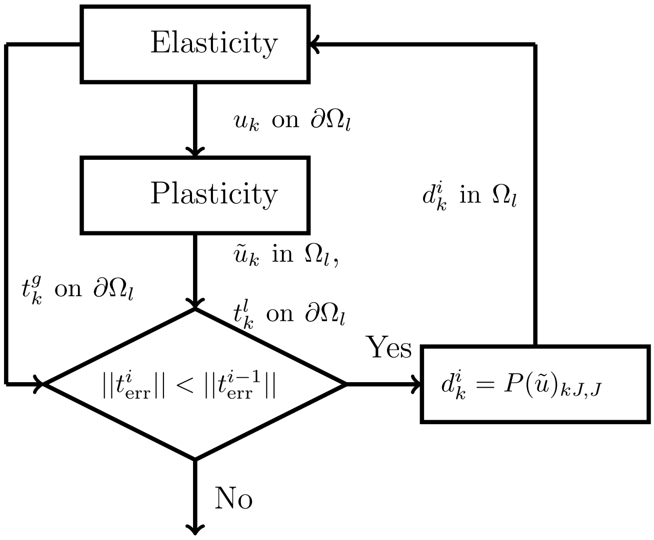

Figure 2.9: Local defect correct process

Following *Algorithm 6* introduced above, the first step is to solve the elastic problem in Ω_g to get the displacement $\boldsymbol{u}^1$ at the nodes of the global coarse mesh. By interpolating $\boldsymbol{u}^1$ on local fine mesh boundary $\partial\Omega_l$, the displacement boundary condition for the local domain is completely determined following the global analysis. Then linear hardening plasticity is solved in local domain Ω_l with displacement boundary conditions derived from previous global analysis so that displacement $\boldsymbol{u}_l$ in Ω_l is obtained. Then interpolate $\boldsymbol{u}_l$ on the global nodes in Ω_g to get $\tilde{\boldsymbol{u}}$. After that, plug $\tilde{\boldsymbol{u}}$ into the global PDE of elasticity to compute the residual $\boldsymbol{d}$. At last, add the residual to the original volume force in the local domain Ω_l as the new volume force for the next iteration. The entire iteration process is summarized in

Fig. 2.9.

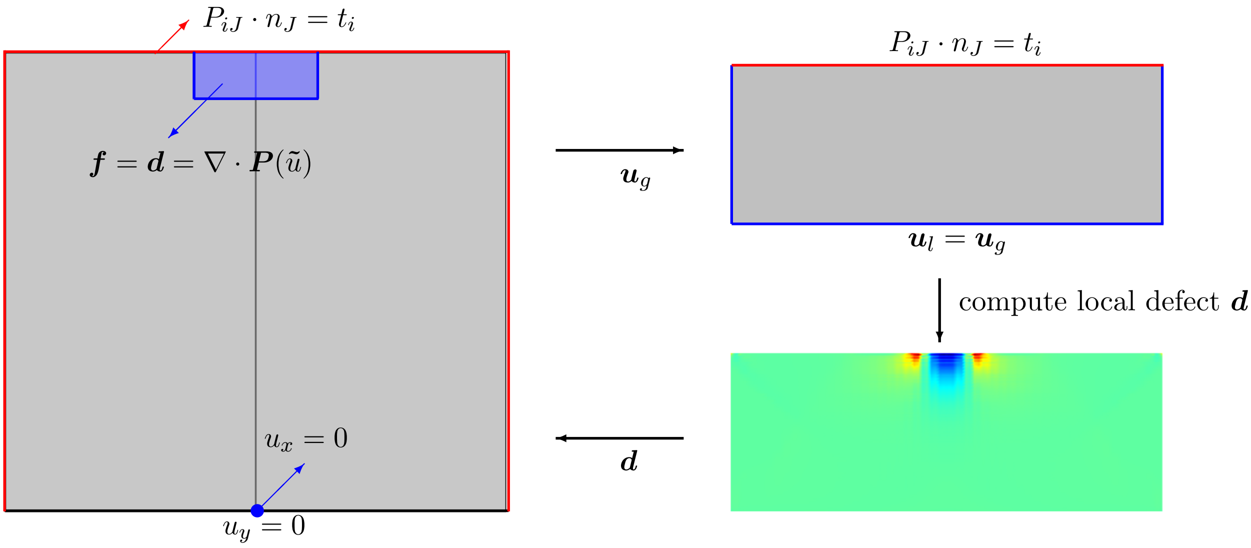

(a) Global domain (b) Local domain

Figure 2.10: Boundary conditions

Boundary conditions of both global and local analysis are illustrated in Fig. 2.10. For the global elastic analysis, the bottom boundary is constrained in vertical direction and the mid-point of the bottom is completely fixed. The two lateral boundaries are traction free. The top surface is indented by a rigid 90° wedge with a tip radius of $R = 10\ \mu m$. The indenter is pressed into the material with a depth of 5 μm. The indentation contact problem is solved by applying a traction as a function of the signed distance between indenter and material top surface:

$$t_i = \frac{KE}{h} H^*(d(x)) n_i \tag{2.42}$$

where K is a constant indicating the hardness of the indenter which is selected to be 0.3. E is the Youngs Modulus of the material. h stands for the average mesh element size of sample top boundary. $\frac{KE}{h}$ is interpreted as penalty factor in the penalty method and is determined based on both ease of convergence and solution accuracy. The low penalty factor usually leads to faster convergence but more inter-penetration between contact surfaces. $d(x)$ is the signed distance of x on the top surface from its closest point on the indenter, and H^*

is a smooth Heaviside step function. $\boldsymbol{n}$ is the normal to the top surface in the deformed configuration, which can be computed from $\boldsymbol{N}$ in the reference frame via $n_i = JG_{Kj}N_K$.

In addition to the local defect correction method, conventional elasto-plastic analysis over the whole domain with a fine mesh was also implemented for comparison and verification. The number of degrees of freedom and of elements used in both methods are listed in Table 2.5. The 8-node quadratic quadrilateral elements are used in each model. The DOF can be computed from the product of number of nodes and number of variables solved on each node. The DOF needs to be solved can be cut over half by using the global-local method. The Von-Mises stresses in both the global and local domains after the first iteration is plotted in Fig. 2.11. The stress in the local domain is much smaller than in the global domain due to the implementation of a linear hardening plastic model. Fig. 2.12 shows a comparison between the Von-Mises stress in the local refined domain after the last iteration with the LDC method and the stress obtained by the global elasto-plastic model, indicating good agreement. In addition, Fig. 2.14 shows the traction mismatch between the global and local domain at the interface. The relative traction difference is computed as $\int_{\partial\Omega_{\text{int}}} ||\bar{\boldsymbol{t}}_g - \bar{\boldsymbol{t}}_l||/||\bar{\boldsymbol{t}}_l||dl$, where $\bar{\boldsymbol{t}}_g$ and $\bar{\boldsymbol{t}}_l$ represent traction vectors on the interface computed from global and local models respectively. The difference keeps on decreasing as the number of iterations increases, indicating that the local defect correction method converges and eliminates the traction mismatch at the interface.

Model	DOF	Number of quadrilateral elements
Global plasticity	795,802	15,000
Global elasticity	120,802	15,000
Local plasticity	132,902	2,500

Table 2.5: Summary of computation information.

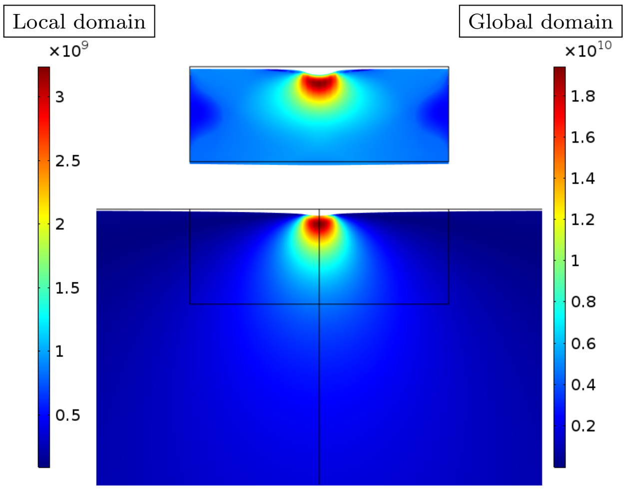

Figure 2.11: Von-mises stress [Pa] in both the global and local domains after the first iteration

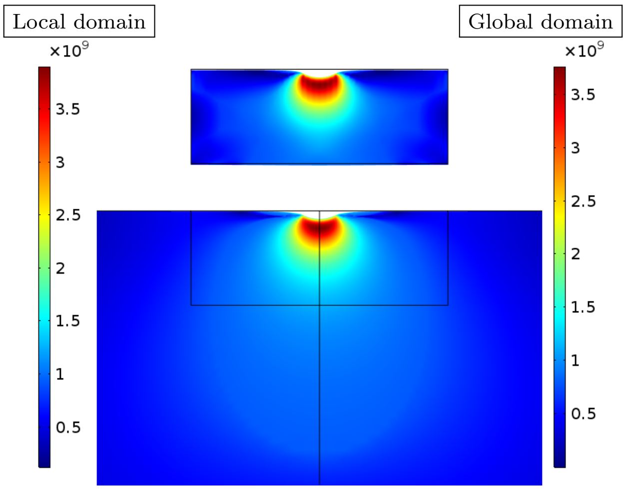

Figure 2.12: Von-mises stress [Pa] in the local domain after the last iteration, compared with the global plasticity domain

The improvements of the solution during iterations can be further examined from Fig. 2.13 by plotting the relative error of displacements at the global-local interface which is computed as $\int_{\partial\Omega_{\mathrm{top}}} ||\bar{\boldsymbol{u}} - \bar{\boldsymbol{u}}_0||/||\bar{\boldsymbol{u}}_0||dl$, where $\bar{\boldsymbol{u}}$ is the displacement vector obtained from LDC method while $\bar{\boldsymbol{u}}_0$ represents the one computed from global elasto-plastic model. As the number of iterations increases, the displacement solution approaches the result of the global elasto-plastic analysis, ending up with an error of 6%.

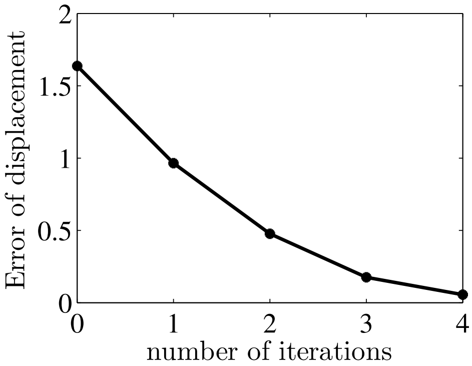

Figure 2.13: Relative error in the y-displacement along the top boundary.

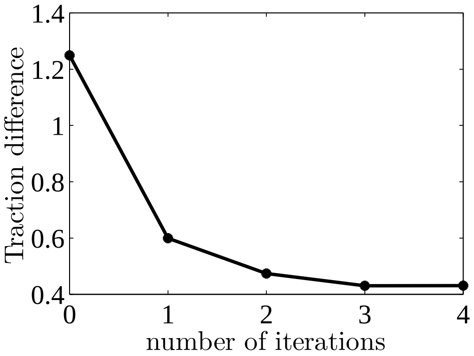

Figure 2.14: Relative traction difference at the global-local interface.

One major drawback of this method is that it requires several iterations to reach a relatively accurate solution. In addition, the traction mismatch at the interface is still difficult to be eliminated though can be reduced as the number of iterations increases. To overcome these drawbacks, a more fundamental and self-consistent approach using a variational principle and Lagrangian multiplier is reviewed next.

2.3.3 Variational Principle for Partitioned Structural Systems

The two methods introduced in previous sections are using either sequential process (multigrid method) or iterative process (local defect correction method) to connect the local domain to the global domain. However, neither of them solves both global and local domains together in a more self-consistent way. To solve this problem, a continuum-based variational principle is presented by K. C. Park *et al.* [28] for the formulation of the discrete governing equations of partitioned structural systems. The interface is treated by a displacement frame and a localized version of the method of Lagrange multipliers. One important application of this method is the treatment of physically heterogeneous subdomains and nonmatching meshes that arise from independent mesh refinement and global-local analysis.

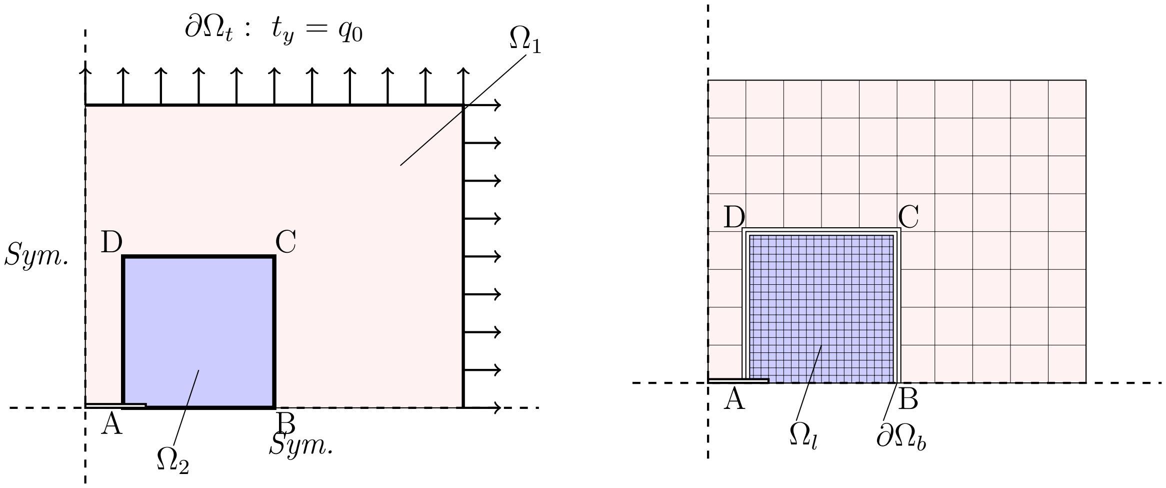

(a) Global and local domains with boundary conditions

(b) Partitioned domains with nonmatching meshes

Figure 2.15: Partitioned structural systems

Fig. 2.15 shows a typical example for which this method can be applied. The entire domain Ω is partitioned into two subdomains Ω_1 and Ω_2, unlike the two previous methods where global and local domain are overlapped with each other. An internal boundary $\partial\Omega_b$, named partition frame, is placed between Ω_1 and Ω_2. The displacement of $\partial\Omega_b$ are to be varied independently from those of the subdomains, and are called $\boldsymbol{u}_b$. The partition frame is attached to the adjacent subdomains by Lagrangian multiplier fields $\boldsymbol{\lambda}_l$.

With the additional displacement fields and Lagrangian multipliers on the interface, a modified form of the potential energy functional is shown as follows [28]:

$$\Pi_{\mathrm{PEM}}(u_i, \lambda_{l_i}, u_{b_i}) = \Pi_{\mathrm{PE}} - \pi_u = \sum_m \Pi_{\mathrm{PE}}^m - \sum_m \pi_u^m, \tag{2.43}$$

$$\Pi_{PE}^m = \int_{\Omega^m} [\psi(u_i^m) - u_i^m f_i^m] d\Omega - \int_{\partial\Omega_t^m} u_i^m t_i^m dS \tag{2.44}$$

$$\pi_u^m = \int_{\partial\Omega_b^m} \lambda_{l_i}^m (u_i^m - u_{b_i}) dS \tag{2.45}$$

where m is the index of subdomains. The interior fields of subdomain Ω^m, considered as an isolated entity, are: displacements u_i^m and prescribed body force f_i^m. Its boundary $\partial\Omega^m$ can be generally decomposed into $\partial\Omega_u^m$, $\partial\Omega_t^m$ and $\partial\Omega_b^m$. $\partial\Omega_u^m$ and $\partial\Omega_t^m$ are portions of $\partial\Omega^m$ where displacement and tractions are specified respectively. $\partial\Omega_b^m$ is the interface with other subdomains.

Π_{PE}^m is the localized strain energy of subdomain m as Eq. 2.26 shows, and has nothing to do with fields in other subdomains. The only inter-partition connection is through $\boldsymbol{u}_b$ in π_u^m, which is called interface potential. Note that if the compatibility condition $u_i^m = u_{b_i}$ is enforced a priori, π_u drops out and the ordinary functional Π_{PE} results.

Take the first variation of the functional Π_{PEM}:

$$\begin{aligned}\delta\Pi_{\mathrm{PEM}} = &\int_{\Omega_m} \left[\frac{\partial\psi}{\partial E_{KL}} \frac{\partial E_{KL}}{\partial F_{iJ}} \delta F_{iJ} - b_i^m \delta u_i^m\right] d\Omega - \int_{\partial\Omega_t^m} t_i^m \delta u_i^m dS \\ &- \int_{\partial\Omega_b^m} (u_i^m - u_{b_i}) \delta\lambda_{l_i}^m dS - \int_{\partial\Omega_b^m} \lambda_{l_i}^m (\delta u_i^m - \delta u_{b_i}) dS \end{aligned} \tag{2.46}$$

The functional in Eq. 2.43 can provide a tool to treat nonmatching meshes and displacement fields. However, due to the heterogeneous constitutive models in subdomains, if displacement are matched at the interface, then the traction wouldn't be matched. Therefore, further work needs to be done to improve the interface matching.

- Test case 4: Global-local analysis of a wedge microindentation problem

The test case used for the local defect correction method as shown in Fig. 2.8 was also used for testing this variational principle method for comparison. Fig. 2.16 shows the displacement u_y along the top traction-free surface obtained from two different methods — global elasto-plastic analysis and Lagrangian multiplier method based on the variational principle discussed in this section. It can be observed that results from variational principle method agree well with results from global elasto-plastic analysis with an average error of 9%, which is less than the error of results obtained from local defect correction method after three iterations (18%) but greater than that after four iterations (6%), as shown in Fig. 2.13. In addition, since Lagrangian multiplier was used at the global-local interface with the physical meaning of traction, the traction mismatching problem was resolved automatically with variational principle method.

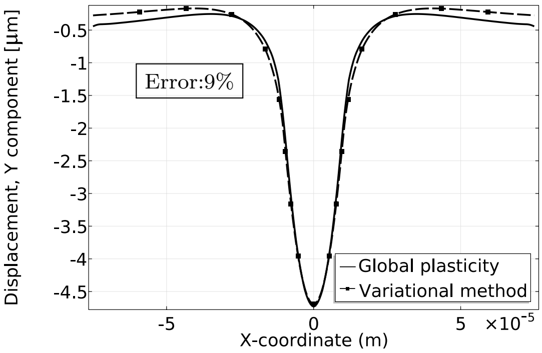

Figure 2.16: Displacement in the y-direction along the top boundary of local region.

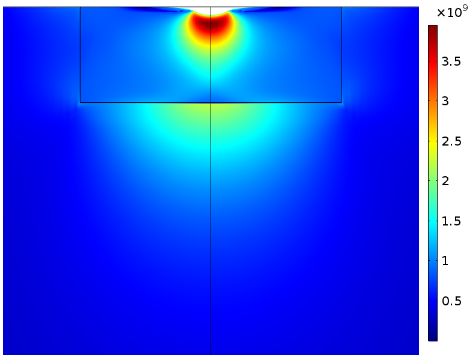

Figure 2.17: Von mises stress [Pa]

It can be concluded that the advantage of variational principle method over the local defect correction method is that it solves the global and local domains at the same time without iterations and the traction can be matched at the global-local interface. However, as Fig. 2.17 shows, the stresses are still unmatched at the global-local interface. This problem can be resolved by the proposed method discussed in Sec. 2.4.2.

2.4 A Proposed Multiphysics-Multiscale Methodology

The following discussion is intended to provide a practical strategy for performing multiphysics simulations, where the objective would be sufficient accuracy with computational efficiency. First, the approach used for multiphysics simulations is discussed, then a variational method for coupling local-global regions with heterogeneous constitutive equations will be presented.

2.4.1 Multiphysics

Step 1. DOF estimation

The solution speed and memory requirements are strongly dependent on the number of degrees of freedom (DOF) in the model. It is often desirable to estimate the DOF based on the number of elements in the model.

Generally, the DOE is given by the number of nodes multiplied by the number of dependent variables. The relation between the number of nodes and the number of elements depends on the order of the elements and differs between 2D and 3D.

	2D		3D	
Element type	Triangular	Quad	Tetrahedral	Hexahedral (brick)
Linear	0.5	1	0.2	1.2
Quadratic	2	4	1.4	8.5
Cubic	4.5	9	4.6	28

Table 2.6: The ratio of number of nodes to number of elements

The total number of DOF is then computed by #nodes × #dependent variables. The number of DOFs is determined by to the amount of memory a particular model will need though is not the only factor determining the memory requirements and the solution time of a problem.

Step 2. Memory requirements prediction

It is not just the number of DOFs, but also the sparsity of the system matrix that will affect the amount of memory needed to solve the problem. The memory needed will depend on the geometry, mesh, element types, and couplings between physics.

Start by solving smaller models with the same physics, or use a coarser mesh to solve the same model. Monitor the memory requirements and DOFs for these smaller models. Fit a second order polynomial curve to this data to roughly predict how much memory you will need for the actual problem that you want to solve. It's important to know the size of the models that need to be solved.

Step 3. Problem simplification

- Order of discretization shape function

\- *Single-physics model*
For the purposes of this discussion, lets consider just the set of PDEs governing common single-physics problems that exhibit no variation in time. We can put all of these PDEs into one of two broad categories:

1. Poisson-type
   Poisson-type PDEs are used to describe heat transfer in solids, solid mechanics, and flow in porous media governed by Darcys law. Such governing PDEs are all of the form:

   $$\nabla \cdot (-D\nabla u) = f \tag{2.47}$$

   Note that this is a second-order PDE, thus second-order (quadratic) elements are preferred for the first try.

2. Transport-type
   Transport-type PDEs are used to describe chemical species transport as well as heat transfer in fluids and porous media. The governing equations here are quite similar to Poissons equation, with one extra term - a velocity vector:

   $$\nabla \cdot (-D\nabla u + \boldsymbol{v}u) = f \tag{2.48}$$

The extra velocity term results in a governing equation that is closer to a first-order PDE. This is one of the reasons why the default choice is to use first-order (linear) elements for these PDEs. Note that for fluid flow problems where the Reynolds number is low, the default is to use the so-called P2 + P1 elements that solve for the fluid velocity via second-order discretization and solve for the pressure via first-order discretization.

As long as one is working with only single physics, it typically does not matter too much which element order you use as long as you remember to perform a mesh convergence study. The solutions with a different element order may require quite varying amounts of memory and time to solve, but they will all converge toward the same solution with sufficient mesh refinement. However, when we start dealing with multiphysics problems, things become a little bit more complicated.

- *Coupled-physics model*

1. Conjugate heat transfer

   The *Conjugate Heat Transfer* interface is composed of two physics interfaces: the *Heat Transfer* interface and the *Fluid Flow* interface. The *Fluid Flow* interface (whether laminar or turbulent) uses linear element order to solve for the fluid velocity and pressure fields. The *Heat Transfer* interface solves for the temperature field in the fluid as well as the temperature field in the solid. The same linear element discretization is used throughout the temperature field in both the solid and fluid domains.

2. Thermal stress

   The other common case where a multiphysics coupling uses different element orders from a single-physics problem is when computing thermal stresses. The two physics are related by the following equation:

$$\epsilon = \frac{1}{2}[(\nabla \boldsymbol{u})^T + \nabla \boldsymbol{u}] - \alpha(T - T_0) \tag{2.49}$$

   By default, we solve for the structural displacements using quardratic discretization, but strains are computed from the gradients of displacement fields, which turn out to be first-order. Hence, the temperature field discretization should also be lowered to a linear order. Therefore, for the thermal stress multiphysics coupling, the default is to use linear discretization for the temperature and quadratic discretization for the structural displacements.

2.4.2 Hu-Washizu Global-Local Analysis Approach

Following the discussion in Sec. 2.3.2 and 2.3.3, where local defect correction method and the method with variational principle were introduced for heterogeneous systems. The local defect correction method is able to reduce the traction difference at the interface by iterations but not totally eliminate the difference. In addition, the number of iterations is undetermined and the iteration process is time-consuming. The method with a variational principle is able to match the tractions at the interface by introducing Lagrangian multipliers. However, the individual stress components are still mismatched. To achieve compatibility of displacement, traction and stress fields at interfaces in global-local methods, a new approach that is based on the Hellinger-Reissner (HR) variational principle [29] is proposed. A simple 2D test case will be presented for model verification.

- Model Formulation

The multifield variational principle provides the possibility of matching both displacements and stresses at the interface between global and local domains since both displacement and stress fields can be varied independently. The most general form of multifield variational principle (also known as the Veubeke-Hu-Washizu (VHW) principle) allows simultaneous variation of displacements, strains and stress. The energy potential functional is expressed as:

$$\Pi_{\mathrm{VHW}}(u_i, \sigma_{ij}, \epsilon_{ij}) = \int_{\Omega} \left[\sigma_{ij}(\epsilon'_{ij}(u_{ij}) - \epsilon_{ij}) + W(\epsilon_{ij}) - b_i u_i\right] d\Omega - \int_{\partial\Omega_t} \hat{t}_i u_i dS \qquad (2.50)$$

where W is the strain energy density, u_i, σ_{ij} and ϵ_{ij} are three independent fields, ϵ'_{ij} is in terms of displacement field and expressed as $\frac{1}{2}(u_{i,j} + u_{j,i})$. Since there is no need to match the strain field if the displacement field is matched with a strain-displacement relationship as a prior, the Hellinger-Reissner (HR) variational principle [30] is more suitable for the multiscale framework, where displacements and stresses are the two independent fields. This implies the existence of six independent variables instead of two (u_i, σ_{ij}, $i, j = 1, 2$), which need to be solved for in a 2D problem. The HR energy functional can be obtained from the VHW functional by eliminating the strain variable, and the using the complementary energy density W^*, one gets in terms of the stress field:

$$\Pi_{\text{HR}}(u_i, \sigma_{ij}) = \int_{\Omega} \left(\sigma_{ij}\epsilon'_{ij}(u_{ij}) - W^*(\sigma_{ij}) - b_i u_i\right) d\Omega - \int_{\partial\Omega_t} \hat{t}_i u_i dS \tag{2.51}$$

Taking the first variation of Π_{HR} gives:

$$\delta\Pi_{\text{HR}} = \int_{\Omega} \left[(\epsilon'_{ij}(u_{ij}) - \frac{\partial W^*}{\partial \sigma_{ij}})\delta\sigma_{ij} + \sigma_{ij}\delta u_{i,j} - b_i \delta u_i\right] d\Omega - \int_{\partial\Omega_t} \hat{t}_i \delta u_i dS \tag{2.52}$$

The drawback of the HR variational principle is that the complementary strain energy density W^* needs to be explicitly expressed by stress components, which is possible only for a linear elastic model. Thus, the HR variational principle needs to be incorporated into a linear elasticity framework. If we have two domains (global and local) only, then linear elastic model with HR variational principle needs to be used in the global domain. Coupling between the global and local domains is realized by displacement, traction and stress boundary conditions at the interface, as Eq. 2.53 and Fig. 2.18 shows.

$$\begin{cases} \boldsymbol{u}_l = \boldsymbol{u}_g, \quad \boldsymbol{\sigma}_l = \boldsymbol{\sigma}_g & \text{on } \partial\Omega^l_{\text{int}} \\ \boldsymbol{t}_g = \boldsymbol{\sigma}_l \cdot \boldsymbol{n} & \text{on } \partial\Omega^g_{\text{int}} \end{cases} \tag{2.53}$$

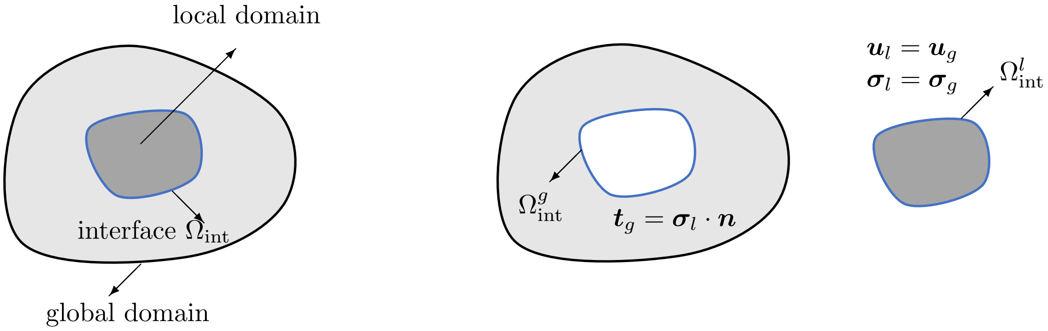

Figure 2.18: Boundary conditions on global-local interface

- Test case 5: Hu-Washizu principle-based global-local analysis of a wedge microindentation problem

To verify the proposed approach, a simple 2D problem was solved by both HR variational principle-based and potential energy (PE) variational principle-based methods discussed in Sec. 2.3.3 for comparison. To keep consistent with the test cases of other global-local methods, the wedge indentation problem was again picked for model verification. The material simulated was assumed to be Nickel superalloy, corresponding material properties can be found in Table 2.8. The model geometry, dimensions, mesh and global boundary conditions are the same as the ones of models implemented in previous sections as shown in Fig. 2.8 and 2.10.

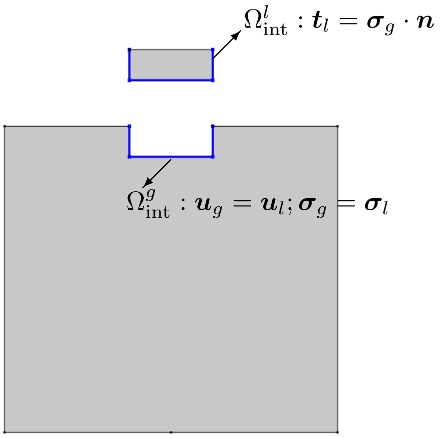

Figure 2.19: Boundary conditions on global-local interface

One expected advantage of HR principle-based approach over the PE principle-based approach is the capability of matching all stress components at the global-local interface. Von-Mises stresses obtained by both methods are plotted in Fig. 2.20(a) and Fig. 2.20(b) for comparison. It can be clearly seen that HR variational principle can help smooth the stresses at the interface.

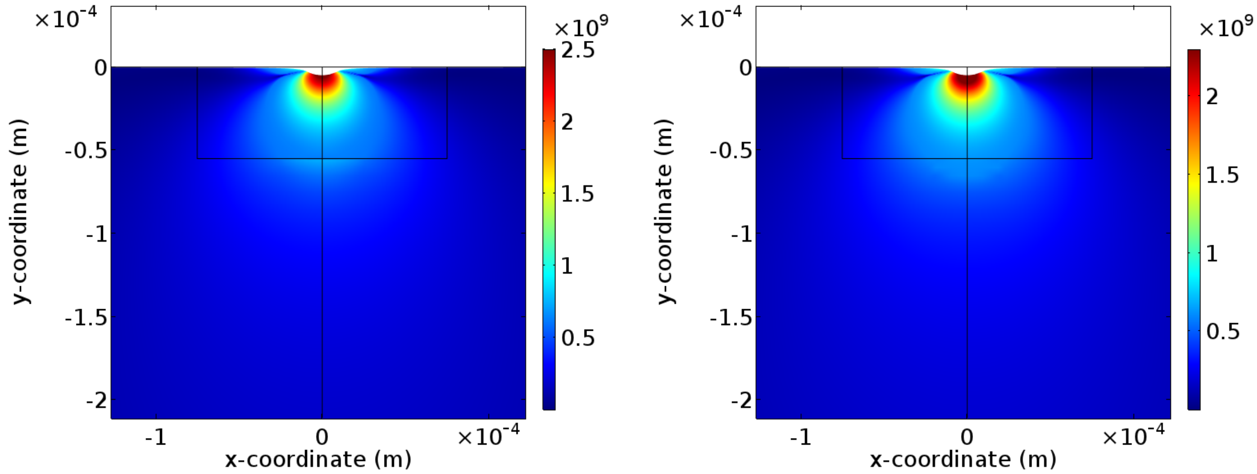

(a) PE variational principle

(b) HR variational principle

Figure 2.20: Von-mises stresses [Pa] at 5 μm indentation depth obtained from two methods.

A more quantitative comparison can be done by plotting the two stress components σ_{xx} and σ_{yy} at the global-local interface, as shown in Fig. 2.21 and Fig. 2.22. which could further demonstrate that stresses in global and local domain are matching at the interface with the help of HR principle.

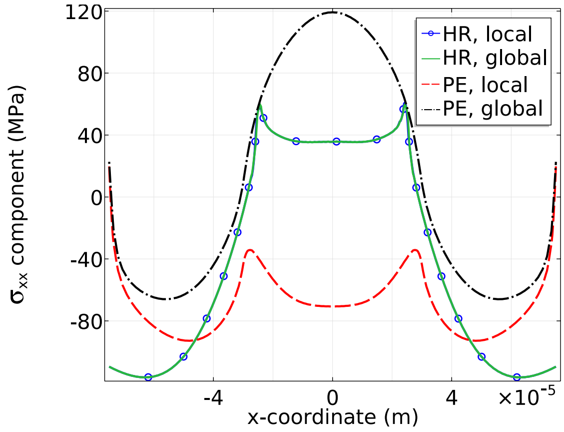

Figure 2.21: σ_{xx} at interface.

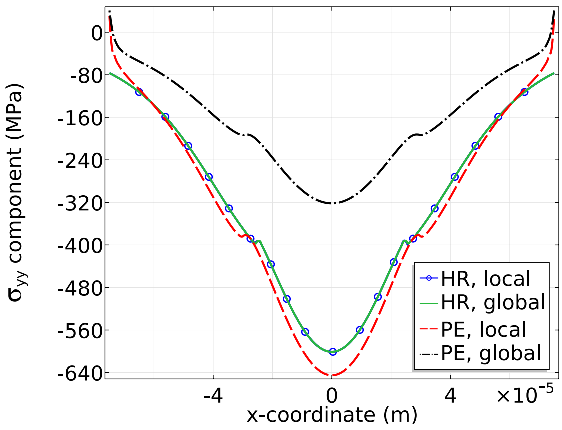

Figure 2.22: σ_{yy} at interface

The proposed multiscale method is compared to the conventional approaches reviewed in the first half of this section. Listed in Table 2.7 are the computing time and DOF needed for the solution of each method. It can be clearly seen that applying the elasto-plasticity to the entire domain without any multiscale method is relatively computationally expensive with the largest number of DOFs among all four models. The local defect correction method can split the total DOFs into two parts, thus has the potential to handle the system with a large number of DOFs. However, the total computing time depends on the number of iterations, thus the speed of simulation is not necessarily increased. The Lagrange multiplier method reduces the DOFs by more than half, and shortens the computing time. Lastly, the proposed method which can provide the most accurate results among all the multiscale methods is not able to reduce the number of DOFs and computing time significantly due to the additional DOFs for stress components. However, it achieves a balance between accuracy and efficiency of simulation.

	Degree of Freedom	Computing time [sec]
Global Elasto-plasticity	795,802	71
Local defect correction	120,802+132,902	119 (5 iterations)
Lagrange multiplier method	345,802	47
Hu-Washizu principle-based method	553,608	65

Table 2.7: DOF and computation time of the indentation problem by various models

2.4.3 Coupling Crystal Plasticity with Conventional Plasticity

The heterogeneous plastic deformation of crystals requires a method that is sensitive to crystal orientations and specific slip directions. Thus, we need to take one step further from traditional isotropic plasticity to crystal plasticity, where such information would be available. Details of crystal plasticity models will be discussed in Chapter 4. The focus of this section is to couple any crystal plasticity model with isotropic plasticity within our multiscale framework. A combined continuum-crystal plasticity FEM approach has been adopted for modeling of a three-point bend test by Dunne, *et al.* [31]. One of the difficulties in the combined crystal and conventional plasticity models is the inconsistency of material properties at the interface boundary between the two regions leading to discontinuities. One simple coupling method as adopted in Dunne's work is to choose the critical resolved shear stress which leads to macroscopic yielding at a stress approximately equal to the continuum yield stress so as to minimize the discontinuity. However, it's difficult to determine the value of critical resolved shear stress to match the yield stress in the two regions without several trial runs. In addition, even if the yield stress matches, it's difficult to guarantee the consistency of each stress component since the flow rule is usually dependent on some effective stresses, like Von-Mises stress for J_2 continuum plasticity.

A plasticity model based on the continuum dislocation theory proposed by M. Baitsch, *et al.* [32] provides the potential of a better approach to couple crystal plasticity with isotropic plasticity. The model includes the microstructure energy U_m, which includes the interaction energy between dislocations and the self-energy of dislocations, assumed to be [33]:

$$U_m = kG\ln\frac{1}{1-\frac{\varrho}{\varrho^s}} \tag{2.54}$$

where ϱ is the scalar dislocation density, which can be expressed by plastic slip, k is a dimensionless parameter assumed to be 10^{-4}, G is the shear modulus and ϱ^s is a saturation dislocation density assumed to be 10^{14} [m^{-2}]. Now the energy functional contains two parts — the strain energy and the microstructure energy. By minimizing the energy functional, both the displacement field and the plastic slip can be solved. The plastic slip can be the bridge to link crystal plasticity to conventional plasticity by matching the plastic slip at the interface. The crystal plasticity model is applied in the local refined domain, providing the plastic slip information at the global-local interface for the global conventional plasticity model in the form of boundary conditions. Detailed equations care discussed next.

- Model formulas

Large deformation kinematics through the multiplicative split of the deformation gradient tensor is adopted, where the incompatible plastic deformation gradient $\boldsymbol{F}^P$ can be expressed as (more details will be discussed in Chapter 4).

$$\boldsymbol{F}^P = \sum_{\alpha} \gamma^{\alpha} \boldsymbol{s}^{\alpha} \otimes \boldsymbol{n}^{\alpha} + \boldsymbol{I} \tag{2.55}$$

where γ^{α}, $\boldsymbol{s}^{\alpha}$ and $\boldsymbol{n}^{\alpha}$ are plastic slip, slip direction and plane normal of dislocation family α respectively, $\boldsymbol{I}$ is the identity matrix.

Nye's dislocation density tensor can be computed from $\boldsymbol{\alpha} = -\boldsymbol{F}^P \times \boldsymbol{\nabla}$. For the plane strain distortion there are two non-zero components of this tensor given by

$$\alpha_{13} = F^P_{12,1} - F^P_{11,2}; \quad \alpha_{23} = F^P_{22,1} - F^P_{21,2} \tag{2.56}$$

The density of geometrically necessary dislocations (ϱ_{GND}) can be obtained by

$$\varrho_{\mathrm{GND}} = \frac{\sqrt{\alpha_{13}^2 + \alpha_{23}^2}}{b} \tag{2.57}$$

The free energy density per unit volume with continuously distributed dislocations can be expressed as

$$I(u_i, \gamma, \gamma_{,K}) = \int_\Omega W(E^E_{ij}) + \underbrace{kG\ln\frac{1}{1-\varrho/\varrho^s}}_{\phi} d\Omega \tag{2.58}$$

where $W(E^E_{ij})$ is the elastic strain energy density, the expression of which can be selected from Table 2.1.

Eq. 2.55 - 2.57 indicate that dislocation density ϱ is in terms of the gradient of plastic slip γ^α. Taking the first variation of the energy functional (Eq. 2.58) gives

$$\delta I(u_i, \gamma, \gamma_{,K}) = \int_\Omega P_{iJ}\delta u_{i,J} + \sum_\alpha \underbrace{\frac{\partial W(E^E_{\alpha\beta})}{\partial F^P_{\gamma K}}}_{P_{iJ}F^E_{i\gamma}\delta_{KJ}} \underbrace{\frac{\partial F^P_{\gamma K}}{\partial \gamma^\alpha}}_{s^\alpha_\gamma n^\alpha_K} \delta\gamma^\alpha + \frac{\partial \phi}{\partial \varrho}\frac{\partial \varrho}{\partial \alpha_{\gamma J}} \underbrace{\frac{\partial \alpha_{\gamma J}}{\partial \gamma_{,K}}}_{-\epsilon_{JIK}s_\gamma n_I} \delta\gamma_{,K}\, d\Omega \tag{2.59}$$

where P_{iJ} is the first Piola stress tensor.

To couple this model with crystal plasticity, we need to satisfy Dirichlet boundary conditions for plastic slip at the interface so as to match the plastic slip between two different models, as shown in Fig. 2.24. The plastic slip is set to be zero on the boundaries where low stresses are expected, indicating transition to elasticity.

- Test case 6: Combined phenomenological crystal plasticity and conventional plasticity analysis of wedge micro-indentation

To examine the feasibility of the proposed coupling method, the wedge indentation test case is implemented here again. Similar to previous coupling methods, the model contains a high-stress local region modeled using phenomenological crystal plasticity, as highlighted in Fig. 2.23 and the rest of the domain is modeled using continuum plasticity, formulated in Eq. 2.59. The modeling of phenomenological crystal plasticity follows Eq. 4.8 - 4.10 with material model parameters for single-crystal Nickel superalloy listed in Table 2.8.

In addition to the proposed coupling model (Model 3), two other models: (1) phenomenological crystal plasticity coupled with elasticity (Model 1) and (2) elasto-plasticity (Model 2), were implemented for comparison.

Parameter	Symbol	Value	Unit
Elastic constant	C_{11}	252	GPa
Elastic constant	C_{12}	161	GPa
Elastic constant	C_{44}	131	GPa
Strain rate sensitivity	m	0.05	1
Reference shearing rate	$\dot{\gamma}_0$	0.001	1/s
Initial slip resistance	$\tau_{\text{crss}}\|_{t=0}$	350	MPa
Saturation slip resistance	τ_s	1500	MPa
Hardening parameter	h_0	550	MPa
Hardening exponent	a	1.3	1
Coplanar hardening ratio	$q_{\alpha\beta}$	1	1
Non-coplanar hardening ratio	$q_{\alpha\beta}$	1.4	1

Table 2.8: Material model parameters for single-crystal Nickel superalloy

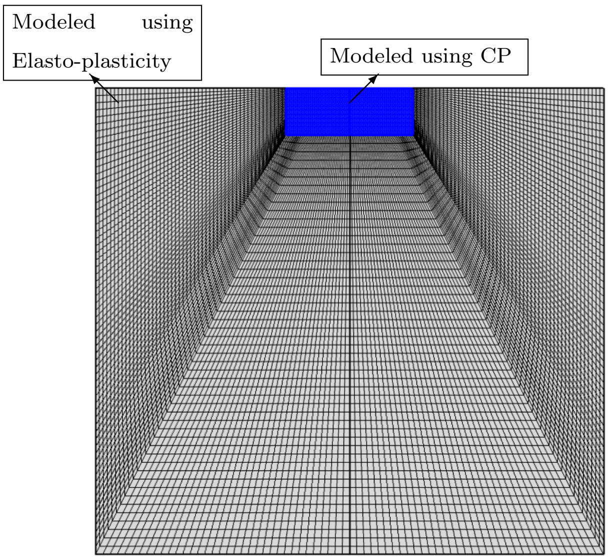

Figure 2.23: Mesh for crystal plasticity domain and elasto-plastic domain

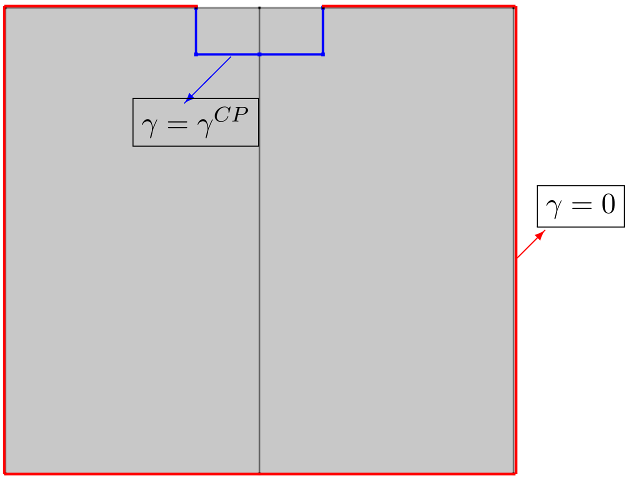

Figure 2.24: Boundary conditions for γ

The boundary conditions for indentation problem can be found in Sec. 2.3.2. Here, we present the results (Fig. 2.25 - 2.30) obtained from the three models directly. The three figures on the left column show the resolved shear stress, from which we can clearly see the discontinuity across the interface in Model 1 and 2 while the stress of Model 3 across the interface is relatively smooth. In addition, the stress-strain curves at two close-by points near the interface (shown as blue and red dots in the figure) are plotted in Fig. 2.26, 2.28, 2.30. In Model 1, the stress in the global domain, where elasticity was modeled, was much overestimated. In Model 2, yielding can be observed in both global and local domains. However, it's difficult to pick the appropriate values for yield strength and hardening modulus used in isotropic elasto-plastic model to make the two curves match with each other. Lastly, Fig. 2.30 shows the results obtained from the proposed coupling method, indicating that the stresses are matching pretty well at the interface.

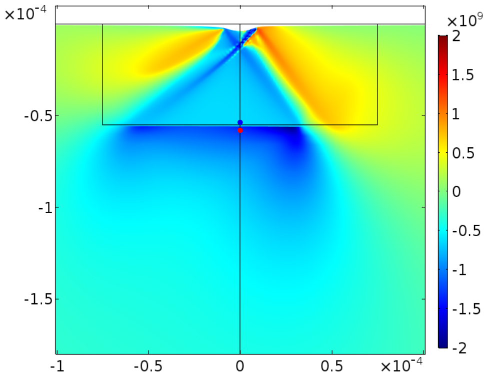

Figure 2.25: Resolved shear stress (Model 1)

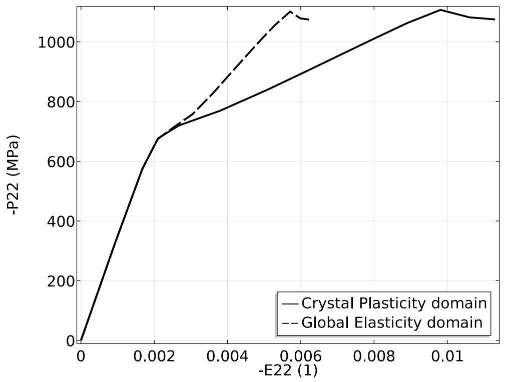

Figure 2.26: $\sigma - \epsilon$ curve at point on the interface (Model 1)

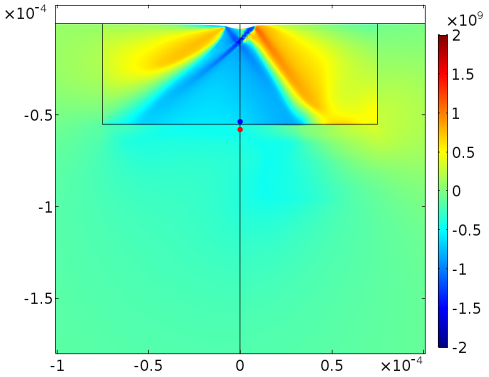

Figure 2.27: Resolved shear stress (Model 2)

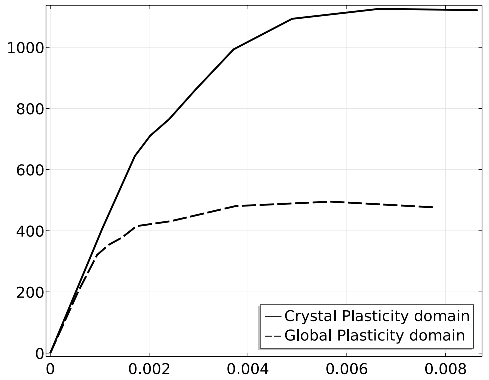

Figure 2.28: $\sigma - \epsilon$ curve at point on the interface (Model 2)

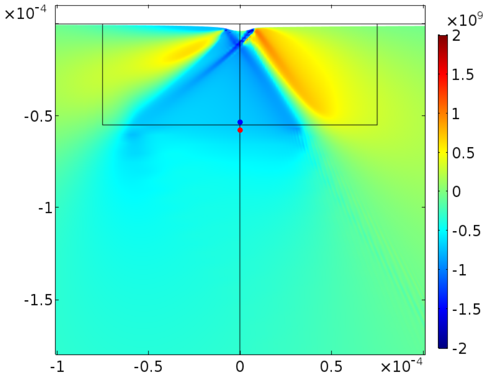

Figure 2.29: Resolved shear stress (Model 3)

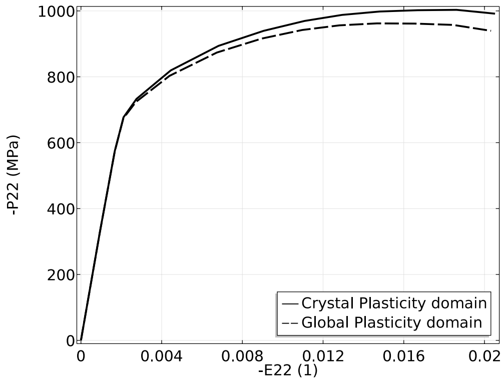

Figure 2.30: $\sigma - \epsilon$ curve at point on the interface (Model 3)

In addition, the continuity of accumulated plastic slip γ across the global-local interface is examined in Fig. 2.31. Since isotropic material models are applied in the global domains of Models 1 and 2, the anisotropic behaviors like plastic slip on different slip systems are not observed in Fig. 2.31(a) and 2.31(b), while the plastic slip obtained from our proposed coupling method shown in Fig. 2.31(c) is smooth over the entire domain.

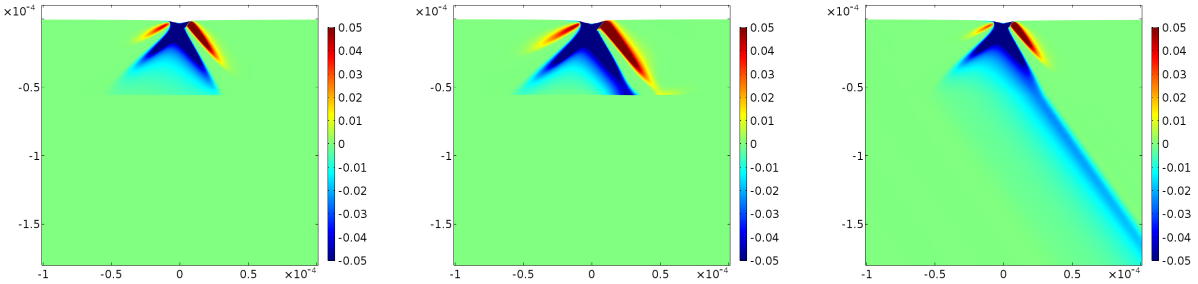

(a) Model 1

(b) Model 2

(c) Model 3

Figure 2.31: Plastic slip γ

The proposed multiscale modeling method in this section provides a general framework to couple conventional plasticity with crystal plasticity models. Although a phenomenological crystal plasticity model is used in the presented test case, physics-based or dislocation-based crystal plasticity models that will be developed further in Chapter 4 can be readily incorporated into the proposed framework.

CHAPTER 3

Multiphysics-Multiscale Design Approach

Recently, advanced concepts of multiphysics-multiscale design-by-analysis are being developed for demanding applications in mechanical, aerospace, and nuclear technologies. The rapid progress in computational methods, and the greater understanding of the influence of the microstructure on the mechanical behavior have prompted many researchers to accelerate the development of multiscale/multiphysics methods. However, progress in the *practical implementation* of such advances in actual design embodiments is still slow. Therefore, a complete design approach following the proposed multiphysics-multiscale method is discussed in this chapter.

3.1 Physics Coupling Requirements for High Heat Flux

The governing equations and boundary conditions for implementing FEM simulations of coupled heat transfer, solid mechanics and fluid dynamics, which are three critical physics involved in high heat flux components, are reviewed in Sec. 2.2. This section will focus on the coupling relationships between them. Fig. 3.1 is a schemtic of necessary couplings that must be considered in multiphysics simulations.

3.1.1 Physics Couplings Approach

Multiphysics design approach is necessary since there are three common couplings between the three physics. Details are discussed as follows.

- Non-isothermal Flow

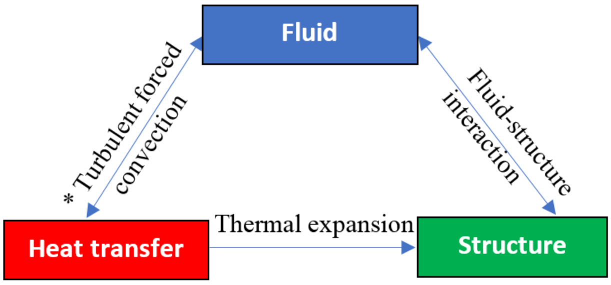

Figure 3.1: Summary of the multiphysics simulations for a typical high heat flux component

Non-isothermal flow refers to fluid motion with temperatures that are not constant. Coolants are critical to high heat flux components to bring their temperature down, and thus must be treated with non-isothermal fluid flow physics. When a fluid is subjected to a temperature change, its material properties, such as the density and viscosity, change accordingly. In addition, since the fluid transports heat, the temperature field is, in turn, affected by changes in the flow field. This two-way coupling between fluid flow and heat transfer is a phenomenon that is prevalent in processes in which components are cooled.

- Fluid-structure Interaction

Fluid-structure interaction (FSI) is a multiphysics coupling between the constitutive equations that describe fluid dynamics and structural mechanics. When a fluid flow encounters a structure, stresses and strains are exerted on the solid object, leading to deformations. If the deformations of the structure are quite small and the variations in time are also relatively slow, the fluid's behavior will not be greatly affected by the deformation, and we can concern ourselves with only the resultant stresses in the solid parts.

- Thermal Expansion

As a solid material experiences an increase in temperature, the volume of the structure is ultimately impacted by increasing, a phenomenon known as thermal expansion. With this volumetric enlargement, the elements of a solid undergo greater levels of stress. Thermal stresses can have a significant effect on a structure's strength and stability, potentially causing cracks or breaks within certain components. Such failures compromise the overall design of the structure, which can lead to possible weakening and deformation. Thermal expansion can usually be simulated by one-way coupling method since the deformation of structure has negligible effect on heat transfer unless contact or delamination happens.

A complete design process for divertor in DEMO is used as an example for demonstrating the multiphysics optimization design. In this example, Fluid-Structure Interaction is easy to handle since the deformations of structure are quite small thus one-way coupling is accurate enough. Therefore, same as Thermal Expansion, FSI can be segregated as an individual step following the heat transfer and fluid dynamics study. As a result, the most challenging part is coupling heat transfer in solids & fluids and fluid dynamics. Two methods are proposed here.

3.1.2 The Case for Fluid-Thermal Coupling

To model a conjugate heat transfer problem with turbulent flow, two different approaches are presented here. The first one includes the turbulent fluid-thermal interaction. The second approach is a simplified one using a heat transfer coefficient correlation to determine the heat transfer at the fluid-cooled side of the wall. The first approach gives more accurate results while the second approach is less computationally expensive. But the heat transfer coefficient correlations used in the second approach work well only under certain circumstances.

In this section, the formulas used in both approaches are firstly introduced, followed by two test cases for model validation. The first one is a heat transfer problem in the first wall of ITER Helium-Cooled-Pebble-Bed Test Blanket Module (HCPB TBM), which is a single-sided heated case. Three modeling approaches (one with 3D CFD, the other two with constant and varying heat transfer coefficient respectively based on the correlation) were implemented and the results of which were compared to the experimental data obtained from [34]. The results suggest that conjugate heat transfer with 3D CFD approach is necessary for simulating cooling of single-sided heated structures which have strong asymmetry of heat loading. The second test case is cooling a double-sided heated structure which represents the cases where structure is in the environment with relatively uniform temperature. The heat transfer coefficient obtained from the approaches with and without 3D CFD simulation were compared to each other and turned out to be a good fit. These two test cases could guide us to select the appropriate approach for different circumstances to achieve balance between accuracy and computational efficiency of simulation. The detailed conclusions are drawn at the end of this section.

- Turbulent Forced Convection Model Formulation

(1) *Conjugate heat transfer including the fluid dynamics*

The model works with following equations:

a. Navier-Stokes equations in the fluid domain (k-ϵ equations)
   - Normal flow pressure at the outlet
   - Specified velocity at the inlet
   - Logarithmic wall function at the interface boundaries

b. Heat balance equations in the fluid and solid wall
   - Specified temperature at the inlet
   - Convection at the outlet
   - Thermal wall function at the interface

Heat transfer in solids and fluids are connected through a heat flux boundary condition, the thermal wall function.

$$q = \frac{\rho C_p C_\mu^{1/4} k_w^{1/2} (T_w - T)}{T^+} \tag{3.1}$$

where C_μ and k_w are model constants. T_w is the wall temperature, while T is the bulk temperature of the fluid. T^+ is related to the dimensionless wall distance and defined as follows:

$$T^+ = \frac{Pr_T}{\kappa} \ln(y^+) \beta \tag{3.2}$$

where the dimensionless wall distance y^+ is given by:

$$y^+ = \frac{\rho \delta_w C_\mu^{1/4} k_w^{1/2}}{\mu} \tag{3.3}$$

where Prandtl number $Pr_T = \frac{C_p \mu}{k}$ and κ is the Von Karman constant, which is set to be 0.41. β is a constant set to 3.27.

(2) *Convection modeled as a boundary condition without fluid dynamics*

This simplified model uses only an energy balance for the solid wall. The heat transfer at the fluid/solid interface is calculated with correlations. This means it is not necessary to model the fluid domain.

The model works with the following equations:

a. Heat balance equations in the solid

- Specified temperature/heat flux on certain boundaries
- Flux boundary condition at fluid/solid interface using a heat transfer coefficient

$$Nu = 0.037 Re^{0.8} Pr^{1/3} (\mu/\mu_s)^{0.14} \tag{3.4}$$

$$Re = \frac{\rho U D}{\mu} \tag{3.5}$$

$$Pr = \frac{\mu C_p}{k} \tag{3.6}$$

$$h = \frac{Nu \cdot k}{D} \tag{3.7}$$

$$q_w = h(T_w - T_{\text{bulk}}) \tag{3.8}$$

where q_w and T_w denote the heat flux and wall temperature averaged over the channel wall surface, while T_{bulk} stands for the fluid bulk temperature obtained by volume averaging of 3D CFD data for the local coolant temperature. This approach can be further simplified using a constant heat transfer coefficient, which is widely used in multiphysics simulation [35].

- Test case 1: Cooling single-sided heated structure

M. Ilic *et al.*[34] reported the investigations of heat transfer in the first wall of HCPB TBM for ITER. The investigations have been performed both experimentally and numerically, demonstrating that modeling forced convection as a boundary condition without CFD approaches failed in comparison with experimental data while the approach with CFD simulation is well fitted. The experimental data for the Eurofer temperature can be used for verifying the models discussed above.

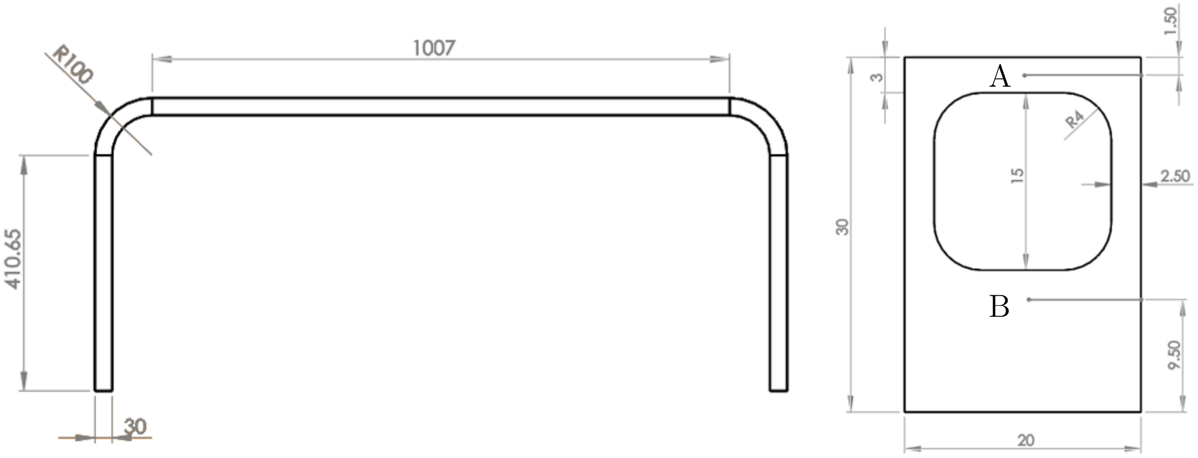

Figure 3.2: Geometry of a cooling channel in the first wall of HCPB TBM

The geometry and dimensions of the cooling channel used in the HCPB TBM are shown in Fig. 3.2. All the thermal-hydraulic boundary conditions applied in the numerical models are consistent with the experiment performed in [34], as listed in Table 3.1.

$\dot{m}$ [g/s]	T_{in} [°C]	q_{FW} [kW/m^2]	P_{He} [MPa]
80	300	269.4	15.5

Table 3.1: Thermal-hydraulic boundary conditions for HCPB TBM first wall

As discussed in the previous section, three different modeling approaches were performed, which are: (1) conjugate heat transfer with 3D CFD (2) applying varying heat transfer coefficient obtained from correlations without CFD (3) applying constant heat transfer coefficient without CFD. The results obtained from all of these three approaches were compared to the experimental results for validation.

In the experiment, the temperature was measured along two paths throughout the cooling channel structure, whose positions are denoted as A and B in Fig. 3.2. Path A is closer to the surface facing the heat flux (front side) while path B is on the other side of the coolant (back side). The longitudinal profiles of temperature along both paths obtained from experiments and simulations with three different approaches are presented and compared in Fig. 3.3.

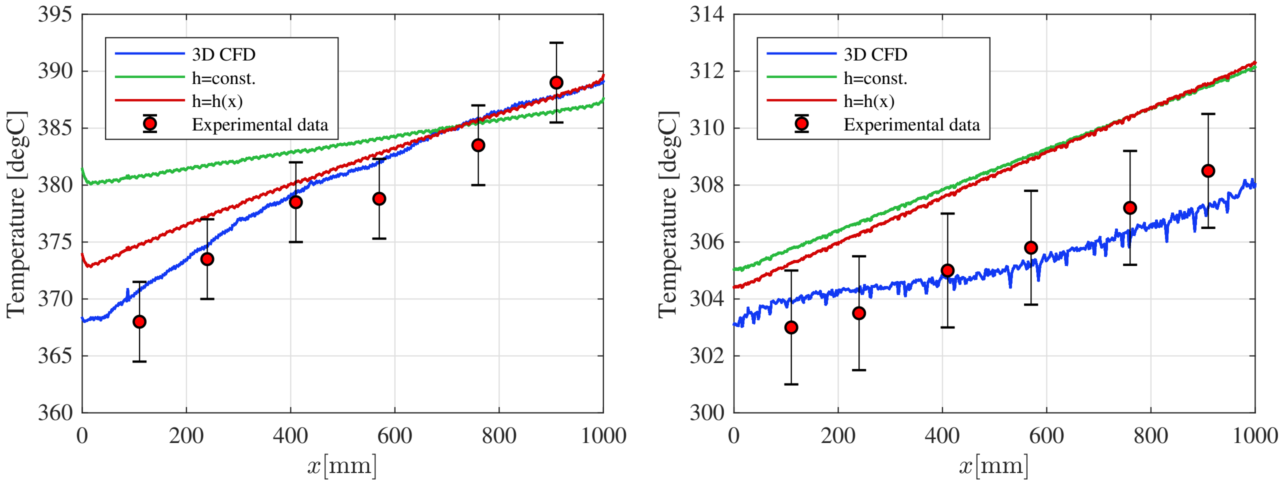

(a) Front side (b) Back side

Figure 3.3: Longitudinal temperature profiles in the front (a) and back (b) part

It can be clearly seen that results obtained from the approach with 3D CFD fit the experimental data nicely and all fall within the range of error-bars for both front side and back side paths. The approach with constant heat transfer coefficient gave an unacceptable disagreement with the experimental results, while the scenario with variable heat transfer coefficient gave rather good agreement with measured data in the front heated wall. However, in the back non-heated wall the approach using correlations overestimated measured temperatures. Therefore, using approaches with heat transfer coefficient correlations for the evaluations of heat removal from the single-sided heated structure like first wall is not reliable enough. It is necessary to include the 3D CFD simulation to get the acceptable simulation results.

- Test case 2: Cooling double-sided heated structure

The above Test case 1 proves that the approach with variable heat transfer coefficient performs better than the approach with constant heat transfer coefficient but both of them failed to provide reliable results for the single-sided heated case with strong asymmetry of loading. The following Test case 2 was used to validate the approach with variable heat transfer coefficient for the double-sided heated cases.

Fig. 3.4 depicts the geometry: a horizontal stream of water which was simulated as turbulent flow that cools a horizontal tungsten plate. Symmetry boundary condition was applied on the top surface of the fluid domain due to the assumption of double-sided heating. Heat flux was applied on the bottom surface of the solid plate. This model is an analogy of coolant inside a tube with square cross section, which is widely used in cooling systems of high heat flux plasma-facing components.

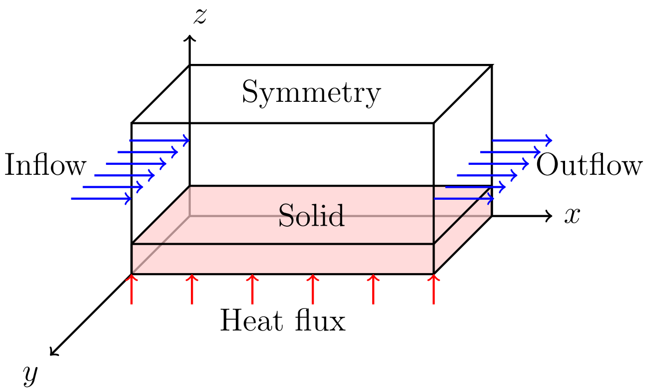

Figure 3.4: Simple model of forced turbulent convection cooling for validation

Two models were set up based on the two modeling methods discussed above. The first method, which includes the fluid domains, is what COMSOL built-in module uses for conjugate heat transfer problem thus has been validated. Thus we can trust the second method if its results match well with the first one. Detailed boundary conditions for both models are shown in Table 3.2. A parametric sweep on inlet velocity was performed to test the model performance at different velocities.

	U_{in} [m/s]	P_{out} [Pa]	T_{in} [K]	q_{in} [MW/m^2]	Solid-fluid interface
Method 1	1, 2, 5, 10	1.013×10^5	293	0.5	$q = \frac{\rho C_p C_\mu^{1/4} k_w^{1/2}(T_w - T)}{T^+}$
Method 2	NA	NA	NA	0.5	$h = \frac{Nu \cdot k}{D}$

Table 3.2: Boundary conditions for two turbulent forced convection models

The results can be verified in terms of heat transfer coefficient at the solid-fluid interface. Fig. 3.5 compares the local heat transfer coefficient from two models. The plot shows results from two models agree well with each other at every velocity level.

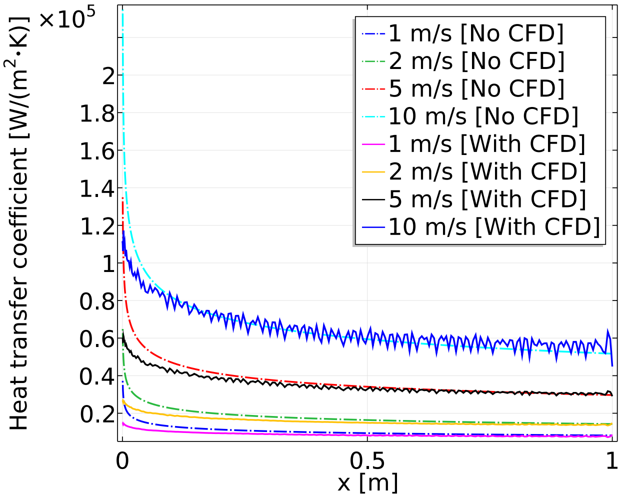

Figure 3.5: Heat transfer coefficient at solid-fluid interface

Results from Test case 1 and 2 can provide us the guidance of how to choose the appropriate model of forced convection problem under different scenarios. When the cooled structure is single-sided heated, then 3D CFD simulation must be included to give accurate temperature on both heated and non-heated side. If the heated structure is applied by a relatively uniform heating, then the simplified approach with variable heat transfer coefficient is reliable enough and is recommended to use due to its computational efficiency.

3.2 The Multiscale Approach to Design

Prior to early 1960s, most of the mechanical components were designed according to a systematic Design by Formula (DBF) approach. It's based on simple mechanics and standard basic configurations like cylindrical pressure vessels. Although it's easy to implement, it usually leads to conservative design that does not necessarily improve security. Besides, it's not able to handle non-standard configurations and complex loading conditions. The development of nuclear technology in the 1960s led to a reappraisal of design requirements to seek for a design code which is less conservative without reduction in safety. In the ASME Section III Design Code [36], Design-by-Analysis (DBA) approach was introduced, where elastic stress analysis is used to realize design constraints. DBA may be used as an alternative to DBF approach with higher allowable loads and consistent safety margins. The design codes are aiming at prevent failure mechanisms including plastic deformation and brittle fracture under static load, incremental plastic collapse under repeated load and fatigue under cyclic load. Finite element analysis is a powerful tool to provide accurate simulation results for DBA approach. However, most of the design codes are based on elastic analysis, providing limited guidelines for plastic analysis and inelastic failure mechanisms.

For fusion energy applications, structural design codes are still evolving. Presently, the code for Structural Design Criteria for In-Vessel Components (SDC-IC) [37] contains interim rules for the structural design of the in-vessel components: first wall (FW), shield/blanket (B), divertor and the diagnostic components located inside of vacuum vessel for ITER. The ITER design criteria make one step further from pure elastic analysis to so-called enhanced elastic analysis, meaning post-processing the FEM data to determine membrane, bending, thermal, and peak stress followed by a comparison to allowable stresses described in the design code. Although membrane, bending, thermal and peak stresses are computed elastically, the corresponding allowable stresses are derived from experimental tests, including the effects of complex variables, such as stress triaxiality and the available ductility of the material. In this giant step, elastic analysis is related to failure mechanisms that are the results of plastic deformation and fracture process. This process has been the basis of the ITER SDC-IC.

Alternatively, another enhanced elastic analysis approach which avoids performing expensive plasticity calculations by post-processing the data obtained from elastic analysis in a way to include the effects for plastic deformation on stress and strain redistributions. The approach was pioneered by Neuber within the context of fatigue design [38] for steady state analysis, and later by Bree for analyzing the effects of cyclic plastic deformation [39].

All these enhanced elastic analysis approaches are able to enhance the results by post-processing the data but still in an approximate way. Design code needs to be improved for inelastic analysis including large deformation and strain hardening effects. For this purpose, more sophisticated models like elasto-plastic and crystal plastic models need to be used. However, the large computational cost of these models impedes them from being widely used for real-life design and applications. By incorporating these computationally expensive models into the global-local multiscale framework discussed in Chapter 2, we can trade off between accuracy and computational demand.

Here in this section, we firstly present three methodologies for enhancements of the current design code through simplified plastic analysis — ITER SDC-IC criteria, Neuber method and Bree diagram approach that outlines necessary conditions for avoiding ratcheting and thermal fatigue failure mechanisms. Modified strength-based criteria are then presented, which would require minimal changes in current procedures. We finally present brief introduction of the elasto-plastic and crystal plastic models, which provide a potential path forward towards a more precise DBA approach.

3.2.1 Enhanced elastic analysis

- ITER SDC-IC criteria

Several design codes are used for qualification of high-temperature components in nuclear environments. For fusion energy applications, structural design rules are still evolving. Presently, the code for Structural Design Criteria for In-Vessel Components (SDC-IC) contains interim rules for the structural design of the in-vessel components: First wall/blanket (FW/B), divertor and the diagnostic components located inside of vacuum vessel for ITER.

To understand design criteria, we briefly discuss here the main definitions in the ITER design code:

1. *Primary stress:* primary stress is defined as that portion of the total stress which is required to satisfy equilibrium with the applied loading and which does not diminish after small scale permanent deformation.

2. *Secondary stress:* secondary stress is that portion of the total stress (minus peak

stresses, as defined below), which can be relaxed as a result of small scale permanent deformation. The basic characteristic of a secondary stress is that it is self-limiting.

3. *Total stress (strain):* total stress σ_{ij} (strain ε_{ij}) is the stress (strain) under the effect of all the loadings to which the component is subjected.

4. *Membrane stress (strain):* membrane stress (or strain) tensor is the tensor whose components $(\sigma_{ij})_m$ [$(\varepsilon_{ij})_m$] are equal to the mean value of stresses σ_{ij} (ε_{ij}) through the thickness.

5. Bending stress (strain): the bending stress (strain) tensor is that tensor whose components $(\sigma_{ij})_b$ [$(\varepsilon_{ij})_b$] vary linearly through the thickness and which, when integrated through the thickness result in equilibrium with the section moment.

6. *Peak stress:* Peak stress is the increment of stress which is additive to the membrane-plus-bending stresses by reason of local discontinuities or local thermal stresses including the effects, if any, of stress concentrations.

7. *Stress intensity:* the stress intensity, $\overline{\sigma}$, at any given point is a scalar derived from the stress tensor, $\boldsymbol{\sigma}$, at that point, using the maximum shear or Tresca criterion.

8. *Effective stress:* the effective stress used for creep calculation is based on von-Mises effective stress.

9. *Stress intensity range:* it is the maximum of the stress intensities of the tensor differences between the stress tensors $\sigma(t)$ and $\sigma(t)$ for every pair of times t and t' within a cycle.

10. *Allowable primary membrane stress intensity (S_m)*: S_m is a temperature (T) and fluence (Φt) dependent allowable stress intensity defined as the least of the quantities:

$$\begin{aligned} S_m = Min \Bigg[& \frac{1}{3} S_{u,min}(RT,0), \frac{1}{3} S_{u,min}(T,0), \\ & \frac{1}{3} S_{u,min}(T,\Phi t), \frac{2}{3} S_{y,min}(RT,0), \\ & \frac{2}{3} S_{y,min}(T,0), \frac{2}{3} S_{y,min}(T,\Phi t) \Bigg] \end{aligned} \tag{3.9}$$

where $S_{y,min}$ and $S_{u,min}$ are the minimum yield and ultimate tensile strengths, respectively, and RT is room temperature.

- Neuber method

Elasto-plastic analysis is necessary for preventing inelastic failure mechanisms. To avoid computationally expensive elasto-plastic analysis of a complex system, it is necessary to translate the elastic calculated stress at the critical locations into estimates of elastic-plastic stress and strain behavior. One of the most popularly used methods is the Neuber plasticity correction [38]. The advantage of this Neuber method is that equivalent plasticity information could be obtained without implementing plastic analysis. In this approach, a post-processing step is made to re-compute the stress and strain field via approximate energy conservation principles, whereby the uniaxial stress-strain curve is used to re-compute stresses in the plastic regime approximately, using available elastic information alone and a conservation of energy principle. In this fashion, elastic stresses (which tend to be overestimated at high loads) would be reduced, and the elastic strains increased to mimic the results of full-fledged plasticity.

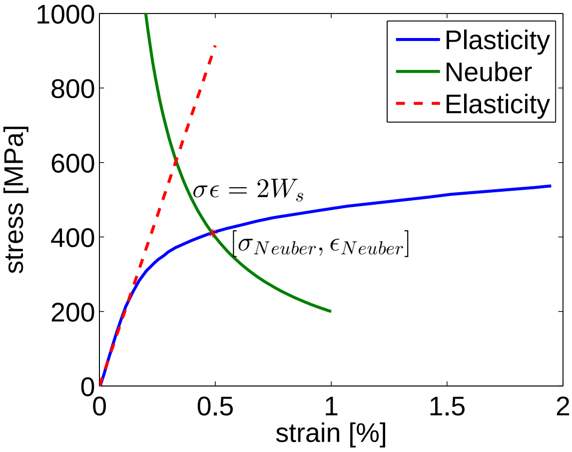

Figure 3.6: Stress-strain curve with Neuber Hyperbola

- Bree diagram

When the heat flux is fluctuating, the combination of thermal and mechanical (pressure) stress can lead to an elastic stress state, a cyclic plastic stress state, shakedown stress state or a ratchet stress state where the structure will continually grow in size and its thickness reduced gradually till rupture. The ASME design code limits on these failure phenomenon are due to the work of Bree [39]. The six different regimes based on the Bree analysis and used in the ASME Design Code are shown in Fig. 3.7.

As discussed in the SDC-IC criteria section, the stress can be divided into membrane and bending components that can include thermal stress gradients. This provides the basis for the approach of Bree. The membrane stress from an FEM calculation would be equivalent to the pressure (mechanical) stress in Bree analysis, and the bending stress can be equivalent to the thermal stress. The Bree diagram can be constructed to determine the expected regimes of ratcheting, elastic shakedown and cyclic plasticity, and to calculate the accumulated plastic strain from cycle-to-cycle in an approximate manner.

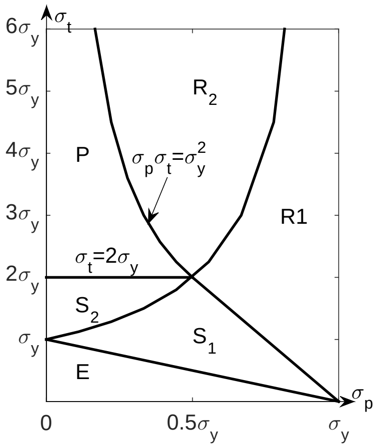

Figure 3.7: Design regimes for cyclic thermal plus pressure loading

3.2.2 Elasto-plastic analysis

There are two implementations of plasticity for small strains and large strains respectively. The one for small strains is based on the additive decomposition of strains while the other one for large strains is based on the multiplicative decomposition of the deformation gradient.

1) Small plastic strain

The stress-strain relationship is written as:

$$\boldsymbol{\sigma} = \boldsymbol{C} : (\boldsymbol{E} - \boldsymbol{E}^T - \boldsymbol{E}^P - \boldsymbol{E}^C) = \boldsymbol{C} : \boldsymbol{E}^E \tag{3.10}$$

where $\boldsymbol{E}^T$ is the thermal strain tensor, $\boldsymbol{E}^P$ is the plastic strain tensor and $\boldsymbol{E}^C$ is the creep strain tensor.

In the special case of no creep or thermal expansion, the elastic strain tensor simplifies to $\boldsymbol{E}^E = \boldsymbol{E} - \boldsymbol{E}^P$.

For the small plastic strain, the direction of the plastic strain increment is defined by:

$$\dot{\boldsymbol{E}}^P = \lambda \frac{\partial Q_p}{\partial \boldsymbol{\sigma}} \tag{3.11}$$

where λ is a positive multiplier (also called the plastic multiplier) which depends on the current state of stress and the load history, and Q_p is the plastic potential.The plastic multiplier λ is determined by the complementary or Kubn-Tucker conditions:

$$\lambda \geq 0,\ F_y \leq 0,\ \text{and } \lambda F_y = 0 \tag{3.12}$$

where F_y is the yield surface, which encloses the elastic region defined by $F_y < 0$. Plastic flow occurs when $F_y = 0$. If the plastic potential and the yield surface coincide with each other ($Q_p = F_y$), the flow rule is called associated.

For isotropic plasticity, the plastic potential Q_p is written in terms of at most three invariants[1] of Cauchy's stress tensor:

$$Q_p(\boldsymbol{\sigma}) = Q_p(I_1(\boldsymbol{\sigma}), J_2(\boldsymbol{\sigma}), J_3(\boldsymbol{\sigma})) \tag{3.13}$$

So the increment of the plastic strain tensor can be decomposed into[2]:

$$\dot{\boldsymbol{E}}^P = \lambda(\frac{\partial Q_p}{\partial I_1}\frac{\partial I_1}{\partial \boldsymbol{\sigma}} + \frac{\partial Q_p}{\partial J_2}\frac{\partial J_2}{\partial \boldsymbol{\sigma}} + \frac{\partial Q_p}{\partial J_3}\frac{\partial J_3}{\partial \boldsymbol{\sigma}}) \tag{3.14}$$

---

[1] $I_1 = \text{tr}(\sigma)$, $J_2 = \frac{1}{2}\text{dev}(\sigma) : \text{dev}(\sigma)$, $J_3(\sigma) = \det(\text{dev}(\sigma))$

[2] $\frac{\partial I_1}{\partial \boldsymbol{\sigma}} = \boldsymbol{I}$, $\frac{\partial J_2}{\partial \sigma} = \text{dev}(\sigma)$, $\frac{\partial J_3}{\partial \sigma} = \text{dev}(\sigma)\text{dev}(\sigma) - \frac{2}{3}J_2\boldsymbol{I}$

A common measure of inelastic deformation is the effective plastic strain rate, which is defined as:

$$\dot{\varepsilon}_{pe} = \sqrt{\frac{2}{3}\dot{\boldsymbol{E}}^P : \dot{\boldsymbol{E}}^P} \tag{3.15}$$

When associate flow rule is applied, the yield function must be smooth. A commonly used form is $F_y = \phi(\boldsymbol{\sigma}) - \sigma_y$. Where σ_y is the yield stress function and $\phi(\boldsymbol{\sigma})$ is the effective stress for which von Mises stress is commonly used.

For the yield function σ_y, if it is a constant, then the perfect plastic hardening is implied. But a more realistic hardening model is isotropic hardening, which means the yield stress function σ_y depends on the effective plastic strain ε_{pe}. An easy way to define the relationship between yield stress and the effective plastic strain is by using tangent data (linear isotropic hardening). In this case, an isotropic tangent modulus K is given, which is defined as $\frac{\partial \sigma}{\partial \varepsilon_{\text{tot}}}$. Then the yield stress function becomes:

$$\sigma_y(\varepsilon_{pe}) = \sigma_{y0} + \sigma_h(\varepsilon_{pe}) = \sigma_{y0} + \frac{KE}{E-K}\varepsilon_{pe} \tag{3.16}$$

Alternatively, an arbitrary hardening function data could be defined for the nonlinear hardening function $\sigma_h(\varepsilon_{pe})$.

2) Large plastic strain

If $\boldsymbol{E}$ or $\boldsymbol{E}^P$ are large, the additive decomposition might produce incorrect results. Thus the multiplicative decomposition is used instead, as discussed in Section 2.2.

3.2.3 Microstructure-based crystal plasticity analysis

Isotropic plasticity models result in nonlinear boundary value problems that can be solved by a return-mapping algorithm within the finite element method framework. However, isotropic plasticity is not able to describe heterogeneous plastic behavior. Even though it has been known since 1934 [40] that crystalline materials deform plastically by the slip of dislocations on discrete slip systems, isotropic plasticity material models were used in finite element simulations for a long time. The first crystal plasticity finite element (CPFE) simulations were performed by Pierce, Asaro, and Needleman in 1982 [41]. After that, different crystal plasticity models were proposed using continuum-based variational formulations for describing the elastic-plastic deformation of anisotropic heterogeneous crystalline matter. CPFE models are critical both for basic microstructure-based mechanical predictions and engineering design and performance simulations involving anisotropic media.

The plastic deformation can be described by crystallographic slip. When a single crystal is deformed under a tensile stress, it is observed that plastic deformation occurs by slip on well-defined parallel crystal planes. It can be observed experimentally as shown in Fig. 3.8. This can explain why the elastic-plastic deformation of crystalline materials depends on the direction of loading. The anisotropy of the elastic tensor and the orientation dependence of the activation of crystallographic deformation mechanisms imply that mechanical parameters of crystalline materials are tensor quantities.

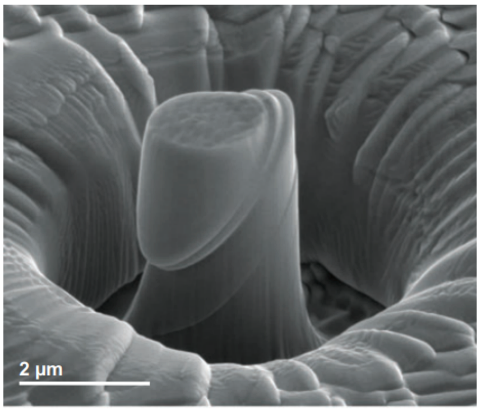

Figure 3.8: A deformed Cu micropillar after a compression[1]

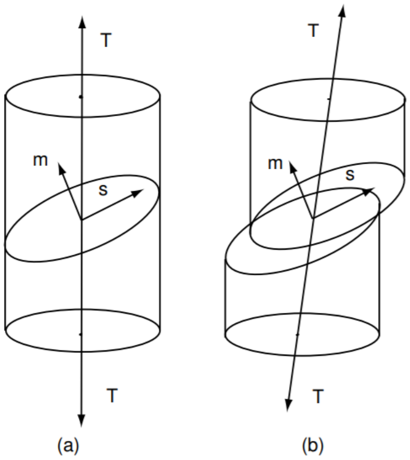

Figure 3.9: Schematic diagram for single slip in tension

A simple example is the uniaxial test, which is the most important mechanical measure in structural materials design, as shown in Fig. 3.9. The uniaxial stress-strain curve represents an incomplete description of plastic deformations since they reduce a six-dimensional yield surface and its change upon loading to a one-dimensional yield curve. CPFE models, which are based on the variational solution of the equilibrium of the forces and the compatibility of the displacements using a weak form of the principle of virtual work, provide the potential to solve this problem. The tensorial crystallographic nature of the underling defects that lead to shear can be guaranteed by the dyadic form of the velocity gradient (Eq. 4.2). This means that the CPFE method has evolved as an attempt to employ some of the extensive knowledge gained from experimental and theoretical studies of single-crystal deformation and dislocations to inform the further development of continuum mechanics. The general framework of CPFE provides an attractive vehicle for developing a comprehensive theory of plasticity that incorporates existing knowledge of the physics of deformation process into the computational tools of continuum mechanics with the aim of developing advanced and physically-based design methods for engineering applications.

It was demonstrated that the CPFE method is a powerful modeling tool for a wide range of mechanical problems in the field of materials science and engineering. It extends the capability from modeling macroscopic regime which conventional plasticity can handle to modeling mesoscopic and even microscopic regime. In addition, crystal plasticity models can be used in conjunction with commercial or academic finite element solvers in the form of user-defined materials subroutines, providing its potential in engineering and design applications. Detailed CPFE model formulations and implementations are discussed in Chapter 4.

CHAPTER 4

A Multiscale Crystal Plasticity Model

4.1 Review of Crystal Plasticity Models

In this chapter, the basic kinematics of crystal plasticity will be introduced, followed by a review of commonly used constitutive models. Those, in turn, can be classified into phenomenological and physics-based models.

4.1.1 Basic kinematics

Similar to what was introduced in the large-deformation elasto-plasticity framework, in crystal plasticity one has to distinguish between three coordinate systems. In a crystalline solid, an increment of deformation is imagined to occur in two steps. Starting from a reference state, deformation occurs by a process of simple shears on slip systems caused by dislocations, followed by a process of lattice deformation. The basic kinematic scheme is shown in Fig. 4.1.

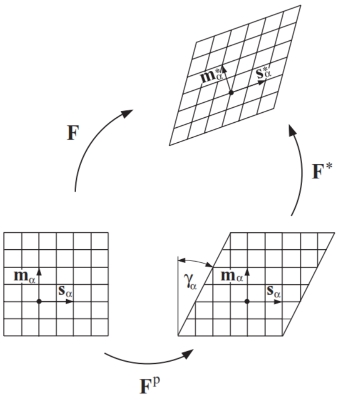

Figure 4.1: Kinematic model of elastoplastic deformation of a single crystal

The multiplicative decomposition of the deformation gradient $\boldsymbol{F} = \boldsymbol{F}^E \cdot \boldsymbol{F}^P$ discussed in the preceding section also holds in crystal plasticity.

Firstly, the material flows through the crystalline lattice by crystallographic slip, which gives rise to deformation gradient $\boldsymbol{F}^P$. During this step, the lattice coordinate system has coordinate axes fixed locally parallel to the crystallographic directions. Thus $\boldsymbol{F}^P$ represents isochoric plastic deformation ($\det(\boldsymbol{F}^P) = 1$), where crystal lattice is neither distorted nor rotated. Then the material with embedded lattice is deformed elastically from the intermediate to the current frame, resulting in internal stresses since these stresses arise from internal reaction forces generated when atoms experience a relative displacement from their equilibrium positions, which can only be related to lattice deformations. Due to lattice rotations, vectors in the intermediate and current configuration are related by $s_i = F^E_{i\alpha} s_\alpha$ and $n_i = n_\alpha F^{E^{-1}}_{\alpha i}$.

Evolution of the deformation requires the expression of the time derivative of $\boldsymbol{F}$. The spatial gradient of the velocity is defined as:

$$\boldsymbol{L} = \nabla_{\boldsymbol{x}} \boldsymbol{v} = \nabla_{\boldsymbol{x}} \dot{\boldsymbol{x}} = \nabla_{\boldsymbol{X}} \dot{\boldsymbol{x}} \cdot \boldsymbol{F}^{-1} = \dot{\boldsymbol{F}} \cdot \boldsymbol{F}^{-1} \tag{4.1}$$

where $\nabla_{\boldsymbol{x}}$ and $\nabla_{\boldsymbol{X}}$ refers to the spatial gradient evaluated in current and reference configuration respectively. Similarly, elastic and plastic velocity gradient $\boldsymbol{L}^E$ and $\boldsymbol{L}^P$ can be expressed by $\boldsymbol{F}^E$ and $\boldsymbol{F}^P$ respectively. Using the kinematics of dislocation glide, the rate of evolution of $\boldsymbol{F}^P$ could be expressed in terms of shear slip rate $\dot{\gamma}^\alpha$ on each slip system as [42]:

$$\dot{\boldsymbol{L}}^P = \dot{\boldsymbol{F}}^P \boldsymbol{F}^{P^{-1}} = \sum_{\alpha=1}^{n_{\text{slip}}} \dot{\gamma}^\alpha \boldsymbol{s}^\alpha \otimes \boldsymbol{n}^\alpha \tag{4.2}$$

in which $\boldsymbol{L}^P$ is the plastic velocity gradient in the intermediate configuration, n_{slip} corresponds to number of slip systems and $\boldsymbol{s}^\alpha$ and $\boldsymbol{n}^\alpha$ are respectively slip direction and slip plane normal for slip system α in the reference configuration.

By combining Eq. 2.23 and Eq. 4.1, the relation of $\boldsymbol{L}$ to $\boldsymbol{L}^E$ and $\boldsymbol{L}^P$ can be expressed as:

$$\boldsymbol{L} = (\dot{\boldsymbol{F}}^E \boldsymbol{F}^P + \boldsymbol{F}^E \dot{\boldsymbol{F}}^p) \cdot (\boldsymbol{F}^{P^{-1}} \boldsymbol{F}^{E^{-1}}) = \boldsymbol{L}^E + \boldsymbol{F}^E \boldsymbol{L}^P \boldsymbol{F}^{E^{-1}} \tag{4.3}$$

Eq. 4.3 shows that the total velocity gradient $\boldsymbol{L}$ can be additively decomposed into an elastic part and a plastic part mapped from intermediate configuration to current configuration by $\boldsymbol{F}^E$.

There is a fundamental quantity connecting the individual dislocations at the micro-scale to the macroscopic plastic deformation gradient fields named dislocation density tensor (or Nye's dislocation tensor) introduced by Nye [43]. The dislocation density tensor $\boldsymbol{\alpha}$ is defined by its relationship with Burgers vector $\tilde{\boldsymbol{b}}$ measured in the intermediate configuration for orientated area $\boldsymbol{A}$ in the reference configuration.

$$\tilde{\boldsymbol{b}} = \int_{\tilde{C}} d\tilde{\boldsymbol{x}} = \oint_{C_0} \boldsymbol{F}^P d\boldsymbol{X} = \int_{S_0} \nabla_{\boldsymbol{X}} \times \boldsymbol{F}^P d\boldsymbol{A} = \int_{\tilde{S}} \frac{1}{J^P} \nabla_{\boldsymbol{X}} \times \boldsymbol{F}^P \cdot (\boldsymbol{F}^P)^T d\tilde{\boldsymbol{A}} \tag{4.4}$$

where C_0 and S_0 are a random closed path and its closure area in the reference frame, while $\tilde{C}$ and $\tilde{S}$ are the ones measured in the intermediate frame. Note that due to the incompatibility of mapping $\boldsymbol{F}^P$, $\tilde{C}$ is not a closed contour. The loop closure failure of $\tilde{C}$ can be measured by the total burgers vector $\tilde{\boldsymbol{b}}$ for area $\boldsymbol{A}$.

As denoted in Eq. 4.4, the dislocation density tensor can be defined as the left curl of the plastic deformation gradient:

$$\boldsymbol{\alpha} = \nabla_{\boldsymbol{X}} \times \boldsymbol{F}^P \tag{4.5}$$

The kinematic formulas describe the geometrical aspects of the anisotropy of materials without considering stresses. To capture the physics of the material behaviors, the constitutive models need to be built and slip rate $\dot{\gamma}^\alpha$ needs to be determined. In the following sections, two classes of constitutive models, phenomenological models and physics-based models are reviewed.

4.1.2 Phenomenological Constitutive Models

Phenomenological constitutive models usually use a critical resolved shear stress τ_c^α as state variable for each slip system α. The slip system is activated and the slip begins when resolved shear stress $\tau_{\mathrm{rss}}^\alpha$ reaches τ_c^α. The resolved shear stress on α slip system may be defined as $\tau^{\alpha}_{rss} = \boldsymbol{S} : \boldsymbol{R}^{\alpha}$, where $\boldsymbol{S}$ is the stress tensor and $\boldsymbol{R}^{\alpha}$ is the Schmid tensor defined as $\boldsymbol{R}^{\alpha} = \frac{1}{2}(\boldsymbol{s}^{\alpha} \otimes \boldsymbol{n}^{\alpha} + \boldsymbol{n}^{\alpha} \otimes \boldsymbol{s}^{\alpha})$.

Thus the plastic shear rate $\dot{\gamma}^{\alpha}$ is formulated as a function of the resolved shear stress and critical resolved shear stress:

$$\dot{\gamma}^{\alpha} = f(\tau^{\alpha}_{\text{rss}},\ \tau^{\alpha}_{\text{crss}}) \tag{4.6}$$

and the evolution of the material state is formulated as function of the total shear γ and the slip shear rate $\dot{\gamma}^{\alpha}$:

$$\tau^{\alpha}_{\text{crss}} = g(\gamma,\ \dot{\gamma}^{\alpha}) \tag{4.7}$$

One commonly used group of formulations that follow Eq. 4.6 and Eq. 4.7 is the one where the plastic slip rate has a power law dependence on resolved shear stress $\tau^{\alpha}_{\text{rss}}$ in each particular slip system, suggested by Rice [44] and Peirce *et al.* [41]:

$$\dot{\gamma}^{\alpha} = \dot{\gamma}_0 (\frac{\tau^{\alpha}_{\text{rss}}}{\tau^{\alpha}_{\text{crss}}})^{\frac{1}{m}} \cdot \text{sign}(\tau^{\alpha}_{\text{rss}}) \tag{4.8}$$

where $\dot{\gamma}_0$ and m are material-dependent fitting parameters, which are the reference shear rate and rate sensitivity of slip respectively.

As discussed above, slip initiates on system α when $\tau^{\alpha}_{\text{rss}}$ reaches the $\tau^{\alpha}_{\text{crss}}$, which is taken initially identical for all slip systems. After slip initiates, $\tau^{\alpha}_{\text{crss}}$ evolves depending on slip rates on other slip systems. The hardening increses with on-going shear strain. The hardening behavior of a slip system α by the influence of any other slip systems β is expressed as:

$$\dot{\tau}^{\alpha}_{\text{crss}} = \sum_{\beta=1}^{n} h_{\alpha\beta} |\dot{\gamma}^{\beta}| \tag{4.9}$$

where $h_{\alpha\beta}$ is name as hardening matrix:

$$h_{\alpha\beta} = q_{\alpha\beta} \left[h_0 \left(1 - \frac{\tau^{\beta}_{\text{crss}}}{\tau_s} \right)^{a} \right] \tag{4.10}$$

where h_0, a, and τ_s are slip hardening fitting parameters and assumed to be equal for all slip systems. $q_{\alpha\beta}$ is taken as 1 if slip system α and β are coplanar and 1.4 for other cases. Eq. 4.9 and Eq. 4.10 empirically incorporate the microstructural interaction between different slip systems.

There are lots of variations of Eq. 4.8 and Eq. 4.9 in the literature. Some authors used modified hardening laws [45] and some others used sinh function [46] instead of the power law in Eq. 4.8.

One of the critical drawbacks of these phenomenological models is that the material state is only described in terms of the critical resolved stress but there is no link to the defects or dislocations, which are more fundamental physically. To solve this problem, physics-based models are proposed, as presented in next section.

4.1.3 Physics-based Constitutive Models

In contrast to the phenomenological constitutive models, the physics-based ones depend on microstructure-related internal variables, such as the dislocation density. There are mainly two tasks for physics-based constitutive models: (1) Calculation of the flow stress from dislocation densities. (2) Computation of the evolution of dislocation densities. Following this logic, different models have been proposed by various researchers (e.g. references [47, 48]).

In a typical dislocation-based crystal plasticity model, the Orowan equation [49] is used for kinetic equation instead of Eq. 4.8 in phenomenological models. It links shear rates to mobile dislocation densities, capturing the physics of dislocations for a continuum mechanical term:

$$\dot{\gamma}^{\alpha} = \rho_m^{\alpha} b v^{\alpha} \tag{4.11}$$

where ρ_m^{α} is the density fo mobile dislocation densities, b is the magnitude of Burgers vector and v^{α} is the averaged velocity of mobile dislocations.

In addition, the phenomenological description of hardening in Eq. 4.9 is replaced by the expression depends on the dislocation densities in physics-based models. The Taylor equation [40] is one of the first expressions relating the flow stress to dislocation densities.

The maximum shear stress associated with a dislocation is proportional to $\mu b/r$, where μ is the shear modulus and r the distance to the dislocation, and the average spacing between randomly distributed dislocations is of order $1/\sqrt{\rho}$. Assuming the flow stress is the stress required to drive one dislocation past the other one which is on a parallel slip plane, the critical resolved shear stress can be expressed as:

$$\tau_{\text{crss}}^{\alpha} = \tau_0^{\alpha} + \beta b \mu \sqrt{\rho^{\alpha}} \tag{4.12}$$

where τ_0 is the intrinsic lattice resistance, equals to the Peierls stress for a screw dislocation at zero temperature and is the same for all slip systems, and β is a dimensionless parameter that can be fitted based on experimental data for different materials.

Additional microstructure-dependent components can be added to flow stress expression to capture other hardening effects. For example, if polycrystal is considered, a term τ_{GB} which accounts for the grain boundary hardening can be added. Hall-Petch relation gives the formulation of $\tau_{\text{GB}}^{\alpha}$ [50]:

$$\tau_{\text{GB}}^{\alpha} = \frac{k_{\text{HP}}}{\sqrt{d}} \tag{4.13}$$

where k_{HP} is the Hall-petch strengthening coefficient and d is the average grain size.

After expressing shear rate $\dot{\gamma}^{\alpha}$ and flow stress $\tau_{\text{crss}}^{\alpha}$ in terms of evolution of dislocation densities, the next task is to compute the evolution of dislocation densities. Following the law proposed by Mecking and Kocks [51], the evolution of dislocation density in each slip system is given as:

$$\dot{\rho}^{\alpha} = \dot{\gamma}^{\alpha}(k_1\sqrt{\rho^{\alpha}} - k_2\rho^{\alpha}) \tag{4.14}$$

where k_1 and k_2 are two Mecking-Kocks coefficients, the relationship between which was proposed by Beyerlein and Tome [52] as:

$$\frac{k_2}{k_1} = \frac{\chi b}{g}\left(1 - \frac{k_B T}{D b^3}\ln(\frac{\dot{\epsilon}}{\dot{\epsilon}_0})\right) \tag{4.15}$$

where χ, g, D and $\dot{\epsilon}_0$ are fitting parameters, $\dot{\epsilon}$ is the applied strain rate and k_B is the Boltzmann constant.

As Eq. 4.7 and Eq. 4.13 show, the flow stress is generally indicated by the dislocation density with contributions from the grain size (the Hall-Petch effect) in low-temperature crystal plasticity models. However, at high temperatures, grain growth takes place, and individual grains subjected to an applied stress start to subdivide themselves into subgrains of a size that is inversely proportional to the applied stress [53]. To capture the nucleation and growth of such subgrains when modeling at high temperatures, Ghoniem *et al.* [54] proposed the Ghoniem-Matthews-Amodeo's (GMA) model. The overall model is composed of three evolution equations for dislocation densities and one rate equation for average size of subgrain. They are given by:

$$\frac{d\rho_m^\alpha}{dt} = v_g^\alpha \left((\rho_m^\alpha)^{3/2} + \beta R_{sb}\rho_s^\alpha/h^2 - \rho_m^\alpha/(2R_{sb}) - \delta\rho_m^\alpha(\rho_m^\alpha + \rho_s^\alpha)\right) - 8(\rho_m^\alpha)^{3/2}v_{cm} \tag{4.16}$$

$$\frac{d\rho_s^\alpha}{dt} = v_g^\alpha\rho_m^\alpha/(2R_{sb}) - 8\rho_s^\alpha v_{cs}/h - \delta v_g^\alpha\rho_m^\alpha\rho_s^\alpha \tag{4.17}$$

$$\frac{d\rho_b^\alpha}{dt} = 8(1-2\zeta)\rho_s^\alpha v_c/h - \rho_b^\alpha M_{sb}(p_s - 2\pi r_p^2 N_p\gamma_{sb})/R_{sb} \tag{4.18}$$

$$\frac{dR_{sb}}{dt} = M_{sb}(p_s - 2\pi r_p^2 N_p\gamma_0 sb) - \mu\eta_v K_c R_{sb}[(\rho_m^{1/2} + \rho_s^{1/2}) - \frac{K_c}{2R_{sb}}]\frac{\Omega D_s}{kT} \tag{4.19}$$

where ρ_m, ρ_s, ρ_b and R_{sb} are mobile, static and boundary dislocation density and subgrain radius, respectively.

Eq. 4.16 - 4.18 are conservation equations that balance production and annihilation rates. For ρ_m^α, the first and second terms are the production rates from the mobile population and sub-grain walls, respectively, the third is for annihilation at sub-grain walls, the fourth is for climb recovery, and the last is for dynamic recovery. For ρ_s^α, the first term is for immobilization at sub-grain walls, the second is for climb recovery, and the last is for dynamic recovery. For ρ_b^α, the first term is the production rate from static dislocations incoming into the boundary, the second is for annihilation of boundary dislocations by the creation of new sub-grain surface. Finally, the rate equation for the sub-grain radius (Eq. 4.19) is a balance between the growth rate by reduction of surface area, and the second term is the rate of annihilation by creation of new sub-grain surface.

To demonstrate the feasibility of the GMA model discussed above, a simplified polycrystal model is presented here as an example. A five-grain tungsten polycrystal disc of diameter

0.6 mm and height of 0.16 mm, is subjected to a tensile strain rate of 0.02 s^{-1}. The top surface was allowed to move only in the z-direction, while the bottom surface was constrained to move only in x and y directions. For simplicity, only one slip system in each grain was considered, as shown in Fig. 4.2. Detailed slip directions and slip plane normals are listed in Table 4.1.

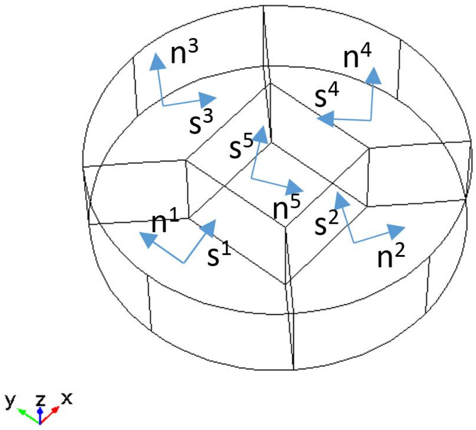

Figure 4.2: 5-grain polycrystal model.

Slip system No.	Slip directions	Slip plane
1	$[1,0,1]$	$(\bar{1},0,1)$
2	$[0,1,1]$	$(0,\bar{1},1)$
3	$[0,\bar{1},1]$	$(0,1,1)$
4	$[\bar{1},0,1]$	$(1,0,1)$
5	$[1,1,1]$	$(0,\bar{1},1)$

Table 4.1: Slip system orientations.

Fitting parameters in GMA model obtained in Table 4.2 were utilized for simulation. A temperature of 1600 °C was assumed. All the equations including ODEs in GMA model and crystal plasticity framework as well as weak form PDE were solved.

Parameter	Value	Unit	Description
β	1×10^4	-	Source density parameter
a_1	170	$m \cdot s^{-1}$	Phonon drag parameter
ζ	0.2	-	Static-to-boundary fraction
D_0	1×10^{-11} [55]	$m^2 \cdot s^{-1}$	Diffusion pre-exponential
E_{self}	5.95 [55]	eV	Self diffusion energy
Q	18.2 [56]	Ω	Activation Volume
ΔG_g	3.18	eV	Glide activation energy

Table 4.2: Fitting parameters used in the viscoplasticity model for W.

The stress in z-direction on the deformed structure is shown in Fig. 4.3. Stress concentrations can be observed near the boundary interfaces of different grains. This observation matches well with the anticipation based on the assigned slip systems. The stress-strain curves are plotted at one representative point inside each grain, as shown in Fig. 4.4.

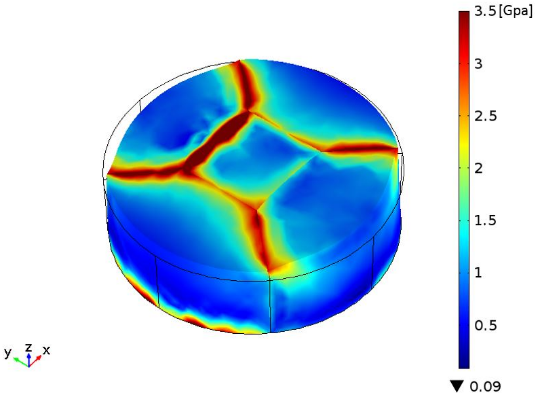

Figure 4.3: Stress distributions.

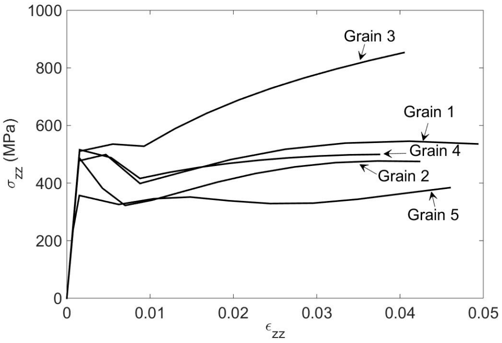

Figure 4.4: Stress-strain curves.

The physics-based models reviewed above capture the effects of dislocations on the plastic deformation. However, several equations and parameters are still phenomenological and strongly dependent on experimental data. A more fundamental crystal plasticity model which minimizes the number of fitting parameters will be introduced in the next chapter.

4.2 A Proposed Dislocation-Based Crystal Plasticity Model

Both commonly-used phenomenological and physics-based constitutive models of crystal plasticity have been reviewed in Sec. 4.1. Although the physics-based constitutive models capture the role of dislocations in plastic deformation, most of them still contain many phenomenological equations with fitting parameters. In this section, we propose an advanced dislocation-based crystal plasticity model, with model verification based on a wedge microindentation test case.

4.2.1 Model Formulation

The model is based on the conventional crystal plasticity framework, which includes a spatially dependent ODE governing the time evolution of $\boldsymbol{F}^P$: $\dot{\boldsymbol{F}}^P = \boldsymbol{L}^P\boldsymbol{F}^P$, as Eq. 4.2 shows, which requires the knowledge of $\boldsymbol{L}^P$. The idea of finding $\boldsymbol{L}^P$ is to compare the rates of dislocation density tensor computed from kinematic definition Eq. 4.5 and actual dislocation content respectively [57].

A fundamental aspect of the multiplicative decomposition $\boldsymbol{F} = \boldsymbol{F}^E\boldsymbol{F}^P$ is that $\boldsymbol{F}^E$ and $\boldsymbol{F}^P$ are individually incompatible, although the total deformation gradient $\boldsymbol{F}$ is compatible. Based on this fact, a closed oriented material curve $\mathcal{C}_0$ maps into a closed material curve $\mathcal{C}_t$ in the spatial configuration, while it transforms into an open curve $\tilde{\mathcal{C}}$ in the intermediate configuration. Thus the vector measuring the closure failure of $\tilde{\mathcal{C}}$ is

$$\tilde{B}_\gamma = \int_{\tilde{\mathcal{C}}} d\tilde{X}_\gamma \tag{4.20}$$

where d$\tilde{X}$ is an infinitesimal material vector in the intermediate configuration. This vector can be mapped to either the reference or the current configuration.

$$\tilde{B}_\gamma = \int_{\tilde{\mathcal{C}}} d\tilde{X}_\gamma = \oint_{\mathcal{C}_0} F^P_{\gamma I} dX_I = -\int_{\mathcal{S}_0} \epsilon_{JKM} F^P_{\gamma K,M} dA_J = -\int_{\tilde{\mathcal{S}}} \frac{1}{J^P} \epsilon_{JKM} F^P_{\gamma K,M} F^P_{\chi J} d\tilde{A}_\chi \tag{4.21}$$

Introduce the dislocation density tensor which measures the local closure failure

$$A_{\gamma J} = -\epsilon_{JKM} F^P_{\gamma K,M} \tag{4.22}$$

Eq. 4.22 is the kinematic definition of dislocation density tensor. Alternatively, letting the superscript r identify families of dislocations sharing a common Burgers vector $\tilde{\boldsymbol{b}}^r$ and line direction $\boldsymbol{\xi}^r$ and having density ϱ^r per unit reference area normal to their line direction, the dislocation density tensor can be expressed as

$$A_{\gamma J} = \sum_r A^r_{\gamma J} = \sum_r \varrho^r \, \tilde{b}^r_\gamma \xi^r_J \tag{4.23}$$

An expression for $\boldsymbol{L}^P$ is now obtained considering the rate of $\boldsymbol{A}$. The balance law governing the evolution of each $A^r_{\gamma J}$ leads to

$$\dot{A}^r_{\gamma J} = -\epsilon_{JKM} \left(L^r_{\gamma\chi} F^P_{\chi K} \right)_{,M} + p\tilde{b}^r_\gamma \xi_J \tag{4.24}$$

where $L^r_{\gamma\chi} = \tilde{\varrho}^r \tilde{b}^r_\gamma \epsilon_{\delta\beta\chi} \tilde{w}^r_\delta \tilde{\xi}^r_\beta$ is the Burgers vector flux of the r-th family, with $\tilde{\varrho}^r$, $\tilde{\boldsymbol{w}}^r$, $\tilde{\boldsymbol{\xi}}^r$ being the density, the velocity and line direction in the intermediate configuration, respectively.

On the other hand, the rate of the dislocation density tensor can be obtained by differentiating its kinematic definition Eq. 4.22.

$$\dot{A}_{\gamma J} = -\epsilon_{JKM} \left(\dot{F}^P_{\gamma K} \right)_{,M} = -\epsilon_{JKM} \left(L^P_{\gamma\chi} F^P_{\chi K} \right)_{,M} \tag{4.25}$$

Two important results are obtained by summing Eq. 4.24 over all slip systems and comparing with Eq. 4.25. First, that $\boldsymbol{L}^P$ can be expressed as the sum of the individual dislocation flux tensors

$$L^P_{\gamma\chi} = \sum_s L^{Ps}_{\gamma\chi} = \sum_s \tilde{b}^s_\gamma \epsilon_{\chi\beta\mu} \tilde{\varrho} \tilde{\omega}^s_\beta \tilde{\xi}^s_\mu \tag{4.26}$$

and second that the sum of the production terms must vanish

$$\sum_s \tilde{p}^s \tilde{b}^s_\gamma \tilde{\xi}^s_\chi = 0 \tag{4.27}$$

We further assume that only dislocation glide motion is allowed. Therefore the dislocation velocity of family s can be written as $\tilde{\boldsymbol{w}}^s = \tilde{w} \tilde{\boldsymbol{s}}^s$, where w^s is a scalar dislocation velocity field, and $\tilde{\boldsymbol{s}}^s$ is the fixed slip direction. In turn, the product $\tilde{n}^s_\delta = \epsilon_{\delta\chi\mu} \tilde{s}^s_\chi \tilde{\xi}^s_\mu$ defines the component of the glide plane normal for each slip system, and the plastic velocity gradient reduces to the familiar form encountered in CP theories [58]

$$L^P_{\gamma\delta} = \sum_r \dot{\gamma}^r \tilde{s}^r_\gamma \tilde{n}^r_\delta \tag{4.28}$$

where the slip rates are given by Orowan's equation $\dot{\gamma}^s = \tilde{\varrho}^s \tilde{b} \tilde{w}^s$.

The evolution of dislocation density ϱ^s follows the transport equation[1]:

$$\dot{\varrho}^s = -(\jmath_K)_{,K} + P^s = -(\tilde{w}^s \varrho^s \tilde{s}^s_\chi G^P_{K\chi})_{,K} + P^s \tag{4.29}$$

The next task is to determine the dislocation fluxes based on thermodynamic considerations. The following logic is used to achieve this goal. In classical continuum mechanics,

---

[1] $J_K dA_K = J_\chi dA_\chi = J_\chi J^P G^P_{K\chi} dA_K \to J_K = J^P G^P_{K\chi} J_\chi$

the dissipation equation is often employed to derive thermodynamic restrictions imposed on constitutive laws and here we specialize it for dislocation plasticity. The first law of thermodynamics states that the rate of the internal energy plus that of kinetic energy of a thermodynamic system is equal to the rate of external mechanical work plus the rate of heat supply to the system due to heat flux and heat source. Besides, the effect of dislocations to the system should also be considered. Assume the flux of dislocations of family s is J_k^s and the production rate of dislocation of family s is p^s. φ^s represents the energy per unit dislocation length. Then the energy balance based on the first law of thermodynamics turns out to be[2]:

$$\begin{aligned}\frac{d}{dt}\int_{\mathcal{B}_0}\left(\frac{1}{2}v_iv_i+\phi\right)\rho_0 dV = &\oint_{\partial\mathcal{B}_0}\left(P_{iK}v_i - Q_K - \sum_s \varphi^s \jmath_K^s\right)dA_K \\ &+\int_{\mathcal{B}_0}\left(b_kv_k + h + \sum_s \varphi^s p^s/\rho_0\right)\rho_0 dV \qquad (4.30)\end{aligned}$$

The second law of thermodynamics states that the rate of increase in the entropy of a system is never less than the rate of increase in the entropy due to heat source and heat flux. Again, the entropy of dislocations needs to be included in the balance. Assume χ^s represents the entropy per unit dislocation length in J/(K·m). The final entropy balance of the system follows[3]:

$$\frac{d}{dt}\int_{\mathcal{B}_0}\eta\,\rho_0 dV = \oint_{\partial\mathcal{B}_0}\left(-\frac{Q_K}{T} - \sum_s \chi^s \jmath_K^s\right)dA_K + \int_{\mathcal{B}_0}\left(\frac{h}{T} + \sum_s \chi^s p^s/\rho_0 + \gamma\right)\rho_0 dV \quad (4.31)$$

By combining the local forms of energy and entropy balance equations, together with the condition of conservation of mass $\dot{\rho}_0 = 0$ and linear momentum ($\rho_0\dot{v}_i = P_{Ki,K} + \rho_0 b_i$) we obtain:

$$\rho_0(\dot{\phi} - T\dot{\eta}) = P_{iK}v_{i,K} - (\varphi^s J_K^s)_{,K} + \varphi^s p^s - \frac{Q_K}{T}T_{,K} + (T\chi^s J_K^s)_{,K} - \chi^s J_K^s T_{,K} - \chi^s p^s T - \gamma\rho_0 T \qquad (4.32)$$

---

[2] v_i is the velocity of system, ϕ is the system internal energy per unit mass. With Piola transformation, $P_{iK} = JG_{Kk}\sigma_{ik}$, $Q_k = JG_{Kk}q_k$, where q_k is the heat flux, $J_K = JG_{Kk}J_k$, b_k is the body force in [N/kg], h is the heat source in [W/kg]

[3] γ is a positive quantity, aiming to show that the left hand side of the equation is not less than the expression of right hand side without γ

We further manipulate Eq. 4.32 introducing the Helmholtz free energy $\psi = \phi - T\eta$, the chemical potential $\mu^s = \varphi^s - T\chi^s$, the balance law for each dislocation density (4.29), and assuming isothermal deformation:

$$P_{iK}\dot{F}_{iK} - \rho_0\dot{\psi} - \rho_0\eta\dot{T} + \sum_s(\mu^s\dot{\varrho}^s - \mu^s_{,K}\jmath^s_K) = T\rho_0\gamma \geq 0 \tag{4.33}$$

Further manipulation of the dissipation Eq. 4.33 requires a constitutive law between the free energy density and appropriate kinematic variables. However, as pointed out by [?], in order to explicitly guarantee the independence of the free energy on the preceding plastic deformation, the constitutive law must be given for the free energy per *intermediate* unit volume $\tilde{W} = \tilde{\rho}\psi = \frac{\rho_0}{J^P}\psi$. Plug $\rho_0\dot{\psi} = J^P\dot{\tilde{W}} + \dot{J}^P\tilde{W} = J^P\dot{\tilde{W}} + J^P\tilde{L}^p_{\chi\chi}\tilde{W} = J^P\dot{\tilde{W}}$ into Eq. 4.33 gives:

$$P_{iK}\dot{F}_{iK} - J^P\dot{\tilde{W}} - \rho_0\eta\dot{T} + \sum_s(\mu^s\dot{\varrho}^s - \mu^s_{,K}\jmath^s_K) = \rho_0 T\gamma \geq 0 \tag{4.34}$$

To derive the inelastic constitutive equations by the thermodynamic theory, we assume that the free energy is a function of the elastic Green-Lagrangian strain, temperature, and each of the dislocation densities ϱ^s, that is

$$\tilde{W} = \tilde{W}(\boldsymbol{E}^E, T, \varrho^s) \tag{4.35}$$

Based on the assumption as Eq. 4.35 shows, $\dot{\tilde{W}}$ can be calculated as:

$$\dot{\tilde{W}} = \frac{\partial\tilde{W}}{\partial E^E_{\alpha\beta}}\dot{E}^E_{\alpha\beta} + \frac{\partial\tilde{W}}{\partial T}\dot{T} + \sum_s\frac{\partial\tilde{W}}{\partial\varrho^s}\dot{\varrho}^s = \frac{\partial\tilde{W}}{\partial E^E_{\alpha\beta}}F^E_{i\beta}\dot{F}^E_{i\alpha} + \frac{\partial\tilde{W}}{\partial T}\dot{T} + \sum_s\frac{\partial\tilde{W}}{\partial\varrho^s}\dot{\varrho}^s \tag{4.36}$$

Substituting Eq. 4.36 into Eq. 4.34 and drop the term with temperature gradient for an isothermal deformation process we obtain:

$$\begin{aligned}\left(\frac{1}{J^P}P_{iK}F^P_{\alpha K} - \frac{\partial\tilde{W}}{\partial E^E_{\alpha\beta}}F^E_{i\beta}\right)\dot{F}^E_{i\alpha} - \left(\frac{\partial\tilde{W}}{\partial T} + \tilde{\rho}\eta\right)\dot{T} + \sum_s\left(\frac{1}{J^P}\mu^s - \frac{\partial\tilde{W}}{\partial\varrho^s}\right)\dot{\varrho}^s \\ +\frac{1}{J^P}P_{iK}F^E_{i\alpha}\dot{F}^P_{\alpha K} - \sum_s\frac{1}{J^P}\mu^s_{,K}\jmath^s_K = T\tilde{\rho}\gamma \geq 0\end{aligned} \tag{4.37}$$

The terms in parenthesis in Eq. 4.37 are those that must vanish identically when the dissipation γ is assumed to be independent of the rate $\dot{\boldsymbol{F}}^E$, $\dot{T}$, and $\dot{\varrho}^s$. This assumption leads to the following constitutive relations[4]:

$$P_{mI} = J^P F^E_{m\alpha} \frac{\partial \tilde{W}}{\partial E^E_{\alpha\beta}} G^P_{I\beta} = J^P \left. \frac{\partial \tilde{W}}{\partial F_{mI}} \right|_{\boldsymbol{F}^P} = F_{mI} S_{IJ} \qquad \tilde{\rho}\eta = -\frac{\partial \tilde{W}}{\partial T} \qquad \mu^s = J^P \frac{\partial \tilde{W}}{\partial \varrho^s} \tag{4.38}$$

$$S_{IJ} = J^P \left. \frac{\partial \tilde{W}}{\partial E_{IJ}} \right|_{\boldsymbol{F}^P} = J^P G^P_{I\alpha} \frac{\partial \tilde{W}}{\partial E^E_{\alpha\beta}} G^P_{J\beta} \tag{4.39}$$

By virtue of these relations, and introducing the Mandel stress[5], the dissipation equation (4.37) is reduced to :

$$\tilde{M}_{\alpha\gamma} \tilde{L}^P_{\gamma\alpha} - \sum_s \frac{1}{J^P} \mu^s_{,K} \jmath^s_K = \tilde{\rho} T \gamma \geq 0 \tag{4.40}$$

Expanding $\boldsymbol{L}^P$ and $\jmath^s$ in terms of individual family velocity[6]:

$$\tilde{M}_{\alpha\gamma} \sum_s \tilde{\varrho}^s b \tilde{w}^s s^s_\gamma n^s_\alpha - G^P_{K\chi} \sum_s \mu^s_{,K} \tilde{\varrho}^s s^s_\chi \tilde{w}^s = \frac{1}{2} \sum_s B \tilde{\varrho}^s (\tilde{w}^s)^2 \tag{4.41}$$

where the simplest form of the dissipation energy $T\gamma$ is assumed as $\frac{1}{2}\sum_s B\tilde{\varrho}^s(\tilde{w}^s)^2$ and B is a coefficient with unit of [Pa·s]. Then the velocity of each dislocation family can be obtained from Eq. 4.40 via the principle of maximum dissipation rate (PMEP) [59].

$$\tilde{w}^s = \frac{b}{B} \Big(\underbrace{\tilde{M}_{\alpha\gamma} s^s_\gamma n^s_\alpha}_{\tau^s_{\text{rss}}} - \underbrace{\mu^s_{,N} G^P_{N\gamma} s^s_\gamma / b}_{\tau^s_{\text{back}}} \Big) \tag{4.42}$$

Plugging Eq. 4.42 into Eq. 4.29 gives the governing equation for ϱ^s:

$$\dot{\varrho}^s + \left(\frac{\tilde{M}_{\alpha\gamma} b s^s_\gamma n^s_\alpha - \mu^s_{,N} G^P_{N\gamma} s^s_\gamma}{B} \varrho^s \tilde{s}^s_\chi G^P_{K\chi} \right)_{,K} = P^s \tag{4.43}$$

Both resolved shear stress τ^s_{rss} and back stress τ^s_{back} need to be computed from free energy density $\tilde{W}$. We assume that the free energy density has the form

$$\psi(\boldsymbol{E}^E, T, \varrho^s) = \psi_E(\boldsymbol{E}^E) + \psi_M(\varrho^s) \tag{4.44}$$

---

[4] $E^e_{\alpha\beta} = G^P_{I\alpha}(E_{IJ} - E^P_{IJ}) G^P_{J\beta}$; $\frac{E^e_{\alpha\beta}}{\partial E_{IJ}} = G^P_{I\alpha} G^P_{J\beta}$

[5] $M_{\alpha\gamma} = \frac{\partial \tilde{W}}{\partial E^e_{\alpha\beta}} F^e_{i\gamma} F^e_{i\beta} = \frac{1}{J^P} P_{iK} F^P_{\alpha K} G^E_{\beta i} F^e_{j\beta} F^e_{j\gamma} = \frac{1}{J^P} P_{iK} F^P_{\alpha K} F^e_{i\gamma}$; $\boldsymbol{M} = \frac{1}{J^P} \boldsymbol{F}^P \boldsymbol{P}^T \boldsymbol{F}^E$

[6] If we let $\jmath^s_\chi = \tilde{\varrho}^s \tilde{w}^s s^s_\chi$, then $\tilde{L}^{Ps}_{\gamma\delta} \equiv b^s_\gamma \epsilon_{\delta\mu\chi} \tilde{\xi}^s_\mu \tilde{\varrho}^s \tilde{w}^s s^s_\chi = b^s_\gamma \tilde{\varrho}^s \tilde{w}^s n^s_\delta$, where $\boldsymbol{n} = \boldsymbol{\xi} \times \boldsymbol{s}$; since $\boldsymbol{s} \cdot \boldsymbol{n} = 0$, then $\delta_{\gamma\delta} \tilde{W} \sum_s b^s_\gamma \tilde{\varrho}^s \tilde{w}^s n^s_\delta = 0$

where ψ_E is the elastic energy density which can be determined from Table 2.1. ψ_M is microstructural energy. Berdichevsky *et al.* [33] proposed the simple expression

$$\psi_M(\varrho^1, \varrho^2, \ldots) = \hat{\psi}_M(\varrho^T(\varrho^1, \varrho^2, \ldots)) = kG \ln \frac{1}{1 - \varrho^T/\varrho^*} \tag{4.45}$$

With this choice, the chemical potential is same for all scalar dislocation densities, and back stress becomes proportional to the gradient of the total density

$$\mu^s = \frac{\partial \psi_M}{\partial \varrho^T} \frac{\partial \varrho^T}{\partial \varrho^s} = \frac{J^P kG}{\varrho^* - \varrho^T} \qquad \text{and} \qquad \mu^s_{,N} = \frac{J^P kG}{(\varrho^* - \varrho^T)^2}\, \varrho^T_{,N}\, . \tag{4.46}$$

4.2.2 Model Validation

Due to its simplicity and the need for the minimal specimen preparation, indentation has been used as a non-destructive method to probe properties of materials. The indentation size effect (ISE) which indicates that the hardness of self-similar indenters increases with decreasing indentation depth. And this effect was rationalized by Nix and Gao [60] in terms of geometrically necessary dislocations (GND) accumulating under the indenter. This implies that indentation reveals some fundamental properties of plasticity, such as dislocation structures below the indenter.

To validate the proposed dislocation-based crystal plasticity model, a model used for simulation was built based on the indentation experiment done by Kysar *et al.*[2], where a single nickel crystal is indented with a wedge indenter such that a two-dimensional deformation state with three effective plane strain slip systems is induced. The line loading induces plane strain deformation in the (110) plane by equally activating pairs of slip systems with identical in-plane components of the Burgers vector but opposite out-of plane component. Therefore, the deformation is equivalent to that produced by six effective slip systems of edge dislocations with slip direction and glide plane normal fully contained in the (110) plane, as shown in Fig. 4.5 and Table 4.3.

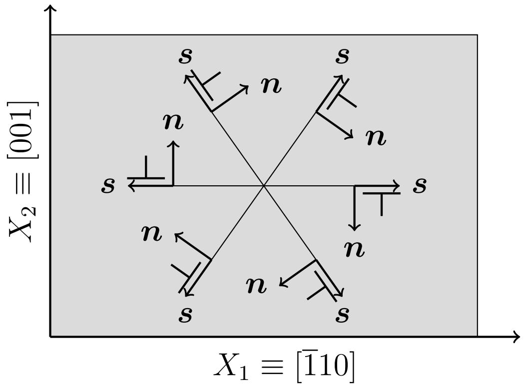

Figure 4.5: View of the (110) plane showing the six effective slip systems

r	$\boldsymbol{\xi}$	$\tilde{\boldsymbol{s}}$	$\tilde{\boldsymbol{n}} = \tilde{\boldsymbol{s}} \times \tilde{\boldsymbol{\xi}}$
1	$[0, 0, 1]$	$[1, 0, 0]$	[0,-1,0]
2	$[0, 0, 1]$	[-1,0,0]	[0,1,0]
3	$[0, 0, 1]$	$[\sqrt{\frac{1}{3}}, \sqrt{\frac{2}{3}}, 0]$	$[\sqrt{\frac{2}{3}}, -\sqrt{\frac{1}{3}}, 0]$
4	$[0, 0, 1]$	$[-\sqrt{\frac{1}{3}}, \sqrt{\frac{2}{3}}, 0]$	$[\sqrt{\frac{2}{3}}, \sqrt{\frac{1}{3}}, 0]$
5	$[0, 0, 1]$	$[-\sqrt{\frac{1}{3}}, -\sqrt{\frac{2}{3}}, 0]$	$[-\sqrt{\frac{2}{3}}, \sqrt{\frac{1}{3}}, 0]$
6	$[0, 0, 1]$	$[\sqrt{\frac{1}{3}}, -\sqrt{\frac{2}{3}}, 0]$	$[-\sqrt{\frac{2}{3}}, -\sqrt{\frac{1}{3}}, 0]$

Table 4.3: Six effective slip systems

As shown in Fig. 4.6, we consider a simulation domain of width $W = 600\mu m$ and height $H = 550\mu m$. A region of infinite elements surrounds this domain on the left, bottom, and right sides. This allows the prescription of boundary conditions on these sides at infinity. The top surface is indented by a rigid 90° wedge with a tip radius of $R = 10\mu m$. The indenter is pushed into the Ni crystal material in increments of $0.5\mu m$, for a total indentation of depth of $100\mu m$. The dislocation density on each slip system is initialized as a uniform field $\varrho^r(\boldsymbol{X}, 0) = \varrho_0 = 10^{12}$ m^{-2} at time $t = 0$. We also assume that the crystal is initially plastically undistorted, that is $\boldsymbol{F}^P(\boldsymbol{X}, 0) = \boldsymbol{I}$. Using these initial conditions, the sequential solution scheme illustrated in Fig. 4.8 is implemented to find the displacement field $\boldsymbol{u}$, the plastic distortion field $\boldsymbol{F}^P$, and the dislocation density fields on each slip system ϱ^r $(r = 1, ..., 6)$.

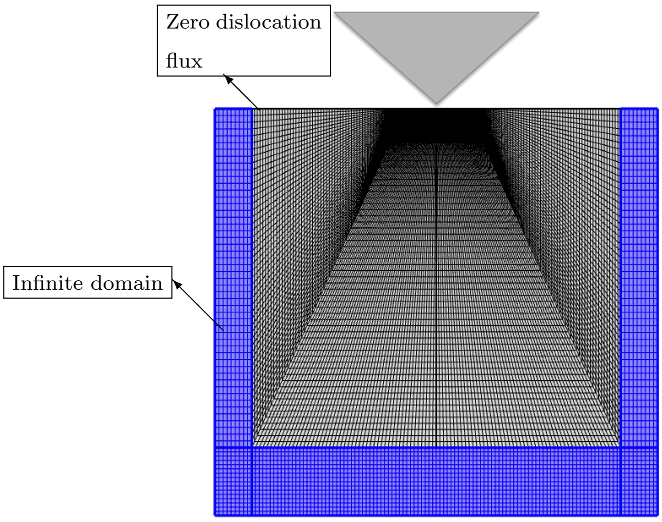

Figure 4.6: Model domain with infinite elements

Burgers vector magnitude [Å]	b	2.489
Lamé parameter [GPa]	λ	147.3
Lamé parameter [GPa]	μ	124.7
mobility coefficient [Pa·s]	B_0	10^{-4}
microstructural energy parameter	k	10^{-4}
saturation density [m^{-2}]	ϱ^*	10^{14}
initial dislocation density [m^{-2}]	ϱ_0	10^{12}
Frank Read source density [m^{-2}]	ϱ_{FR}	10^{12}

Figure 4.7: Material properties

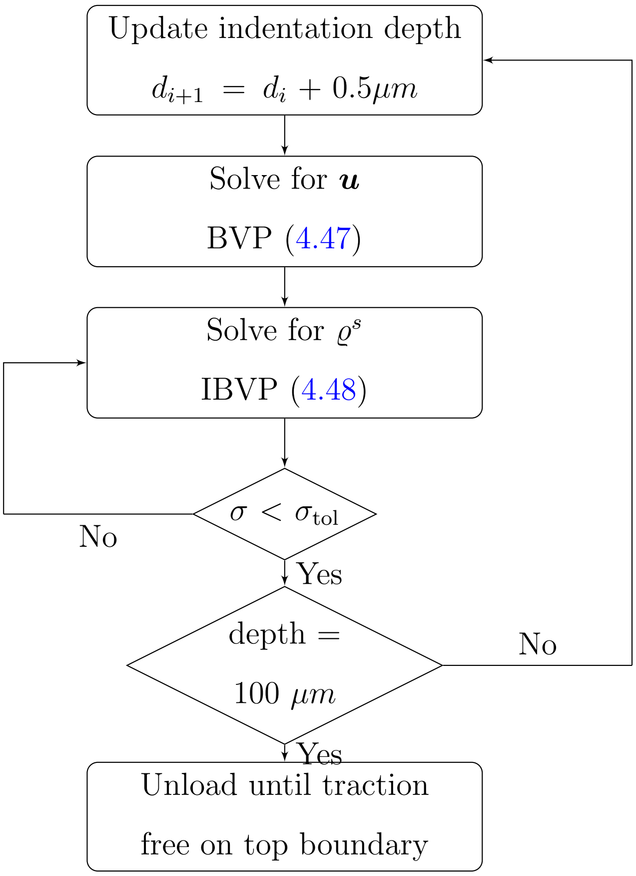

Figure 4.8: Flowchart of simulation process

Generally, the numerical model contains three sets of PDE or ODE, which are: (1) one PDE to solve for displacement field $\boldsymbol{u}$ (2) one convection PDE to solve for dislocation density field ϱ^r on each slip system r (3) one ODE to solve for plastic distortion field $\boldsymbol{F}^P$. At each indentation increment we solve the following quasi-static weak form equation to solve for displacement field $\boldsymbol{u}$

$$\int_\Omega P_{iJ}\delta u_{i,J}\,\mathrm{d}V = \int_{\partial\Omega_{\mathrm{top}}} fJG_{Kj}\delta u_j\,\mathrm{d}A_I \tag{4.47}$$

The weak form Eq. 4.47 is solved at each indenter increment for fixed $\boldsymbol{F}^P$ from previous step. Once the solution $\boldsymbol{u}$ is found, the initial boundary value problem (IBVP) governing the time evolution of each dislocation density is solved. The weak form equation corresponding to Eq. 4.43 is

$$\int_\Omega \left(\dot{\varrho}^r\delta\varrho^r - \varrho^r w^r_K\delta\varrho^r_{,K}\right)\mathrm{d}V + \int_{\partial\Omega_{\mathrm{out}}} \varrho^r w^r_K\delta\varrho^r\,\mathrm{d}A_K = \int_\Omega p^r\delta\varrho^r\,\mathrm{d}V \tag{4.48}$$

We also solve the plastic deformation by solving the spatially-dependent initial value problem (IVP). The corresponding weak form is

$$\int_\Omega \dot{F}^P_{\gamma J}\delta F^P_{\gamma J}\,\mathrm{d}V = \int_\Omega \sum_r \tilde{b}\tilde{\varrho}^r\tilde{w}^r\tilde{s}^r_\gamma\tilde{n}^r_\delta F^P_{\delta J}\delta F^P_{\gamma J}\,\mathrm{d}V \tag{4.49}$$

In the experiment [2], the in-plane lattice rotation of the crystal lattice is measured with a three micrometer spatial resolution using Orientation Imaging Microscopy (OIM), as Fig. 4.9(b) shows. In our simulation model, the lattice rotation angle about the out-of-plane direction, ω_3, is computed using the polar decomposition of the elastic deformation tensor as $\boldsymbol{F}^E = \boldsymbol{R}^E\boldsymbol{U}^E$, where $\boldsymbol{R}^E$ is the orthogonal matrix of lattice rotation. The lattice rotation computed from our model is shown in Fig. 4.9(a). It can be observed that the lattice rotation underneath the indenter exhibits four sectors of alternating sign, as predicted by the theory of [61].

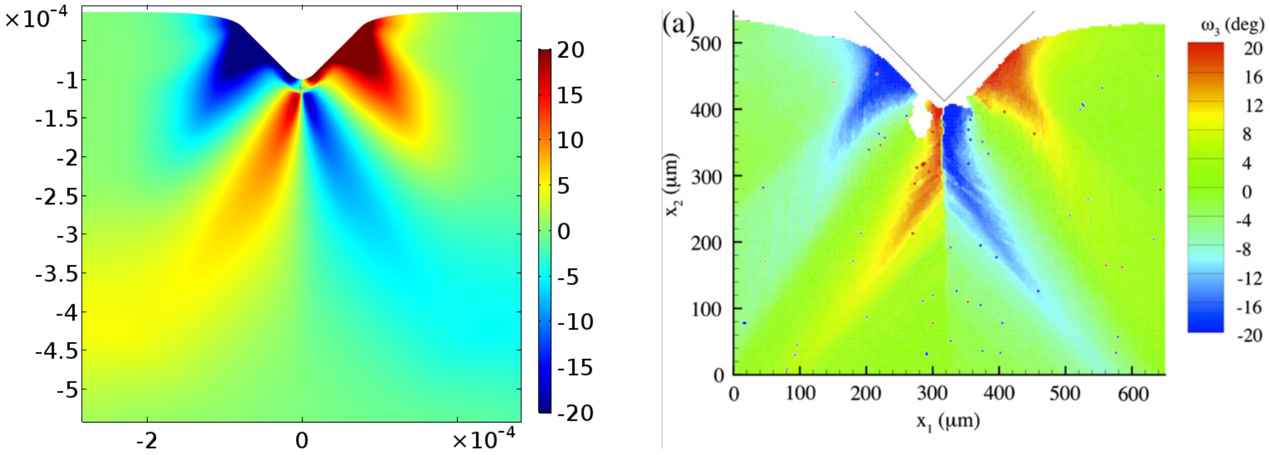

(a) (b)

Figure 4.9: (a) Lattice rotation from simulation. (b) Lattice rotation from experiment [2]

Besides, all non-zero components of the Nye dislocation density tensor are calculated from the lattice rotation field, as shown in Fig. 4.10(a) and Fig. 4.10(c). The black lines superimposed to the figures represent deformed lattice planes. Fig. 4.10(a) shows a concentration of positive Burgers vector density on the vertical line under the indenter, and on two lateral lines that originate approximately at the points of contact of the wedge indenter with top surface of the material. Fig. 4.10(b) and Fig. 4.10(d) and 4.10(d) show the corresponding components of α_{13} and α_{23} obtained by [2] by post-processing the lattice rotation

$$\alpha_{ij} = \omega_{j,i} - \delta_{ij}\omega_{k,k} \tag{4.50}$$

Despite the fact that the experimental results show sharper regions of high density, it can be observed that general pattern is well reproduced for both fields α_{13} and α_{23}.

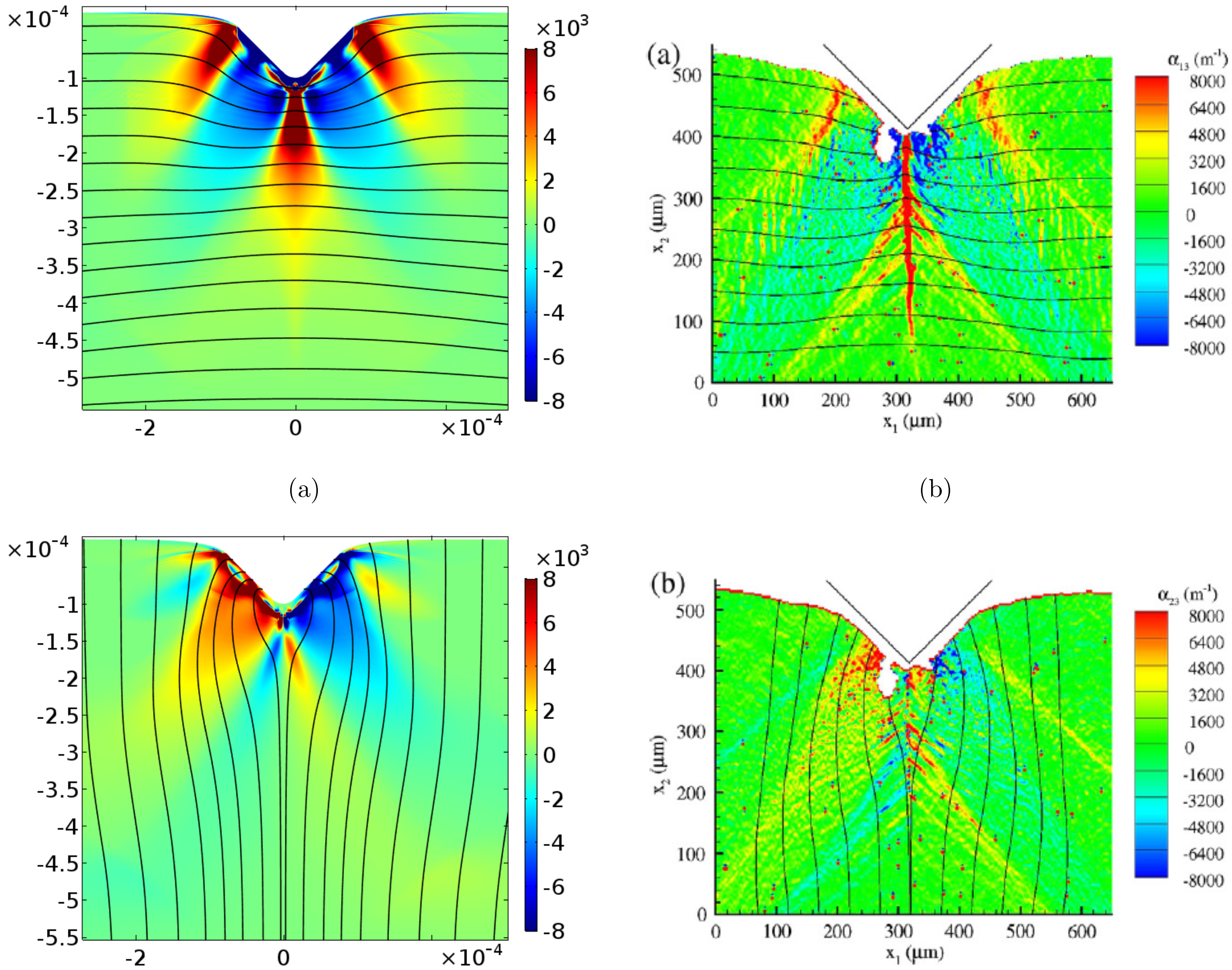

(a) (b)

(c) (d)

Figure 4.10: (a) α_{13} from simulation. (b) α_{13} from experiment [2]. (c) α_{23} from simulation. (d) α_{23} from experiment[2].

Next, we consider the distribution of scalar densities on each slip system. In experiments, the problem of reconstructing the densities ϱ^r given $\boldsymbol{\alpha}$ amounts to solving the equation

$$\sum_r \varrho^r \begin{bmatrix} b_x^r \\ b_y^r \end{bmatrix} = \begin{bmatrix} \alpha_{13} \\ \alpha_{23} \end{bmatrix}, \tag{4.51}$$

which is underdetermined for more than two families of dislocations. Kysar *et. al* [2] have eliminated this under-determinacy by requiring that the net dislocation density on each slip system minimizes the L^1-norm defined as $L^1 = \sum_\alpha |\varrho^\alpha|_{\mathrm{GND}} b^\alpha$. Results of these calculations were interpreted by Kysar as a "lower bound" estimate of the actual dislocation population, and they are reported in the first column of Fig. 4.11. The second column of Fig. 4.11 shows the result of the same calculation using the results of our simulations. It can be observed that for all densities there is very good agreement between corresponding results. Clearly, our model also has full knowledge of the six dislocation density fields ϱ^r, therefore we compare these actual densities to their lower-bound estimates. These results are reported in the third column of Fig. 4.11. It is not surprising to see that the actual density pattern is quite different from the lower-bound estimate. In general, the lower bound estimate predicts sharp interfaces in the dislocation density structure, which are not observed for the actual density fields. For example, there is a sharp transition across the vertical midline of Figs. 4.11(d) and 4.11(e), which is not observed in Fig. 4.11(f).

In this section, a finite deformation dislocation-based crystal plasticity model which is able to reproduce the dislocation microstructure measured in the wedge micro-indentation experiment of [2] is proposed. The incompatible plastic component of deformation is determined from the flux of dislocations on different and interacting slip systems. Both lattice rotation and Nye tensor information match the experimental results qualitatively and quantitatively.

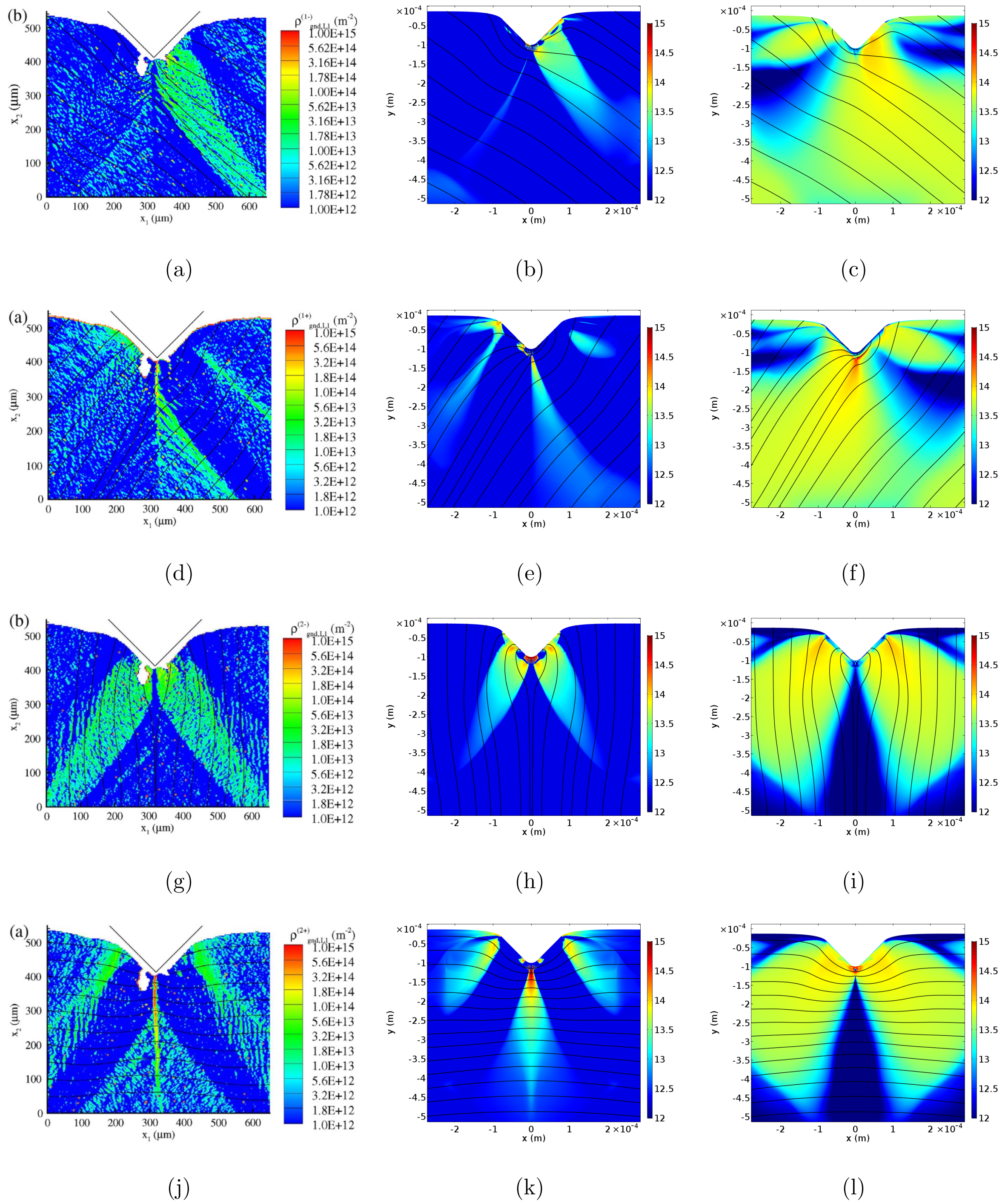

(a) (b) (c)

(d) (e) (f)

(g) (h) (i)

(j) (k) (l)

Figure 4.11: Comparison between experimental lower-bound dislocation density (first column), simulate lower-bound dislocation density (second column), and actual simulated density (third column), for each slip system. (a)-(b)-(c) $\varrho^{(1)}$. (d)-(e)-(f) $\varrho^{(2)}$. (g)-(h)-(i) $\varrho^{(3)}$. (j)-(k)-(l) $\varrho^{(4)}$. Densities $\varrho^{(5)}$ and $\varrho^{(6)}$ are not reported for symmetry reasons.

4.3 Cohesive Zone Model for Crack Propagation

In this work, cohesive zone model(CZM) is utilized to simulate the fracture and crack propagations in polycrystalline solids. CZM is typically expressed as a function of normal and tangential tractions in terms of separation distances. Consider two adjacent grain domains $\mathbf{\Omega_1}$ and $\mathbf{\Omega_2}$ connected by a common boundary $\mathbf{S}$ (grain boundary) as shown in Fig. 4.12(a). If $\mathbf{S}$ separates(fractures) to $\boldsymbol{S_1}$ and $\boldsymbol{S_2}$ as shown in Fig. 4.12(b), then the process creates a new domain $\mathbf{\Omega^*}$, which can be shrunk to an infinitesimally thin surface but can be expanded to a domain. The constitutive relation of $\mathbf{\Omega^*}$ is expressed in terms of the normal and shear tractions and their corresponding separation displacements. A typical relation of $\mathbf{\Omega^*}$ is given by Traction-Separation relations. If the separation distance exceeds a critical value, $|\bar{\delta}| > |\bar{\delta}_{\text{crit}}|$, the traction is assumed to be identically zero within $\mathbf{\Omega^*}$.

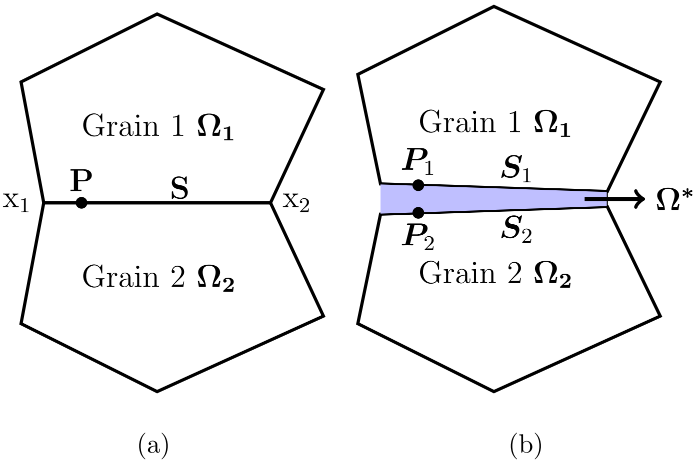

Figure 4.12: Framework of cohesive zone model for grain boundary (a) Reference configuration (b) Current configuration

The simulated model is a 100 μm by 100 μm, two dimensional block, which was divided into 10 randomly distributed grains, as shown in Fig. 4.13. Each grain has two randomly orientated {110}[111] slip systems. Thermal boundary conditions were prescribed as an inward heat flux value, 25 MW/m^2, with a duration of 0.15 s on the left side. A convective heat flux boundary condition was applied on the right side, representing the helium cooling. The mechanical boundary conditions were taken as zero x-displacement on both left and right side, while the top-right corner point was fixed.

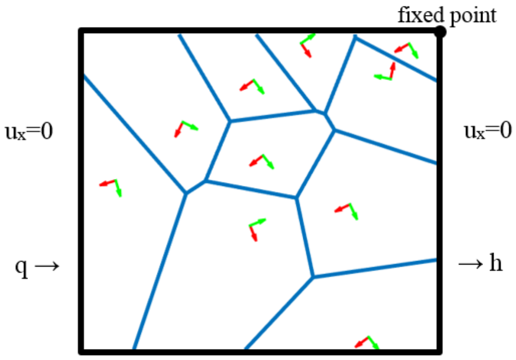

Figure 4.13: Boundary conditions on randomly distributed polycrystal grains

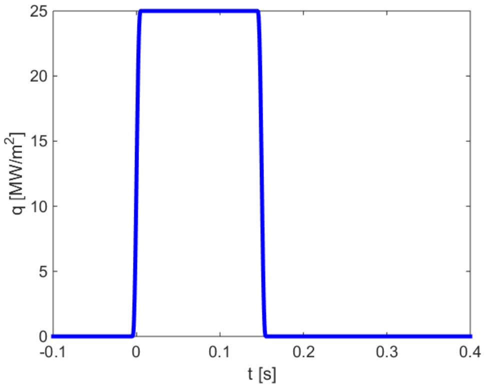

Figure 4.14: Inward heat flux profile

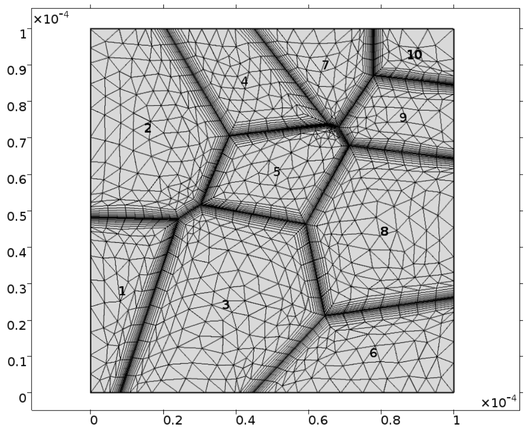

Figure 4.15: Grain domains with boundary layer mesh

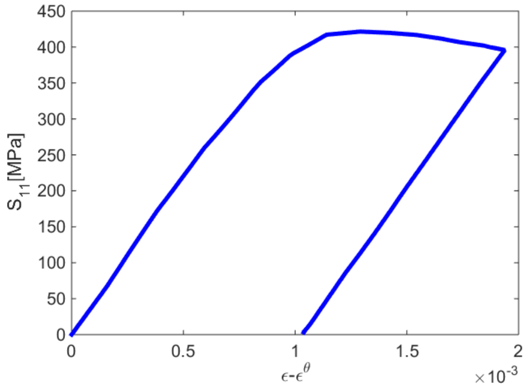

Figure 4.16: Stress-strain path at a specific point

Fig. 4.17 shows the S_{xx} distribution at the peak temperature. The red arrows on the grain boundaries indicate the magnitude of the damage. Most of the damage occurs on the horizontal grain boundaries since the domain is free to expand in y direction. Fig. 4.18 shows the temperature distribution at 0.18 [s], when the domain is cooled down to the level near initial temperature. Red arrows indicate that the current separation distance between two adjacent grains is greater than a critical fracture value u_f and heat cannot transfer across the boundaries. This could explain that domain 2 has a relatively higher temperature than others.

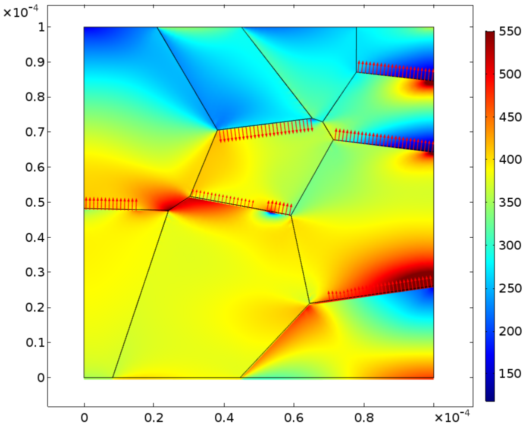

Figure 4.17: S_{xx} [MPa] at peak temperature

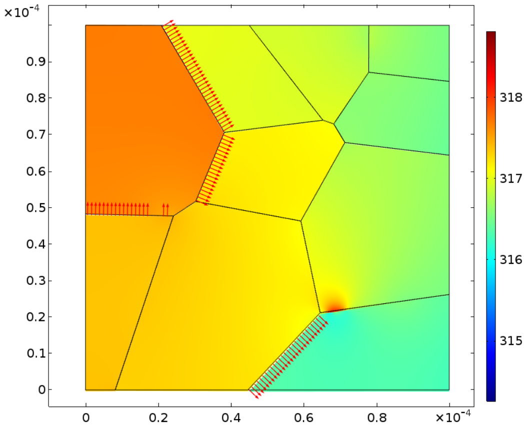

Figure 4.18: Temperature [K] after cooling down

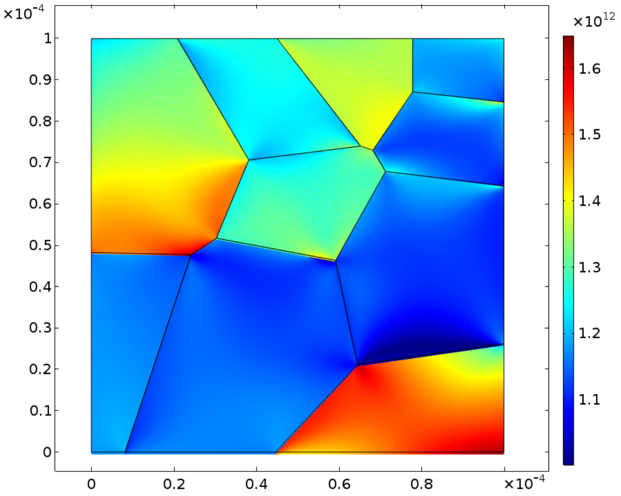

Figure 4.19: Dislocation density on slip system 1

CHAPTER 5

Design Applications

The motivation of developing multiscale-multiphysics approach is for design optimization of complex systems. Several previous design studies [62, 63] have shown that energy conversion components, like blankets and divertors in a fusion power plant, will become significantly more complex in order to provide the multiple functions of extracting heat for thermal conversion, in addition to breeding tritium for fuel. The structural design of these components must meet strict thermal and structural design limits, while maintaining credible manufacturable configuration and maintenance characteristics. Thus these two components are perfect candidates for demonstration of multiscale-multiphysics approach.

Three examples are presented in this chapter. We started from the multiphysics simulation on the FW/Blanket of U.S. Fusion Nuclear Science Facility to demonstrate the feasibility of the multiphysics approach proposed in Sec. 3.1, followed by implementing the comprehensive multiphysics-multiscale design approach on the DEMO water-cooled blanket. Lastly, design optimization was implemented on the monoblock divertor design to show how we improve our design based on the simulation results.

5.1 The FW/Blanket of the U.S. Fusion Nuclear Science Facility (FNSF)

The realization of fusion energy has to face a number of technical challenges. Many programs are now under development to demonstrate that candidate solutions to these challenges will also work at the scale of a reactor. As discussed in the Sec. 5.2, the first commercial demonstration fusion power plant, named DEMO, has been proposed as a demonstration of the commercial feasibility, and as a natural follow-up of the ITER project. However, there are many technical gaps that exist between ITER and DEMO, and such gaps must be bridged with additional research and test facilities. Therefore, the Fusion Nuclear Science Facility (FNSF) has been recently proposed in the U.S. to provide a technical basis for DEMO. It is thus an intermediate step to demonstrate the complex integration of components in the extreme fusion nuclear environment, and to provide a test bed for integrated nuclear science and plasma physics.

5.1.1 Blanket System Integration

FNSF utilizes a full-sector maintenance approach in which all of the components located inside the vacuum vessel are contained within 16 steel structural rings that move horizontally on rails between TF coils, as shown in Figs. 5.1 and 5.2.

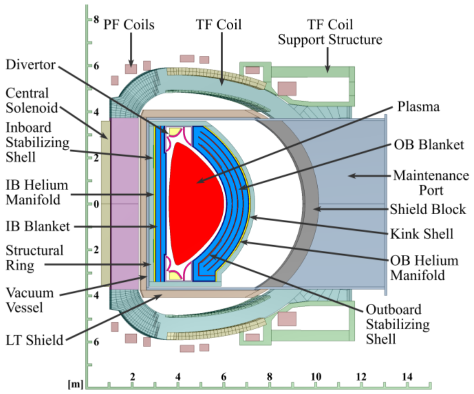

Figure 5.1: Elevation view of the FNSF power core

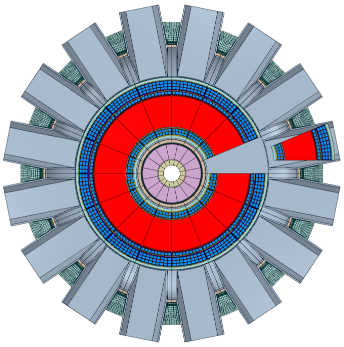

Figure 5.2: Plan view of the FNSF power core

For the purpose of the analyses described here, we considered a slice of the inboard blanket in a mid-plane region away from penetrations and manifolds; the cross section for one sector is shown in Fig. 5.3.

Fig. 5.3 also depicts the two independent coolants. Helium cools the first wall and steel structures, while PbLi liquid breeder flows within SiC inserts that thermally and electrically insulate the PbLi from steel. A thin layer of PbLi penetrates the gap between the SiC inserts

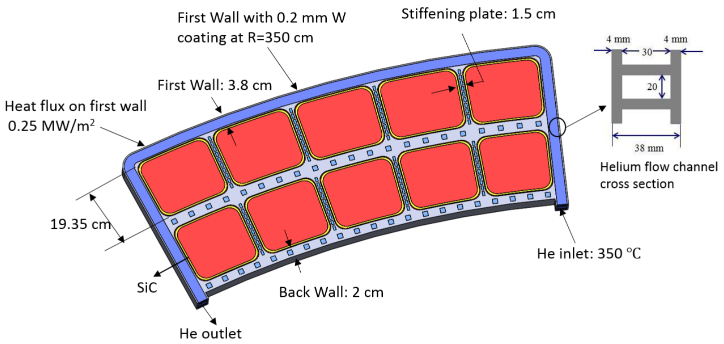

Figure 5.3: Mid-plane cross-section of a 3D CAD model of the inboard blanket

and steel.

The coolant inlet and outlet temperatures are chosen to maintain the steel structures within the operating range determined by irradiation-induced reduction in DBTT (350 °C), high temperature creep strength (550 °C), and compatibility limits with PbLi (470 °C). The compatibility limit is based on wall thinning, and has been used in many PbLi-cooled blanket studies in the past [64]. The expected mass loss of RAFM steels in PbLi under such conditions could be found in [65]. In the baseline design, He exits the first wall at 416 °C and exits the blanket at 475 °C. Due to the rather large channel size and modest velocity, the pressure drop and pumping power in the first wall are low. The ratio of pumping power to thermal power removed is less than 1%. The plasma-facing surface is textured to improve heat transfer with 200 μm roughness height.

5.1.2 Results

- Helium flow

As Fig. 5.4 shows, helium flow velocity should be at least 28 m/s under 8 MPa operating pressure and 46 m/s under 5 MPa to maintain the steel structure temperature below the maximum limit. It is clear that we would have to pay for higher pumping power to reduce the operating pressure. The streamlines of helium flow with velocity magnitude are shown in Fig. 5.5 (with pressure of 8 MPa and inlet velocity of 30 m/s).

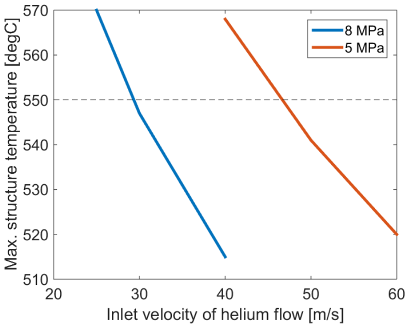

Figure 5.4: Max. structure temperature v.s. inlet velocity

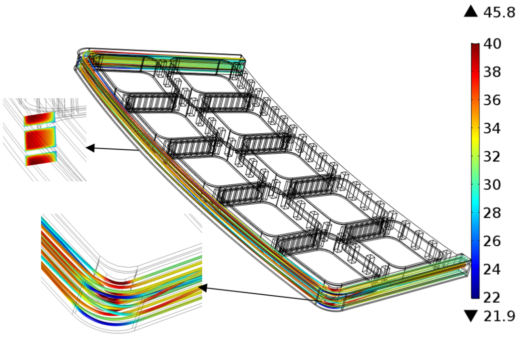

Figure 5.5: Streamlines of helium flow

- Temperature distribution of the solid structure

The result of the temperature distribution is shown in Fig. 5.6. The maximum temperature of the LiPb coolant is around 600 °C at the mid-plane. The temperature distribution is relatively uniform due to the alternating arrangement of coolant. By controlling the inlet helium velocity, the maximum temperature of the steel structure can be maintained below the limit. Even with the operating pressure of 5 MPa, only a velocity of 46 m/s is required. The results reveal that the turbulent flow together with roughening the effective cooling.

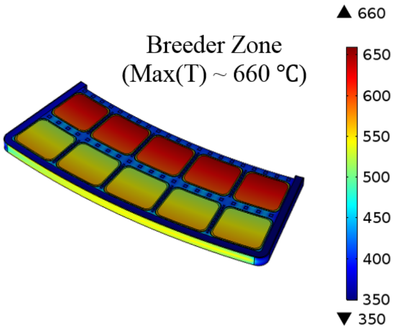

Figure 5.6: Temperature in breeding zone

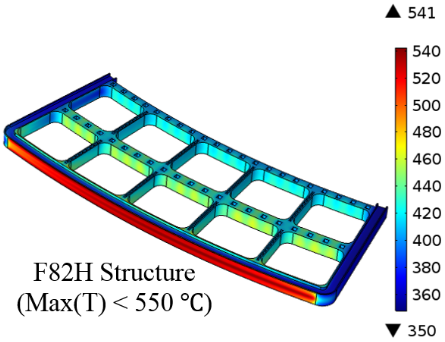

Figure 5.7: Temperature in blanket structure

- Primary and thermal stress

The following results shown in the figures below are based on normal operating conditions with a helium pressure of 8 MPa. Results of other cases (off-normal conditions or 5 MPa pressure) are listed in Tables 5.1- 5.3. Fig. 5.8 shows the global primary stress distribution of the blanket structure. There are stress concentrations at the junctions and corners. After rounding and adding fillets to junction zones, the maximum primary stress was reduced to about 320 MPa.

Thermal stress was calculated based on the temperature obtained from coupled heat transfer and CFD analyses. As illustrated in Fig. 5.9, the first wall has the largest thermal stress, although a directionally-alternating cooling channel layout has already reduced severe temperature gradients. Also, thermal expansion illustrates the reason why we need to leave a gap of at least 2 cm between adjacent sectors during assembly to accommodate thermal expansion.

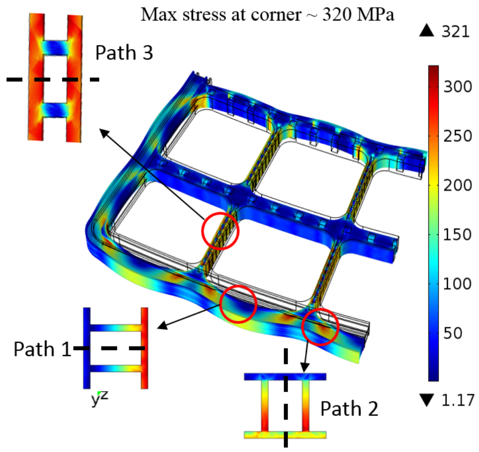

Figure 5.8: Primary stress distribution

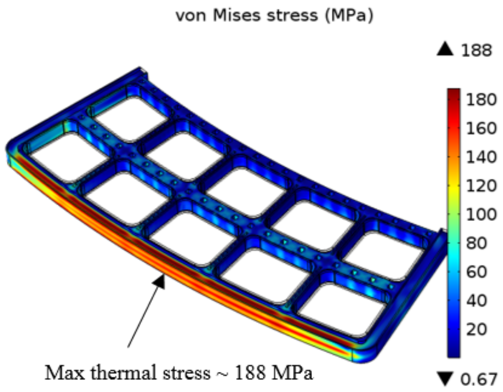

Figure 5.9: Thermal stress distribution

- Design factors of safety

Line integration through the thickness of the structure is usedto resolve stresses into membrane, bending and non-linear compo-nents. The membrane stress tensor has components that are equalto the mean value of stresses through the thickness. The bendingstress tensor has components that vary linearly through the thick-ness and which, when integrated through the thickness result inequilibrium with the section moment [66]. The line along whichthis integration is carried out is defined as a supporting line seg-ment. Three supporting line segments were selected as criticalpaths to determine the design safety factors, as shown in Fig. 5.8.

With the results of the primary and thermal stresses, factors of safety were determined based on the three different allowable values and the low temperature design criteria. The results are shown in Tables 5.1- 5.3. For reference on the mechanical design procedure, including stress intensity parameters and design criteria, please see reference [66].

Design Criteria: $\overline{P_m + P_b} \leq 1.5S_m$						
	5 MPa			8 MPa		
Path	$1.5S_m$ [MPa]	Normal	Off-normal	$1.5S_m$ [MPa]	Normal	Off-normal
1	205.8	4.6	1.7	204.1	4.0	1.1
2	206.7	4.3	1.7	205.0	3.7	1.0
3	228.8	5.8	2.0	228.8	5.4	1.3

Table 5.1: Factors of safety based on necking and plastic instability limit.

Design Criteria: $\overline{P_m} + Q \leq S_e$						
	5 MPa			8 MPa		
Path	S_e [MPa]	Normal	Off-normal	S_e [MPa]	Normal	Off-normal
1	193.6	7.2	3.6	191.9	5.8	2.3
2	194.4	7.0	3.7	192.8	5.7	2.4
3	215.3	6.5	2.0	215.2	6.2	1.2

Table 5.2: Factors of safety based on plastic flow localization limit.

Design Criteria: $\overline{P_m} + P_b + Q \leq S_d$						
	5 MPa			8 MPa		
Path	S_d [MPa]	Normal	Off-normal	S_d [MPa]	Normal	Off-normal
1	387.1	4.2	5.2	383.9	4.3	3.2
2	388.9	2.9	2.5	385.7	3.0	2.0
3	430.5	8.8	3.6	430.4	8.4	2.3

Table 5.3: Factors of safety based on ductility exhaustion limit.

The current results indicate that the FW/Blanket structure,under normal operating conditions, meets all design criteria,while the safety factors under off-normal operating conditions are marginal. Therefore, it is recommended that further design optimization and parametric analyses be conducted.

5.1.3 Conclusions

We have demonstrated the feasibility of multiphysics design and optimization of the FW Blanket system, coupling fluid flow,heat transfer in fluids, heat transfer in solids, thermal stress, and mechanical stress simulations. The simulation results of elastic analysis, including the temperature, velocity and pressure field of coolant flow as well as temperature and stress field of RAFS structure, have been obtained under both normal and off-normal operating conditions. The thermo-mechanical analyses showed that the helium velocity is required to be at least 30 m/s and 50 m/s to maintain the structure temperature below the limit (550 °C),under 8 MPa and 5 MPa operating pressure respectively. By applying the SDC-IC design criteria, factors of safety were calculated and from these we conclude that the current design could withstand the combined loads of thermal and coolant, though the primary stress under 8 MPa off-normal condition was marginal. The parametric analyses on the first wall cooling channel dimensions showed that increasing either the first wall thickness or helium channel thickness by 2 mm could effectively reduce the primary stress to make the design more robust.

5.2 DEMO Water Cooled Lithium-Lead (WCLL) Breeding Blanket

5.2.1 Introduction

Europe has a leading position in this field and EuroFusion is now developing a demonstration fusion power plant (DEMO), producing net electricity for the grid at the level of a few hundred Megawatts is foreseen to start operation in the early 2040s [67].

A new design of the WCLL BB for DEMO fusion reactor was proposed in 2015 [68]. The goal of multiphysics-multiscale analyses of WCLL BB is to deliver a reference design that satisfies the design requirements. The WCLL BB uses reduced activation ferritic-martensitic steel Eurofer as structural material filled with Lithium-Lead (PbLi) as breeder, neutron multiplier and tritium carrier, and water at typical Pressurized Water Reactor (PWR) conditions ($T_{in} = 285°C$, $T_{out} = 325°C$ at 15.5 MPa) as coolant. The water flows in Double-Wall Tubes (DWT). The DWT are used to minimize the probability of water/PbLi interaction in order to reduce the probability of leakage within the module.

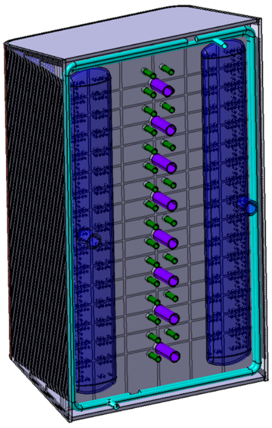

Figure 5.10: WCLL outboard module isometric view

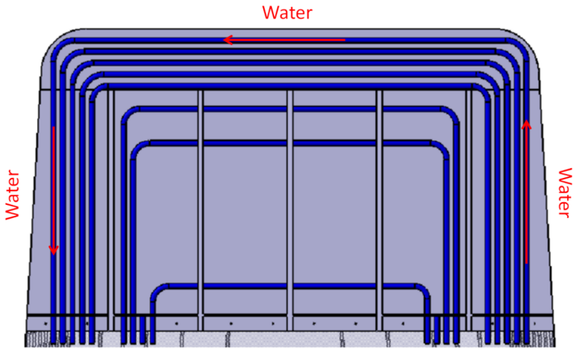

Figure 5.11: Water cooling tubes of the Breeding Zone

The module consists of an Eurofer steel box (Fig. 5.10 [68]), reinforced by an internal grid of radial-poloidal and poloidal-toroidal plates in order to withstand water pressure in case of accidental pressurization. The front part of the WCLL BB system is the First Wall

(FW), which is an integrated part of the module. The FW is an U-shape plate bended in radial direction, the bended radius is of about 150 mm. The thickness of the FW is of 25 mm. Moreover, the FW is covered by a tungsten layer of 2 mm thickness on the plasma facing area.

The breeding zone water cooling tubes are placed along a toroidal-radial direction, and the layout is shown in Fig. 5.11. The tubes are double walled and have the external diameter of 13.5 mm, the internal diameter of 8 mm and the thickness is 1.25 mm.

For the simulation, only the section on a poloidal mid-plane of an elementary cell,as shown in Fig. 5.13, was studied since the elementary cell is repetitive along the poloidal direction.

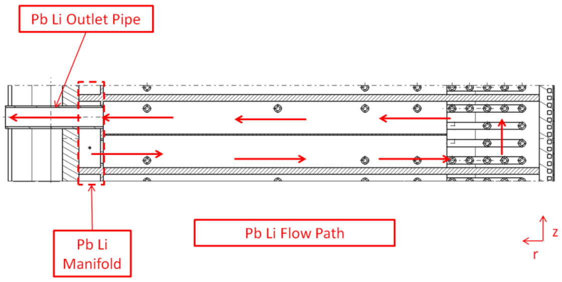

Figure 5.12: Section on flow path of PbLi in a single cell of the module

Figure 5.13: WCLL BB CAD model

5.2.2 Methodology

The thermo-mechanical behavior of DEMO WCLL blanket has been investigated by [35]. The mechanical behavior of the structural material EUROFER has been simulated with a linear elastic model and the results were verified by SDC-IC code. Here we proposed a more sophisticated computational approach based on the FEM framework.

The modeling process includes two parts, as shown in Fig. 5.14. The first part is a thermo-hydraulic analysis coupling the conjugate heat transfer and fluid dynamics to obtain the temperature field in structure, breeder and coolant. The second part is a more advanced multiscale structural analysis approach, including three enhanced elastic analysis methods, both static an transient elasto-plastic analyses under cyclic thermal loading and finally fracture analysis with MS-FAD method.

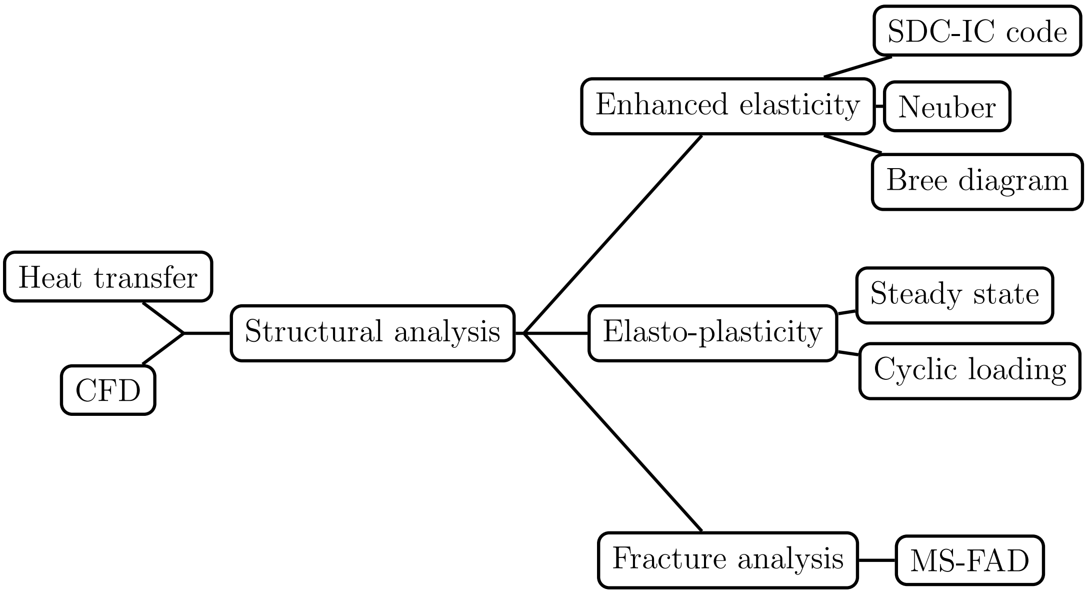

Figure 5.14: Summary of multiphyscis model

Three major physics including heat transfer, fluid dynamics and solid mechanics have been coupled and incorporated into an integrated simulation framework. Forced convective heat transfer takes place between cooling water and both FW channels and double-walled tubes in the breeder. A simplified approach was adopted to simulate this forced convective cooling by using a constant coolant bulk temperature and convective heat transfer coefficient computed from Dittus-Boelter correlation in previous work [35]. However, some studies [34] showed that 3D CFD analysis is necessary to get accurate heat transfer analysis results especially for the cases where heat flux is applied on one side only. In addition, the heat transfer coefficient is non-uniform along the cooling path, with higher values around the bending at the corners due to the abrupt velocity direction change of the coolant.

Therefore, a more accurate method for simulating forced convective cooling as discussed in Sec. 3.1.1 was implemented in this study. There are two sets of cooling channels in DEMO DCLL blanket. One elementary cell has 9 cooling channels in the FW and 14 cooling channels embedded in the breeder zone. The two sets of coolant were treated differently due to the differences in boundary conditions. There are three major reasons for our different strategies for FW cooling and breeder cooling: (1) The cooling channels in FW have rectangular cross section while the ones in breeder zone are round. The heat transfer coefficient correlations used were more suitable for round pipe cases [34]. (2) The coolant in the FW has one side facing the high heat flux while the coolant in the breeder is in the environment with a more uniform temperature. The correlation is more accurate with the uniform temperature environment. (3) We are more interested in the temperature distribution in FW structure than breeder zones. Thus we prefer a more accurate approach for FW cooling. Therefore, CFD and heat transfer were two-way coupled for FW cooling following Eq. 3.1 - 3.3, while a simplified approach following Eq. 3.4 - 3.7 was used for breeder cooling where the coolant flow domain was not modeled and its thermal effect was simulated by specifying a proper heat transfer coefficient based on the Sieder-Tate correlation on the fluid-structure interface.

Thermal-hydraulic analysis could provide the temperature distribution for the following structural analysis. Most of the previous work focused on the stationary elastic analysis with applying SDC-IC code, which is a strength-based design rule. Besides, the Bree diagram method [39] which capture the effects of thermal fluctuations on the strength limits was also applied.

To consider the plastic behavior of the material under thermal-mechanical loadings, the Neuber method [38] was firstly implemented without doing plastic analysis. This is followed by a stationary elasto-plastic analysis over the entire domain. The previous Neuber method could anticipate the material behavior under cyclic thermal loading, which can be verified by transient elaso-plastic analysis results. Since doing transient elasto-plastic analysis over the entire domain is computationally expensive and critical plastic zones are localized in several small regions, a global-local structural analysis framework is proposed here, as Fig. 5.16 shows. The process starts from a transient thermal-hydraulic analysis, based on which the global-local structural analysis is implemented at certain specific time t_i. The temperature of the structure and pressure distribution of coolant obtained from global thermal-hydraulic analysis was used as input for both global elastic and local plastic analyses.

At each time t_i, a global-local elasto-plastic analysis method was implemented. Based on the global elastic analysis results, a small region with highest stresses and temperature was selected as a subdomain for the local elasto-plastic analysis. In our case, the selected region is in the middle of the first wall, as shown in Fig. 5.22. The displacement results at the global-local interface obtained from the global elastic analysis were passed to the local domain as Dirichlet boundary conditions. To match the traction at the global-local interface, traction boundary conditions were applied on the global-local interface in the global domain based on the stress results from local analysis. The boundary conditions used for global-local coupling are summarized in Eq. 5.1.

$$\begin{cases} u_i^{\text{local}} = u_i^{\text{global}} & \text{on } \partial\Omega_{\text{int}} \quad \text{in } \Omega^{\text{local}} \\ t_i^{\text{global}} = \sigma_{ij}^{local} n_j & \text{on } \partial\Omega_{\text{int}} \quad \text{in } \Omega^{\text{global}} \end{cases} \tag{5.1}$$

Alternatively, a more self-consistent approach using interface Lagrange multipliers based on the variational principle as discussed in Sec. 2.3.3 can be used for global-local coupling. The method is reviewed here for refreshing. The key ingredients of the method are illustrated in Fig. 5.15. The interface is treated by a displacement frame u_{b_i} and localized Lagrange multipliers $\lambda_{l_i}^m$, leading to a modified form of the potential energy functional $\Pi_{\text{PEM}}(u_i^m, \lambda_{l_i}^m, u_{b_i}) = \sum_m \Pi_{\text{PE}}^m - \pi_u^m$, where m is the index of domain, π_u^m is the additional potential energy localized on the global-local interface and computed as $\int_{\partial\Omega_b} \lambda_{l_i}^m (u_i^m - u_{b_i}) dS$. By applying the variational principle, the additional functional term results in an additional expression $\int_{\partial\Omega_b} (u_{b_i} - u_i^m)\delta\lambda_{l_i}^m dS + \lambda_{l_i}^m(\delta u_{b_i} - \delta u_i^m) dS$ on the interface boundaries. This approach is able to provide matched displacement and traction fields on the interface naturally.

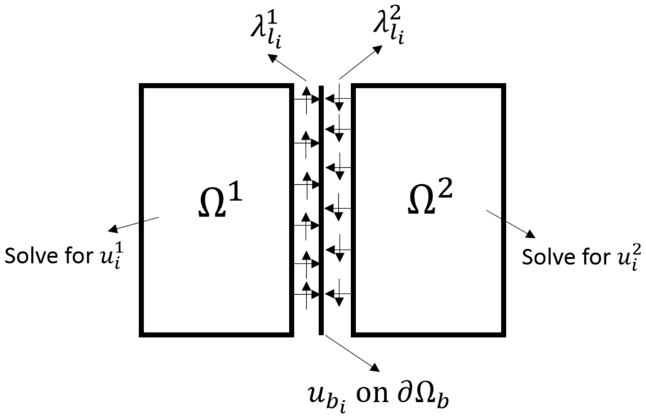

Figure 5.15: Localized Lagrangian multiplier field on interface boundary

In addition, since cyclic loading was applied in the simulation, the plastic strain needs to be stored to capture the material behavior during unloading. The entire simulation process including the coupling between the global (elastic) and local (elasto-plastic) analysis is depicted in Fig. 5.16.

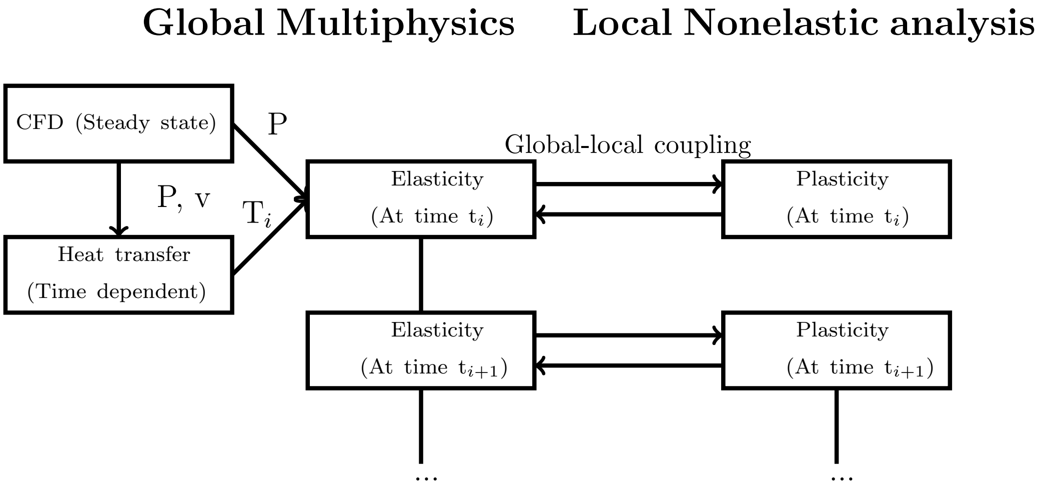

Figure 5.16: Numerical simulation framework

5.2.3 Thermo-mechanical loads and boundary conditions

Generally, both thermal and mechanical boundary conditions were applied on the model. Based on the thermal boundary conditions, power balance can be calculated to roughly estimate the cooling performance so that we could have a reasonable estimation on thermal-hydraulic parameters (inlet temperature, pressure, velocity) of coolant.

- Thermal boundary conditions

The energy that comes into the system consists of two parts: volumetric heating via neutrons and normal heat flux on first wall plasma-facing surface due to radiation. The spatial distribution of heat power volumetric density in different materials is shown in Fig. 5.17, which is a function of the distance from FW. The heat flux was set to be 0.5 MW/m^2 on the FW, while as to the bend FW surface, a decreasing value according to cosine law has been imposed: $q_{\text{corner}} = q_{\text{FW}} \cdot \sin\alpha$. One of the objectives of this thermo-mechanical analysis is to figure out the maximum achievable heat flux that the component could handle without failure.

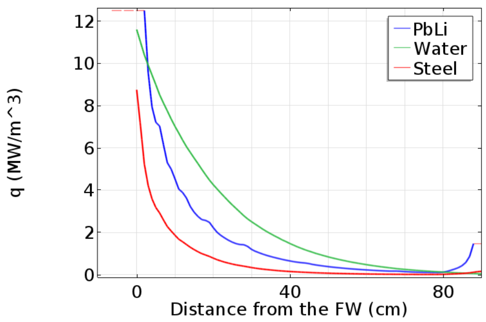

Figure 5.17: Volumetric heating of different materials

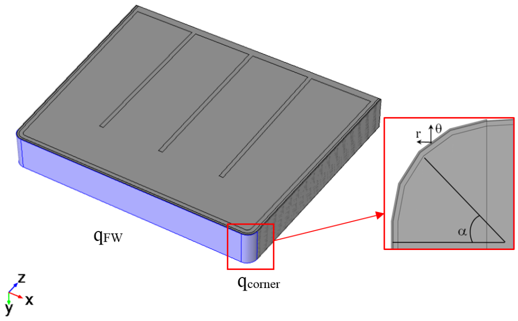

Figure 5.18: Inward heat flux

The sources of inward energy is summarized in Table 5.4.

q_{Eurofer}	q_{Eurofer}	q_{Water}	q_{FW}	q_{total}
25.9 kW	126.4 kW	7.1 kW	105.4 kW	264.7 kW

Table 5.4: Summary of volumetric and surface heat sources

As discussed in Sec. 5.2.2, there is one set of cooling channels for cooling FW and the other one embedded in the breeder. Both of them were considered as forced convective heat transfer problem in the simulation though with different approaches applied. For breeder cooling, a simplified approach was used where the cooling water flow domain has not been modeled and its thermal effect has been simulated by specifying a proper heat transfer coefficient on the breeder cooling channel internal surfaces. For breeder cooling, a different approach called conjugate heat transfer was adopted. Coolant flow domain was included in this approach.

The coolant water domains in FW structure are highlighted in purple as Fig. 5.19 shows. The CFD analysis was implemented with inlet velocity of 1.24 m/s and outlet pressure of 15.5 MPa as boundary conditions. The inlet temperature of FW channels were set to be 285 °C based on previous studies [69]. The heat removed by the water in FW can be computed by $\dot{Q} = \int C_p \dot{m}(T_{\text{out}} - T_{\text{in}}) d\Omega / V$. The obtained pressure and velocity fields could be used for conjugate heat transfer study.

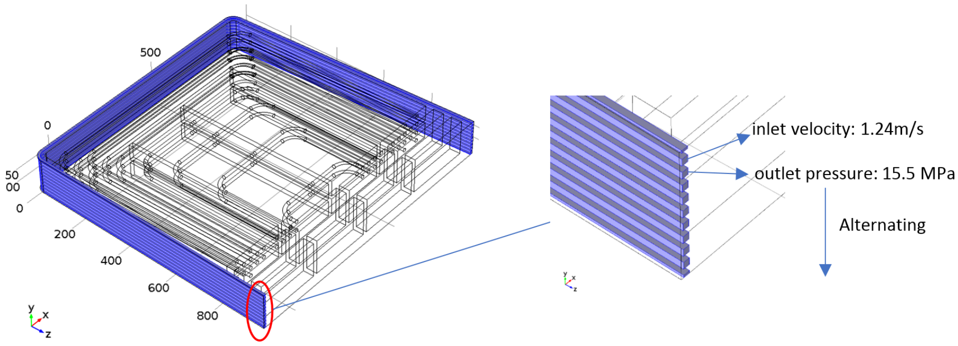

Figure 5.19: Boundary conditions of CFD analysis for FW coolant

The internal surfaces of cooling channels in the breeder are highlighted in purple as Fig. 5.20 shows. As discussed above, a simplified method which uses only an energy balance for the solid wall. The heat transfer coefficient at the fluid/solid interface is calculated with correlations. The heat removed by the breeder coolant can be computed as $\dot{Q} = \int h(T - T_{\text{bulk}}) dA$.

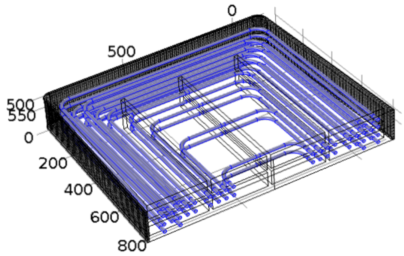

Figure 5.20: Internal surfaces of cooling channels in breeder zones

- Mechanical boundary conditions

The structural analysis starts from the elastic analysis with boundary conditions shown in Fig. 5.21. Periodic boundary conditions were applied on Face A and Face B. On the back wall, the green line was constrained to have zero radial displacement while the red line has zero toroidal displacement so that the structure was fully constrained.

Water coolant mechanical interaction with coolant channels and internal walls has been modeled by imposing a pressure of coolant obtained from thermal-hydraulic analysis to all water-wetted surfaces. Breeder mechanical interaction with module internal walls, belonging to FW, stiffening plates and back plate has been taken into account by applying a 0.5 MPa pressure along the breeder-structure interfaces. Lastly, the thermal deformation field, arising within the module as a consequence of both its thermal field and thermal expansion tensor, has been considered also.

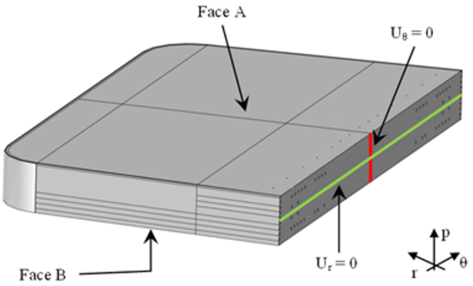

Figure 5.21: Boundary conditions for elastic analyses

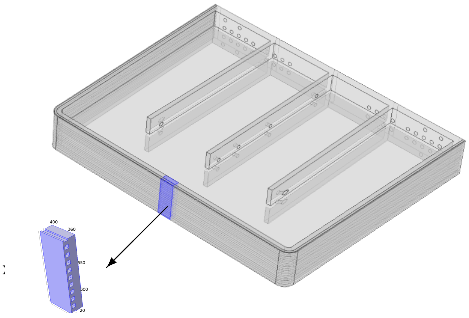

Figure 5.22: Local plastic analysis region

Following the elastic analysis, elasto-plastic analysis was implemented on a local region where highest stress was observed from elastic analysis as shown in Fig. 5.22. The displacement results obtained from global elastic analysis was used as boundary conditions for local elasto-plastic analysis.

5.2.4 Results

- Steady-state thermal-hydaulic analyses

Thermal results (Fig. 5.23) show that the maximum temperature of 534 °C is reached within the EUROFER steel structure, below its maximum allowable temperature of 550 °C, while the maximum temperature that breeder experience is 465 °C. FW coolant temperature distribution is shown in Fig. 5.24, indicating that the outlet temperature is around 345 °C after the system reaches equilibrium, giving a temperature increase of 60 °C between the inlet and outlet. The summary of thermal-hydraulic analysis results is shown in Table 5.5.

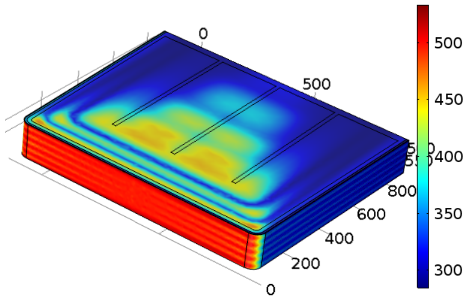

Figure 5.23: Global temperature [°C]

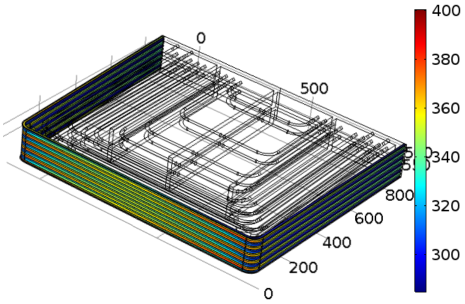

Figure 5.24: Coolant temperature [°C]

T_{max} in structure	T_{inlet}	T_{outlet}	ΔP	$q_{\text{removed\_FW}}$	$q_{\text{removed\_breeder}}$	Total q_{removed}
534 °C	285 °C	345 °C	4.8 kPa	142.4 kW	122.0 kW	264.4 kW

Table 5.5: Summary of thermal-hydraulic results

- Enhanced elasticity

Coupled thermo-mechanical steady state analyses with elastic mechanics model have been implemented to verify the current DEMO WCLL blanket design could safely withstand the thermal and mechanical loads. Three so-called ”enhanced elasticity” methods were carried out for different purposes.

Firstly, SDC-IC rules were used to verify whether the thermo-mechanical stress state complies with the prescribed requirements. Secondly, Neuber method was carried out to estimate the structure plastic behavior from elastic analyses results. Finally, to anticipate the stress state regime of structural material under combined thermal and mechanical loads with fluctuating heat flux, the Bree diagram was used.

A stress linearisation procedure was carried out to evaluate the stresses. Line integration through the thickness of the channel structure was used to resolve stresses into membrane, bending and non-linear components [70]. The line along which this integration is carried out is defined as a ”supporting line segment”. Proper supporting line segments have been identified at the locations where high stresses and high temperatures locate, as shown in Fig. 5.26, since high temperatures could result in lower maximum allowable stress intensities.

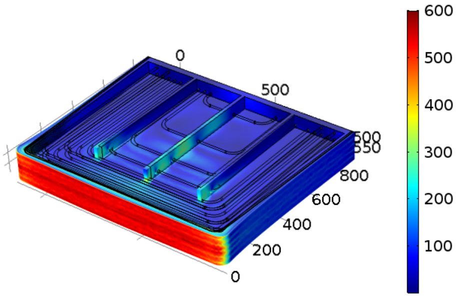

Figure 5.25: Von mises stress, elastic analysis [MPa]

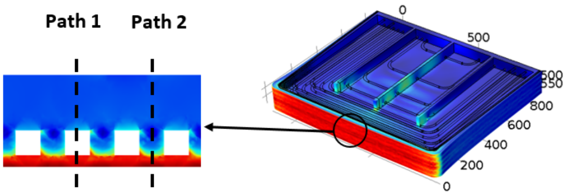

Figure 5.26: Critical supporting line segments

Factors of safety were determined based on the three different allowable values and low temperature design criteria, as shown in Table 5.6. The three design rules were used to prevent failure by plastic instability, cracking due to plastic flow localization and local fracture due to embrittlement, respectively [71].

	Plastic instability limit	Plastic flow localization limit	Ductility exhaustion limit
Path	$1.5S_m/\overline{P_L + P_b}$	$S_e/\overline{P_L + Q}$	$S_d/\overline{P_L + P_b + Q}$
1	11.52	1.07	1.36
2	8.76	1.22	1.71

Table 5.6: Factors of safety based on SDC-IC criteria

One of the objectives of durability analysis is to predict the magnitudes of the local cyclic stresses and strains experienced at the hot-spot of the components subjected to fatigue loading. It is necessary to translate the elastic calculated stress at the critical locations into estimates of elastic-plastic stress and strain behavior. One of the most popularly used methods is the Neuber plasticity correction [38]. The advantage of this Neuber method is that equivalent plasticity information could be obtained without implementing plastic analysis.

The blue curve in Fig. 5.27 is the stress-strain curve of EUROFER at 450 °C [72]. In the simulation, the stress-strain relation was identified as a function of temperature. The elastic analyses results fall on the red dotted line and the strain energy density can be computed from $W_s = \frac{1}{2}\sigma_{ij}\epsilon_{ij}$. Then the point on elasto-plastic stress-strain curve was found to give the same energy product W_s, as the intersection point of blue and green curve in Fig. 5.27 shows. The point was then considered as the equivalent Neuber stress and strain and will be compared to the following elaso-plastic analyses results.

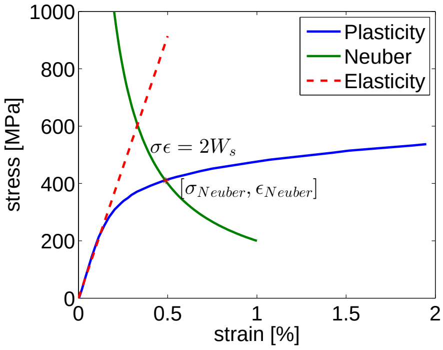

Figure 5.27: Stress-strain curve with Neuber Hyperbola

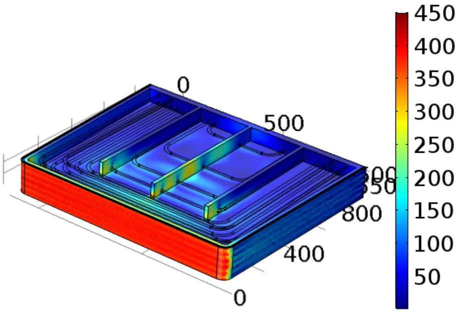

Figure 5.28: Equivalent Neuber stress [MPa]

Fig. 5.28 shows the Von mises stress distribution after applying the Neuber method to the entire steel structure domain. It can be observed that the equivalent Neuber stresses are lower than the elastic stresses due to hardening by comparing Fig. 5.25 to Fig. 5.28.

Both of the previous two enhanced elasticity methods capture the material behavior at the steady state. In the real application, the reactor will start up and shut down for several cycles, leading to a cyclic applied heat flux or thermal loads. Since the plastic strains are irreversible, residual stresses are produced in the material when the reactor is shut down and in turn may cause further plastic flow. This behavior gives rise to two possible modes of failure — ratcheting and plastic cycling. Ratcheting means plastic strains are produced during each thermal load cycle and have a cumulative effect which causes progressive growth of the ratcheting, while there is no net growth of the plastic strains during each thermal cycle. Since ratcheting is a more severe regime and can ultimately lead to rupture, it is necessary to figure out the loading conditions which enable ratcheting to occur so that we are able to avoid it. Although plastic cycling is less severe, the repeated plastic strains can ultimately cause fatigue cracking. It is therefore desirable to know when plastic cycling occurs and estimate the range of variation of the plastic strain, which is necessary for determining the number of cycles to failure.

When the heat flux is fluctuating, the combination of thermal and mechanical (pressure) stress can lead to an elastic stress state, a cyclic plastic stress state, shakedown stress state or a ratchet stress state where the structure will continually grow in size and its thickness reduced gradually till rupture. The ASME design code limits on these failure phenomenon are due to the work of Bree [39]. The six different regimes based on the Bree analysis and used in the ASME Design Code are shown in Fig. 3.7.

As Fig. 3.7 shows, the type of the stress state regime under the combined thermal and mechanical loads is determined by the equivalent pressure stress σ_p and maximum value of thermal stress σ_t. Both σ_p and σ_t were estimated based on the elastic analyses results. It turned out that cyclic plasticity was anticipated since $\sigma_t > 2\sigma_y$ and $\sigma_p \sigma_t < \sigma_y^2$. This conclusion will be further verified by transient elasto-plastic analyses under cyclic loading.

- Elasto-plasticity

A global-local elasto-plastic analysis method was discussed in Sec. 2.3 is implemented in this section. First, we use the global-local analysis to determine the stress distributions during steady-state loading. The method also provides the basis for cyclic loading analysis.

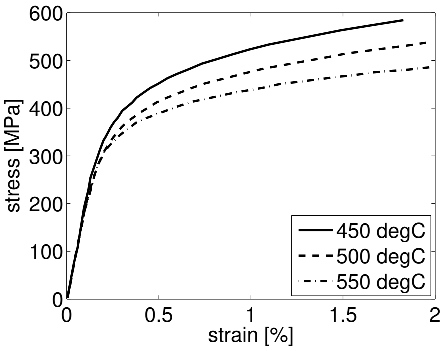

Figure 5.29: Stress-strain curves for Eurofer97 at different temperatures [3]

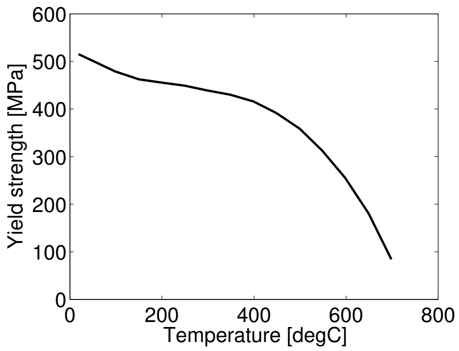

Figure 5.30: Yield strength values for Eurofer97 at different temperatures

Fig. 5.29 shows the stress-strain data at different temperatures used in the global-local elastoplasticity model. Together with the yield strength of Eurofer97 as a function of temperature as shown in Fig. 5.30, temperature-dependent elasto-plastic stress-strain curves were used in a global-local simulations.

A global elasto-plastic analysis was firstly performed as shown in Fig. 5.31. However, due to the complexity of geometry and multiphysics problem, performing elasto-plastic analysis over the entire domain is time-consuming and is not suitable for the following transient analysis under cyclic loading where elasto-plastic analysis needs to be performed for many times. Therefore, a more efficient global-local analysis discussed in Sec. 2.3 was performed alternatively and the obtained results as shown in Fig. 5.32 could be compared to the global elasto-plastic analysis results for proving its accuracy. So far, we have stress results from four different models — global elasticity (Fig. 5.25), Neuber method (Fig. 5.27), global plasticity (Fig. 5.31) and global-local method (Fig. 5.32). It can be seen that the peak stresses obtained from the three models which consider the plastic behavior are much lower than the pure elastic one, but are slightly different from each other. The peak Von-Mises stress computed from the global-local analysis (≈425 MPa) is closer to the global plasticity result (≈410 MPa) than the one from the Neuber method (≈450 MPa).

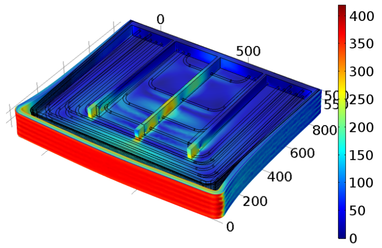

Figure 5.31: Von-Mises stress distribution from global plastic analysis [MPa]

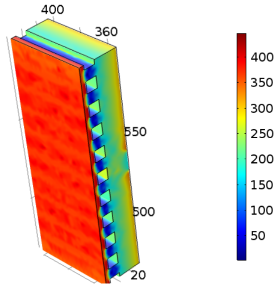

Figure 5.32: Von-Mises stress distribution from global-local analysis [MPa]

As discussed in Sec. 5.2.2 and Sec. 5.2.3, quasi-static elasto-plastic analyses under cyclic thermal loading were conducted within a multiscale framework. Based on the elastic analyses results, a local domain within the high stress region near the FW was selected for the local elasto-plastic analyses. Fig. 5.33 shows plasma current (MA) temporal profile during pulsed operation of DEMO, giving an on-time of 7000 seconds, and a total pulse time of 7200 seconds. The surface heat flux on the first wall was assumed to be proportional to the plasma current, with a magnitude of 0.8 MW/m^2. A region on the FW was selected to plot the stress-strain curve during two cycles of the transient heat loading. No significant strain accumulation was observed after two cycles, as can be seen in Figure 5.34. We thus conclude that the first wall structure will not experience ratcheting of plastic strain, but will rather have repeated and finite amplitudes of plastic strains, on the order of 0.0014 in each cycle. This matches the anticipation of the Bree diagram method, which predicts that the structure will be in the plastic regime rather than in a shakedown or ratcheting regimes.

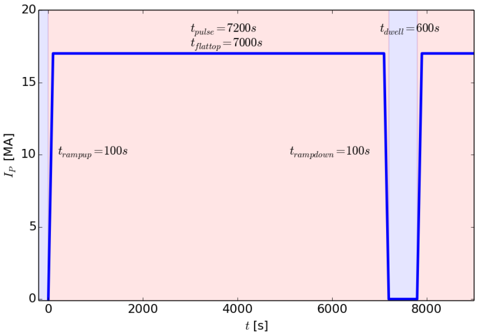

Figure 5.33: Heat pulse duration in DEMO

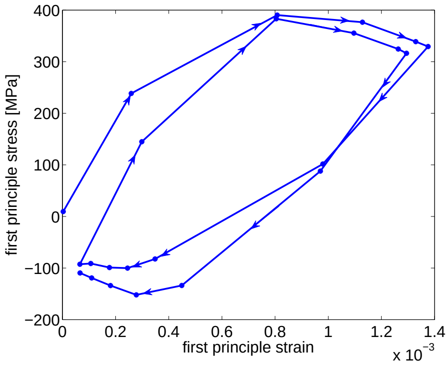

Figure 5.34: Stress-strain curve during two loading cycles

- Fracture analyses with MS-FAD method

Due to the limited fracture toughness of EUROFER 97 at low temperature, it's necessary to carry out the fracture analyses at the location where the combination of relative low temperature and high stress occurs. An advanced fracture mechanics concept based on the Material-Specific Failure Assessment Diagram (MS-FAD) was implemented and introduced in this section.

As Fig. 5.35 shows, the crack was assumed to be initiated at the bending corner of the FW structure where the temperature is below 350 °C and the stresses are relatively high. MS-FAD method requires computing the J-integral based on the elasto-plastic material model. For simplicity, the MS-FAD method was implemented on the 2D cross section with two J-integral contours.

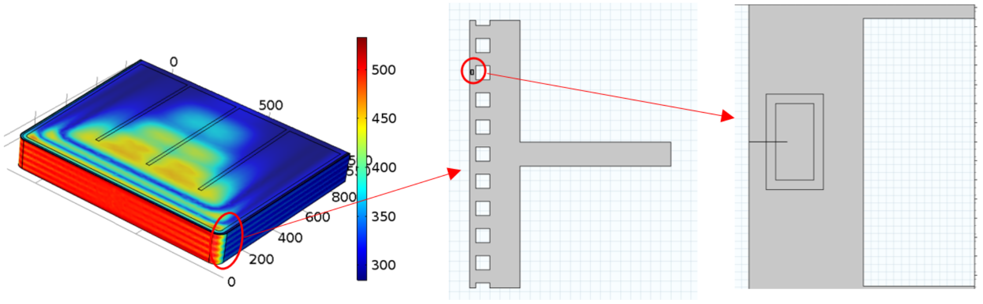

Figure 5.35: Crack at FW corner with contours

To begin the reference stress calculation for the crack, both the elastic portion of the total elasto-plastic J-integral results and elasto-plastic J-integral were computed, based on the elastic material model and elasto-plastic stress-strain curve of EUROFER respectively. $J_{\text{tot}}/J_{\text{elastic}}$ is plotted in Fig. 5.37 and used to determine the values of brittle fracture ratio K_r on the MS-FAD curve: $K_r = \sqrt{J_{\text{elastic}}/J_{\text{tot}}}$.

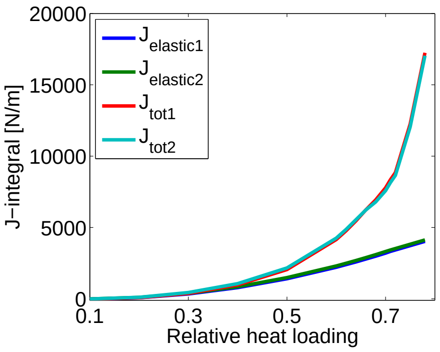

Figure 5.36: Elastic and total J-integrals

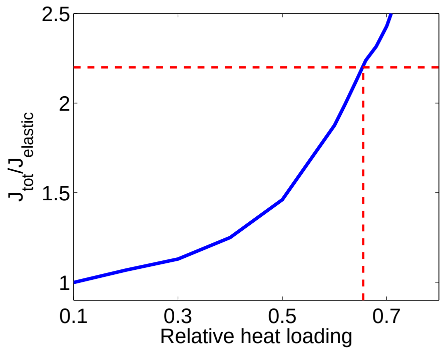

Figure 5.37: J-integral ratio

The other ratio on the MS-FAD is the plastic collapse ratio L_r, which can be calculated as $L_r = \sigma_{ref}/S_y$, where S_y is the yield strength and σ_{ref} is the reference stress. The MS-FAD curve can thus be generated specifically for Eurofer by plotting K_r versus L_r, as shown in Fig. 5.39. To evaluate the diagram, a crack is assumed to be located at the corner, and the the corresponding values of $K_r = K/K_c$ and $L_r = \sigma_{ref}/S_y$ are computed and plotted in Fig. 5.39.

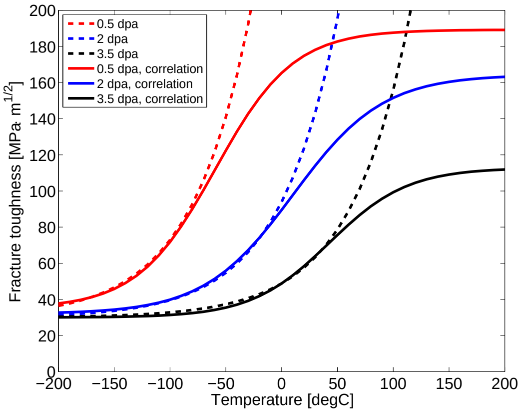

Figure 5.38: Fracture toughness of EUROFER97

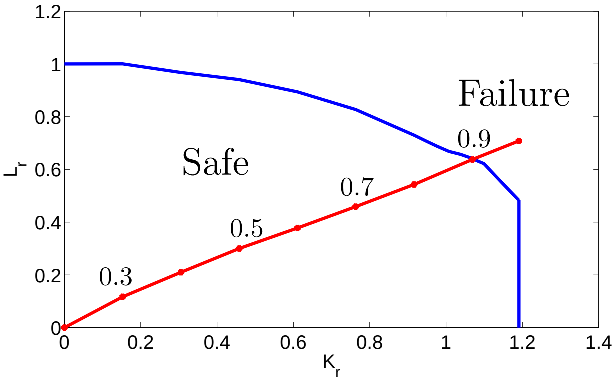

Figure 5.39: MS-FAD fracture analysis for the Eurofer 97 FW. The thermal load line is shown, where the surface heat flux is gradually increased, and the safetu factor computed for each value of the heat flux.

To evaluate the crack assumed to be located at the corner, the corresponding values of $K_r = K/K_c$ and $L_r = \sigma_{\text{ref}}/S_y$ were computed and plotted on Fig. 5.39. The safety factor is computed for each value of the applied heat flux as the ratio of the K_r at the intersection between the load line and the FAD line to the value of K_r at the applied heat flux. It can be seen that the safety factor is around 1.16 at a surface heat flux of 0.8 MW/m^2. This value corresponds to a fracture toughness of around 100 MPa$\sqrt{(}m)$ at the operating tomepratures, evaluated from the irradiation data at 3.5 dpa.

5.3 Tungsten monoblock concepts for the FNSF first wall and divertor

The objective of the work in this section is to maximize the heat flux capability of a He-cooled monoblock to provide high performance solutions for both first wall and divertor applications.

5.3.1 Background of Monoblock Concept

Next-step fusion nuclear devices require plasma-facing components that can survive a much higher neutron dose than ITER, and in many design concepts also require higher operating temperatures, higher reliability, and materials with more attractive safety and environmental characteristics. In search of first wall concepts that can withstand surface heat fluxes beyond 2 MW/m^2, we analyzed advanced monoblock designs using coolants and materials that offer more attractive long-term performance. These use tungsten armor and heat sinks, similar to previous designs, but replace the coolant with helium and the coolant containment pipe with either low-activation ferritic-martensitic steel or SiC/SiC composite.

The monoblock concept provides the possibility of higher heat flux capability, in part due to the spreading of heat over a larger coolant surface area. Fig. 5.40 shows an example of a monoblock cooling channel to be used in ITER, including an internal swirl tube to enhance heat transfer in water. The high-conductivity W blocks conduct heat deeper into the wall, utilizing the sides of the cooling channels as well as the front surface. The initial goal of the present study was roughly a doubling of the achievable heat flux, to the range of 4 MW/m^2, primarily by finding an optimum geometry that allows heat to penetrate into the largest possible cooling channel area.

Two geometric variations were considered: a circular pipe similar to the ITER divertor monoblock or an elongated rectangular duct, similar to a microchannel array. The analysis is performed parametrically in order to determine the optimum design details. Variables include physical properties, geometric dimensions and coolant conditions. The method and results are presented in Section 5.3.3 and 5.3.4.

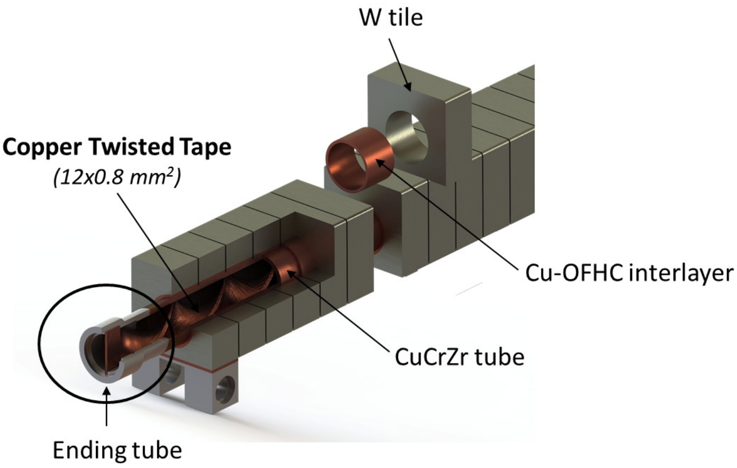

Figure 5.40: ITER monoblock divertor

In this article we consider several variations of advanced monoblock designs, which are described in Sec. 5.3.2. All of the design variations use pure W blocks and He coolant. Water has been avoided for long-term commercial applications due to several issues related to performance, safety and the minimum operating temperature requirement of steel [73]. The containment pipe is either low activation ferritic steel (both conventional ferritic/martensitic and more advanced high-temperature steels were considered) or SiC/SiC composite. With recent advances in the application of SiC composites for both fission [74, 75, 76] and fusion [77], we considered the use of SiC/SiC as a credible He coolant containment pipe in a time frame consistent with the likely implementation of FNSF within the US.

The results of analysis show that helium-cooled steel can remove up to 5 MW/m^2 of steady-state surface heat flux and helium-cooled SiC/SiC can remove nearly 10 MW/m^2 while satisfying all materials and design requirements. This suggests that a He-cooled W/SiC monoblock could withstand divertor-like heat fluxes.

5.3.2 Design concept

- Materials and properties

A typical monoblock design consists of four types of materials with different functions: 1) a plasma facing material (or armor) resistant to plasma interactions, 2) a high conductivity heat sink material, 3) a structural (or pressure vessel) material to contain the coolant and provide mechanical strength, 4) interlayer materials between the pressure vessel and heat sink to provide acceptable heat transfer and structural integrity.

Similar to ITER and some Demo designs, we adopted tungsten as our preferred plasma-facing material. Its high thermal conductivity allows it to fulfill the role of heat sink as well. Its advantages include its refractory nature, low plasma sputtering rate, high strength, high thermal conductivity and acceptable neutron activation, while its brittleness is the main drawback that impacts its use as a candidate structural material [78]. The maximum allowable temperature of 1300 °C is determined by recrystallization and loss of creep strength. The lower bound to maintain ductility under irradiation is uncertain, but probably in the range of 700–800 °C. In the steel monoblock designs we examined, it is not possible to maintain the armor above the ductile-to-brittle transition temperature, so no lower limit was imposed. Although the armor serves no structural or pressure vessel functions, still it must exhibit sufficient crack resistance to allow efficient heat transfer and to prevent spallation of material into the vacuum chamber. Uncertainties remain in the use of tungsten as an armor, but a substantial R&D program is underway to validate the material in ITER and Demo environments [79].

The structural material is a critical part of the design, since it has a structural and pressure containing function as well as the requirement to conduct heat efficiently into the coolant channels. For a water-cooled divertor, low-activation ferritic/martensitic (FM) steel (such as Eurofer) and CuCrZr have been studied as the coolant containment pipe materials [80, 78]. According to [78], the operating temperature window of Eurofer is from 325 to 550 °C. Again, the upper temperature is limited by creep strength. More advanced high-temperature steels (such as ODS steels) can raise the upper limit to 650 °C. The conventional assumption of the lower limit of FM steels is 350 °C. However, post-irradiation annealing of defects will result in a residual shift in DBTT of only 48 °C [81]. It provides the possibility to use Eurofer at a lower temperature, like 325 °C.

Besides low-activation ferritic steels, SiC/SiC composite was also considered as a candidate for the He coolant containment pipe. SiC/SiC composites have been under development as a high temperature structural material for both fission and fusion applications. Its operating temperature window was assumed to be from 400 °C to 1000 °C. The upper limit is determined by void swelling considerations while the lower limit is due to thermal conductivity degradation concerns. Other thermo-mechanical properties for the simulation were obtained from [76, 77].

Major material properties of coolant containment pipe materials (low-activation ferritic steels and SiC/SiC composite) and plasma facing component material (tungsten) used in the FE model are summarized in Table 5.7. Most of properties are temperature-dependent. But for those with only minor changes when the temperature varies within the operating temperature window, the average values were used in simulations. For SiC composites, the effect of neutron radiation on thermal conductivity was taken into account.

	Thermal conductivity [W/mK]	Thermal expansion coefficient [10^{-6} K^{-1}]	Heat capacity [J/kgK]	Youngs Modulus [GPa]	Operating temperature [°C]
Steel	26 [17]	10 [17]	550 [17]	210 [17]	325 – 550/650 [14]
SiC/SiC	158 [13] (500 – 1000 °C)	45 [13] (400 – 1000 °C)	1070 – 1260 [13]	200 [13]	400 – 1000 [18]
Tungsten	145 – 113 [19] (RT1000 °C)	4.5 [19]	148 [19]	360 — 240 [19] (RT – 1000 °C)	500 – 1300 [7]

Table 5.7: Summary of material properties

At the level of preliminary design, only low temperature design rules, without considering creep and fatigue interaction, were applied. Thus the $3S_m$ rule was used to check for failure. For the low-activation ferritic steels, the allowable stress intensity ($3S_m$) is around 450 MPa [82] (with minor variations with respect to temperature change) at the operating temperature. The stress limits of SiC/SiC were discussed in the ARIES-I study; recommended maximum primary and secondary stress limits were 140 MPa and 190 MPa respectively [83]. Since tungsten is not considered a structural material for our designs, the $3S_m$ design criteria was not applied to it. However, to prevent cracks in tungsten, we assumed that the maximum stress should be less than the ultimate tensile strength, which is strongly dependent on the temperature: 1000 MPa at 500 °C and 600 MPa at 1000 °C [80].

- Configurations

A circular pipe is commonly used in divertor monoblock designs (like those for ITER and DEMO). Besides this conventional design, an elongated rectangular duct with rounded corner, similar to a microchannel heat sink, was also considered in this study. Microchannel arrays have been shown to offer solutions to thermal dissipation problems, such as cooling of microelectronics. By comparing the results of these two configurations, the added performance of the slotted duct geometry was clearly shown in Sec. 5.3.4. Both of these geometries are depicted in Fig. 5.41. Models in the simulation were in 3D with a thickness of 4 mm in the axial direction.

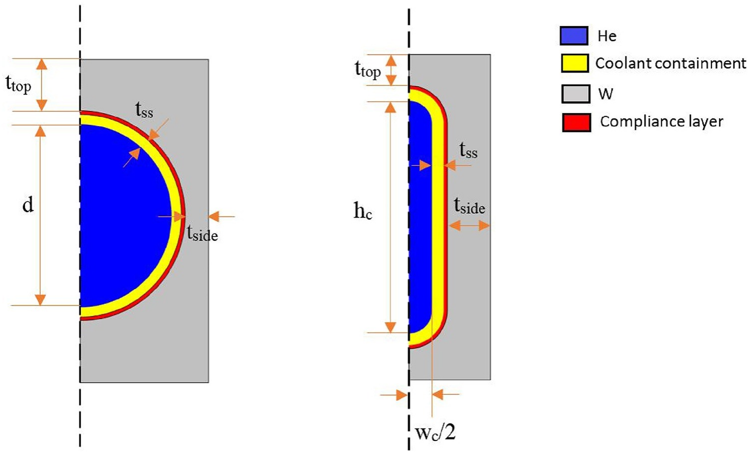

(a) circular pipe (b) Elongated rectangular pipe

Figure 5.41: Concept geometry and adjustable geometric parameters

Circular pipe		Elongated rectangular pipe	
Parameter	Range (mm)	Parameter	Range (mm)
t_{top}	2-10	t_{top}	1-6
t_{side}	2-6	t_{side}	1-6
d	8-12	w_c	1-5
t_{ss}	0.5-2	h_c	10-20
		t_{ss}	0.5-2

Table 5.8: Geometric parameter ranges for analyses.

5.3.3 Analysis

- Analysis and optimization methodology

In order to investigate the maximum heat flux that various advanced monoblock designs can handle, 3D steady state thermo-mechanical analyses have been performed based on the approach discussed in Sec. 3.1.2. For more time-efficient analyses, a symmetry boundary condition was used such that only half of the component was studied. Basically, the simulation includes two parts, which were steady state thermal analysis and thermo-mechanical elastic analysis. Detailed boundary conditions are represented in Fig. 5.42.

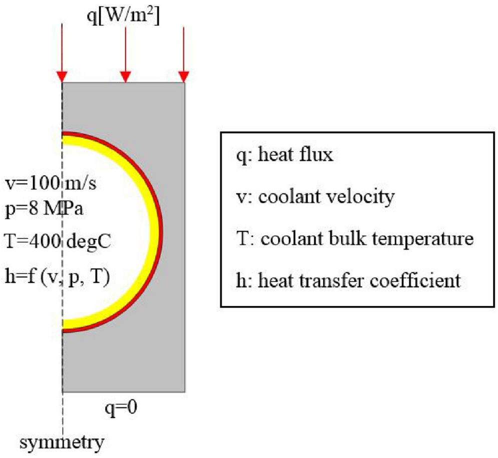

Figure 5.42: Summary of boundary conditions

A two-step optimization methodology was used to investigate the optimal design that leads to the maximum allowable heat flux. The first step is to perform a design parameter study so that the influence of each adjustable geometrical parameter on temperature and stress distributions in the monoblock component was understood. Based on the parameter study results, the best combination of different geometrical parameters, which leads to the largest design margin, was roughly determined. In the second step, an optimization module in COMSOL using the Nelder-Mead method was used to determine the optimal design that satisfies all material and design requirements. The optimization module uses the parameters determined in the first step as the initial values so that it searches for the local optimum around the initial values. Besides the initial values of adjustable parameters, three other things need to be determined in order to run the optimization module: objective function, parameter range and constraints. As discussed earlier, the objective of this optimization is to achieve the maximum allowable heat flux. Thus the objective function was set to be the heat flux loading q. Parameter ranges are listed in Table 5.8. Constraints were determined from operating temperature windows and allowable stress intensities of different materials discussed in Sec. 5.3.2. Finally, COMSOL provides the optimal results that maximize the objective function without breaking any constraint.

5.3.4 Results

Following the optimization methodology discussed above, several monoblock designs have been studied, using different materials and coolant containment geometries. Results of the different cases are compared as shown in Fig. 5.43(a) - 5.43(d) and Table 5.9. Results include temperature and stress distribution in the structure. The calculated stress can be divided into two parts: the primary stress (P) induced by the mechanical loads, and the secondary stress (Q) induced by thermal loads. P + Q stands for the stress intensity of summed primary and secondary stress.

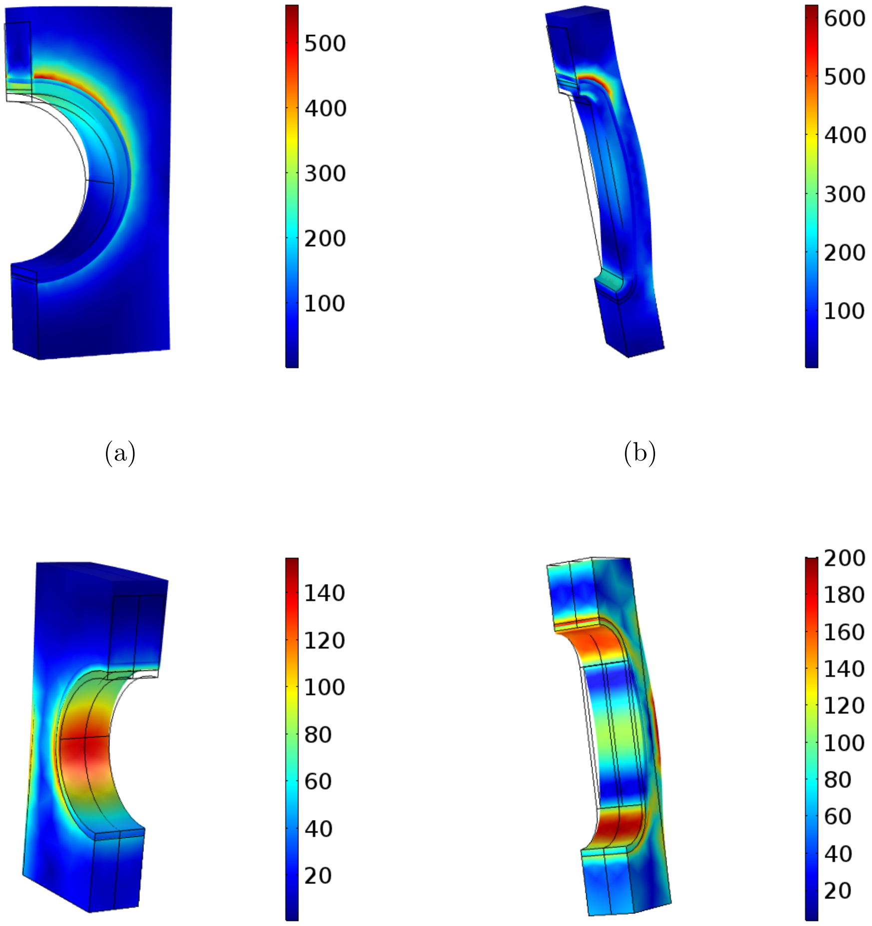

(a) (b)

(c) (d)

Figure 5.43: σ_{Von} [MPa] (a) Steel round pipe. (b) Steel slotted duct. (c) SiC/SiC round pipe. (d) SiC/SiC slotted duct.

Configuration	T_{pipemax} [°C]	T_{Wmax} [°C]	P+Q [MPa]	Allowable temperature [°C]	$3S_m$ [MPa]	Pumping power/area [kW/m^2]	Max allowable heat flux [MW/m^2]
Steel round pipe	**550**	613	396	550	450	32.8	**2.1**
ODS steel round pipe	583	640	**450**	650	450	33.0	**2.4**
Steel slotted duct	**550**	645	344	550	450	46.3	**3.7**
ODS steel slotted duct	**650**	793	358	650	450	46.6	**5.2**

Table 5.9: Summary of thermo-mechanical results for steel cases.

Configuration	T_{pipemax} [°C]	T_{Wmax} [°C]	P+Q [MPa]	Allowable temperature [°C]	$3S_m$ [MPa]	Pumping power/area [kW/m^2]	Max allowable heat flux [MW/m^2]
SiC/SiC round pipe	1000	1172	18/144	1000	140/90	29.6	**4.7**
SiC/SiC slotted duct	995	1183	**140**/98	1000	140/190	40.6	**7.6**

Table 5.10: Summary of thermo-mechanical results for SiC/SiC cases.

5.3.5 Discussion

Besides the configuration, fluid conditions, material properties and design limits also have an impact on the achievable heat flux. For the fluid conditions, higher heat transfer coefficient would help reduce the highest temperature in SiC/SiC while lower pressure will relieve the primary stress problem. For the material properties, higher thermal conductivity of tube material would help enhance the heat transfer. In addition, extending the design limit would help enlarge the design margin and thus improve the performance.

The optimum SiC/SiC slotted duct configuration was selected to show how the factors discussed above make a difference. Heat transfer enhancement methods such as roughening the cooling channel surface could help increase the heat transfer coefficient without causing additional stress problems, which will lead to a larger design margin. For the cases where Reynolds number of coolant was around 2.5×10^4, the Nusselt number can be increased to 1.7 times greater by introducing rib-roughened channel walls [84]. With this higher Nusselt number, simulation results showed that 9.4 MW/m^2 heat flux can be handled (with 8 MPa and 100 m/s coolant).

The effect of thermal conductivity of SiC/SiC composite on achievable heat flux was also studied. The results turned out that the achievable heat flux can be increased to 8.2 MW/m^2 by assuming the thermal conductivity can be increased by 10 W/(mK).

Finally, the impact of stress limits was studied. Assume that allowable primary stress could be increased to 200 MPa, then the achievable heat flux will be able to reach 8.7 MW/m^2. Thermal (secondary) stress limit doesnt affect the results since maximum thermal stress is far below the allowable value as long as the temperature requirement is met.

CHAPTER 6

Conclusions

The research presented in this thesis has focused on an effort to develop a multiscale modeling approach incorporating elasticity, elasto-plasticity and crystal plasticity within a FEM multiphysics framework, specifically for designing high-heat flux components. The aim of research is to contribute to a number of areas, as follows.

1. To make recommendations for optimal multiphysics (solid mechanics, heat transfer and fluid dynamics) simulation strategies, which are especially critical for high-heat flux components and systems, by selecting suitable multiphysics coupling algorithms and solvers.

2. To develop a multiscale modeling approach that couples meso- and macro-scale material models from elasticity to crystal plasticity with a step-by-step zoom-in method. Improvements have been made in the solution of the problem of matching stress and displacements at the interface between different levels due to application of heterogeneous models in different zones.

3. To advance the science of crystal plasticity by the development of a dislocation-based crystal plasticity model with minimum fitting parameters within a large deformation framework and to validate the proposed model with experiments.

4. To apply the developed multiscale-multiphysics framework to real engineering design of critical components in fusion energy systems.

The above research objectives have been achieved and the corresponding major findings and conclusions are discussed in a number of areas.

6.1 Optimum Multiphysics Strategy for High-Heat Flux Components

Coupling between three common physics involved in high-heat flux components — computational fluid mechanics (CFD), heat transfer and structural mechanics is used to optimize the design and to produce a configuration that can be further analyzed for its structural performance. The unique aspects of coupling these three types of physics simulations were revealed. Firstly, structural mechanics is loosely coupled to both CFD and heat transfer since usually the deformation is not large enough to have significant influence on the other two physics unless contact or delamination happens. Thus structural analysis can follow fluid-thermal coupling sequentially, leading to a one-way coupling method. Secondly, fluid-thermal coupling which is more tightly coupled needs to be treated carefully and wisely. It was proved by test cases that while complete coupling between CFD and heat transfer is necessary for first wall design, such tight coupling is not warranted for interior cooling channels to the blanket structure. The main reasons for this conclusion is that first wall channels are subjected to severe one-sided heating, have square cross-sections, and bends. Standard heat transfer correlations are not adequate for first wall channels, but are assumed to be sufficient for interior blanket cooling channels that have round cross-sections and are uniformly heated.

6.2 Global-Local Models of Elasto-Plasticity

Although conventional submodeling methods have been widely used during the past few decades to improve the computational efficiency of FEM simulation, the problem of non-matching quantities such as displacement and traction at the global-local interface due to the coupling of heterogeneous constitutive models still remains not perfectly solved. Three conventional submodeling methods, named multi-grid method, local defect correction method and variational method with Lagrangian multipliers, have been reviewed and implemented on a 2D indentation problem as the test case. None of them could provide a smooth transition of stress components across the interface. To solve this problem, a new coupling method based on the Hu-Washizu variational principle method is proposed in the thesis to couple the elastic model in global domain and elato-plastic model in local domain. Thanks to the additional stress components as independent variables, stresses and displacements are able to be matched at the interface at the same time. In addition, to make one step further for crystal plasticity to capture the anisotropic material behaviors, another innovative multiscale framework has been proposed to couple the conventional plasticity model and crystal plasticity model by matching the plastic slip on the global-local interface and implemented on the indentation problem again for demonstrating its feasibility. The results showed that the proposed global-local analysis appraoch is able to match the macroscopic material behaviors from two coupled models by examining the stress-strain curves. Besides, the anisotropic material behaviors like plastic slip on each slip system can be smoothed out around the global-local interface.

6.3 Dislocation-Based Crystal Plasticity

A continuum dislocation-based crystal plasticity model within large deformation framework is proposed in the thesis, where the incompatible plastic component of deformation results from the flux of dislocations on different and interacting slips systems. Constitutive equations for the dislocation fluxes are determined from a dissipative variational principle given two thermodynamic potentials. Solution to the self-consistent continuum formulation was found using the finite element method. In particular, computer simulations were performed for cases that mimic the experimental conditions used in wedge micro-indentation experiments of fcc Ni. A comparison of overall dislocation density distribution and macroscopic mechanical response is presented and shows a satisfactory fit. Both lattice rotation and Nye tensor information match the experimental results qualitatively and quantitatively. The 4 sectors of lattice rotation with alternating sign are clearly observed from simulation results. Besides, the distribution of scalar densities on each slip system is computed from both convection equation for dislocation densities and "low bound" estimation method proposed by

Kysar *et. al* [2]. The proposed model is able to reproduce the dislocation microstructure measured in the wedge micro-indentation experiment with minimum number of fitting or phenomenological parameters.

6.4 Design Applications of the Methodology

The proposed multiscale-multiphysics framework for the simulation-based design of high heat flux components has been applied on three components used in the fusion power plant, which are FW/Blanket of FNSF and EUROfusion DEMO fusion power plant and monoblock concept for the divertor.

Firstly, the FNSF FW/Blanket is used as an example to demonstrate how to select the suitable multiphysics strategies for the high heat flux component with cooling systems. Based on the thermal-hydraulic simulation results, the elastic structural analysis is performed with the SDC-IC design criteria applied, demonstrating that the current design can withstand the steady-state combined thermal and mechanical loads.

Furthermore, based on the successful implementation of multiphyisics modeling of FNSF FW/Blanket, a more comprehensive multiphysics-multiscale simulation approach is applied for the EUROfusion DEMO FW/Blanket design. Besides applying SDC-IC criteria, another two enhanced elastic analysis approaches which are based on Neuber method and Bree diagram have been performed to approximately estimate the material plastic behavior under steady-state and cyclic loading respectively. A more precise multiscale method is developed and applied to the optimized design as the final stage of verification. In this method, the global elastic solution is coupled to a local analysis of a small section of the FW that was determined to be critical. The coupling ensures that tractions and displacements are continuous across the global-local boundary via a variational principle. Calculations of the local elasto-plasticity, coupled with global elasticity of the entire structure showed that ratcheting will not take place as the structure is cycled. The result is in agreement with the simplified Bree analysis, but gives a value of the reversed plastic strain amplitude on the order of 0.0014 that must be considered for further fatigue analysis. The potential for fracture is addressed with the method of Failure Assessment Diagram (FAD). The method requires material specific calculations of the elastic J-integral alone, and the elasto-plastic J-integral of Eurofer. The ratio of the two is used to determine a relative brittle fracture index, K_r. Also, a plastic collapse ratio is obtained from the values of stress in the structure and the yield strength of Eurofer. A region of "safe" design was established for various applied levels of FW heat flux. It is shown that the factor of safety against fracture of the FW in the WCLL design is around 1.16 for a heat flux of 0.8 MW/m^2 at a neutron damage dose of 3.5 dpa. This is a low fluence, and reduced values of the heat flux may be required for longer structural lifetime.

The third design application — tungsten monoblock concept for FW/divertor is presented to show how to perform the design optimization based on the simulation results. By varying the material, structural configuration and geometric parameters, the optimized design is achieved aiming for withstanding the maximum allowable heat flux. The results of analysis show that helium-cooled steel can remove up to 5 MW/m^2 of steady-state surface heat flux and helium-cooled SiC/SiC can remove nearly 10 MW/m^2 while satisfying all materials and design requirements. This suggests that a He-cooled W/SiC monoblock could withstand divertor-like heat fluxes.

In the present research, we have proposed a multiphysics-multiscale FEM simulation framework especially applicable for high heat flux/temperature components. The feasibility and advantages of the proposed simulation approach have been demonstrated by three real-world design applications. In addition, an advanced dislocation-based crystal plasticity model has been proposed and validated by indentation experiment, which could provide more precise results for simulation-based design and failure analysis by capturing the material micro-structure. Future work can be incorporating the discrete dislocation dynamics models into the current continuum multiscale modeling framework.

REFERENCES

[1] Oliver Kraft, Patric A Gruber, Reiner Mönig, and Daniel Weygand. Plasticity in confined dimensions. *Annual review of materials research*, 40:293–317, 2010.

[2] J.W. Kysar, Y. Saito, M.S. Oztop, D. Lee, and W.T. Huh. Experimental lower bounds on geometrically necessary dislocation density. *International Journal of Plasticity*, 26(8):1097–1123, aug 2010.

[3] Ferenc Gillemot. *Material Property Handbook on EUROFUER 97.* EUROfusion, February 2012.

[4] LE Shilkrot, RE Miller, and WA Curtin. Coupled atomistic and discrete dislocation plasticity. *Physical review letters*, 89(2):025501, 2002.

[5] Ronald E Miller, LE Shilkrot, and William A Curtin. A coupled atomistics and discrete dislocation plasticity simulation of nanoindentation into single crystal thin films. *Acta Materialia*, 52(2):271–284, 2004.

[6] Mathias Wallin, WA Curtin, Matti Ristinmaa, and Alan Needleman. Multi-scale plasticity modeling: Coupled discrete dislocation and continuum crystal plasticity. *Journal of the Mechanics and Physics of Solids*, 56(11):3167–3180, 2008.

[7] O Jamond, R Gatti, A Roos, and B Devincre. Consistent formulation for the discrete-continuous model: Improving complex dislocation dynamics simulations. *International Journal of Plasticity*, 80:19–37, 2016.

[8] David Rivera, Yue Huang, Giacomo Po, and Nasr M Ghoniem. A dislocation-based crystal viscoplasticity model with application to micro-engineered plasma-facing materials. *Journal of Nuclear Materials*, 485:231–242, 2017.

[9] Y Huang, MS Tillack, NM Ghoniem, JP Blanchard, LA El-Guebaly, and CE Kessel. Multiphysics modeling of the fw/blanket of the us fusion nuclear science facility (fnsf). *Fusion Engineering and Design*, 2017.

[10] CE Kessel, JP Blanchard, A Davis, L El-Guebaly, LM Garrison, NM Ghoniem, PW Humrickhouse, Y Huang, Y Katoh, A Khodak, et al. Overview of the fusion nuclear science facility, a credible break-in step on the path to fusion energy. *Fusion Engineering and Design*, 2017.

[11] Y Huang, MS Tillack, and NM Ghoniem. Tungsten monoblock concepts for the fusion nuclear science facility (fnsf) first wall and divertor. *Fusion Engineering and Design*, 2017.

[12] G. Po, Y Huang, and N.M. Ghoniem. A continuum dislocation model of wedge microindentation of ductile metals. *Journla of the Mechanics and Physics of Solids*, submitted, 2018.

[13] Patrick R Amestoy, Ian S Duff, and J-Y L'Excellent. Mumps multifrontal massively parallel solver version 2.0. 1998.

[14] Olaf Schenk and Klaus Gärtner. Solving unsymmetric sparse systems of linear equations with pardiso. *Future Generation Computer Systems*, 20(3):475–487, 2004.

[15] Nicholas IM Gould, Jennifer A Scott, and Yifan Hu. A numerical evaluation of sparse direct solvers for the solution of large sparse symmetric linear systems of equations. *ACM Transactions on Mathematical Software (TOMS)*, 33(2):10, 2007.

[16] Iain S Duff, Albert Maurice Erisman, and John Ker Reid. *Direct methods for sparse matrices*. Oxford University Press, 2017.

[17] Magnus Rudolph Hestenes and Eduard Stiefel. *Methods of conjugate gradients for solving linear systems*, volume 49. NBS, 1952.

[18] Carl T Kelley. *Iterative methods for optimization*, volume 18. Siam, 1999.

[19] David E Keyes, Lois C McInnes, Carol Woodward, William Gropp, Eric Myra, Michael Pernice, John Bell, Jed Brown, Alain Clo, Jeffrey Connors, et al. Multiphysics simulations challenges and opportunities. *International Journal of High Performance Computing Applications*, 27(1):4–83, 2013.

[20] Theodore L Bergman and Frank P Incropera. *Fundamentals of heat and mass transfer*. John Wiley & Sons, 2011.

[21] Javier Bonet and Richard D Wood. *Nonlinear continuum mechanics for finite element analysis*. Cambridge university press, 1997.

[22] Raymond W Ogden. *Non-linear elastic deformations*. Courier Corporation, 1997.

[23] Philippe G Ciarlet. Mathematical elasticity. vol. i, volume 20 of studies in mathematics and its applications, 1988.

[24] CT Sun and KM Mao. A global-local finite element method suitable for parallel computations. *Computers & structures*, 29(2):309–315, 1988.

[25] CT Sun and KM Mao. Elastic-plastic crack analysis using a global-local approach on a parallel computer. *Computers & Structures*, 30(1-2):395–401, 1988.

[26] K. M. Mao and C. T. Sun. A refined global-local finite element analysis method. *International Journal for Numerical Methods in Engineering*, 32(1):29–43, jul 1991.

[27] Wolfgang Hackbusch. *Multi-grid methods and applications*, volume 4. Springer Science & Business Media, 2013.

[28] K. C. Park and Carlos A. Felippa. A variational principle for the formulation of partitioned structural systems. *International Journal for Numerical Methods in Engineering*, 47(1-3):395–418, jan 2000.

[29] K Washizu. Variational methods in elasticity and plasticity, pergamon press, 1982.

[30] J-H He. Generalized hellinger-reissner principle. *Journal of applied mechanics*, 67(2):326–331, 2000.

[31] FPE Dunne, AJ Wilkinson, and R Allen. Experimental and computational studies of low cycle fatigue crack nucleation in a polycrystal. *International Journal of Plasticity*, 23(2):273–295, 2007.

[32] M Baitsch, KC Le, and TM Tran. Dislocation structure during microindentation. *International Journal of Engineering Science*, 94:195–211, 2015.

[33] Victor L Berdichevsky. Continuum theory of dislocations revisited. *Continuum Mechanics and Thermodynamics*, 18(3-4):195, 2006.

[34] M Ilić, G Messemer, K Zinn, R Meyder, S Kecskes, and B Kiss. Experimental and numerical investigations of heat transfer in the first wall of helium-cooled-pebble-bed test blanket modulepart 2: Presentation of results. *Fusion Engineering and Design*, 90:37–46, 2015.

[35] PA Di Maio, P Arena, J Aubert, G Bongiovì, P Chiovaro, R Giammusso, A Li Puma, and A Tincani. Analysis of the thermo-mechanical behaviour of the demo water-cooled lithium lead breeding blanket module under normal operation steady state conditions. *Fusion Engineering and Design*, 98:1737–1740, 2015.

[36] ASME Boiler and Pressure Vessel Code. Section viii division 1. *UG-126 Pressure Relief Valves to UG-129 Marking, ASME International, New York*, 2010.

[37] ITER SDC-IC. Structural design criteria for iter in-vessel components. *ITER Document*, (G74), 2004.

[38] Heinz Neuber. Theory of stress concentration for shear-strained prismatical bodies with arbitrary nonlinear stress-strain law. *Journal of Applied Mechanics*, 28(4):544–550, 1961.

[39] J Bree. Elastic-plastic behaviour of thin tubes subjected to internal pressure and intermittent high-heat fluxes with application to fast-nuclear-reactor fuel elements. *Journal of Strain Analysis*, 2(3):226–238, jul 1967.

[40] Geoffrey Ingram Taylor. The mechanism of plastic deformation of crystals. part i. theoretical. *Proceedings of the Royal Society of London. Series A, Containing Papers of a Mathematical and Physical Character*, 145(855):362–387, 1934.

[41] D Peirce, RJ Asaro, and A Needleman. An analysis of nonuniform and localized deformation in ductile single crystals. *Acta metallurgica*, 30(6):1087–1119, 1982.

[42] Robert J Asaro and JR Rice. Strain localization in ductile single crystals. *Journal of the Mechanics and Physics of Solids*, 25(5):309–338, 1977.

[43] JF Nye. Some geometrical relations in dislocated crystals. *Acta metallurgica*, 1(2):153–162, 1953.

[44] James R Rice. Inelastic constitutive relations for solids: an internal-variable theory and its application to metal plasticity. *Journal of the Mechanics and Physics of Solids*, 19(6):433–455, 1971.

[45] UF Kocks. Laws for work-hardening and low-temperature creep. *Journal of engineering materials and technology*, 98(1):76–85, 1976.

[46] R Becker. Analysis of texture evolution in channel die compressioni. effects of grain interaction. *Acta metallurgica et materialia*, 39(6):1211–1230, 1991.

[47] A. Ma, F. Roters, and D. Raabe. A dislocation density based constitutive model for crystal plasticity FEM including geometrically necessary dislocations. *Acta Materialia*, 54(8):2169–2179, may 2006.

[48] Athanasios Arsenlis and David M Parks. Modeling the evolution of crystallographic dislocation density in crystal plasticity. *Journal of the Mechanics and Physics of Solids*, 50(9):1979–2009, 2002.

[49] E Orowan. Problems of plastic gliding. *Proceedings of the Physical Society*, 52(1):8, 1940.

[50] W Sylwestrowicz and EO Hall. The deformation and ageing of mild steel. *Proceedings of the Physical Society. Section B*, 64(6):495, 1951.

[51] H Mecking and UF Kocks. Kinetics of flow and strain-hardening. *Acta Metallurgica*, 29(11):1865–1875, 1981.

[52] I.J. Beyerlein and C.N. Tomé. A dislocation-based constitutive law for pure zr including temperature effects. *International Journal of Plasticity*, 24(5):867–895, may 2008.

[53] David L Holt. Dislocation cell formation in metals. *Journal of Applied Physics*, 41(8):3197–3201, 1970.

[54] Nasr Mostafa Ghoniem, JR Matthews, and Robert John Amodeo. *A dislocation model for creep in engineering materials.* Institute of Plasma and Fusion Research, University of California, Los Angeles, 1989.

[55] SL Robinson and OD Sherby. Mechanical behavior of polycrystalline tungsten at elevated temperature. *Acta Metallurgica*, 17(2):109–125, 1969.

[56] Peter L Raffo. Yielding and fracture in tungsten and tungsten-rhenium alloys. *Journal of the Less Common Metals*, 17(2):133–149, 1969.

[57] A Arsenlis, DM Parks, R Becker, and Vasily Bulatov. On the evolution of crystallographic dislocation density in non-homogeneously deforming crystals. *J Mech Phys Solids*, 52(6):1213–1246, 2004.

[58] F. Roters, P. Eisenlohr, L. Hantcherli, D.D. Tjahjanto, T.R. Bieler, and D. Raabe. Overview of constitutive laws, kinematics, homogenization and multiscale methods in crystal plasticity finite-element modeling: Theory, experiments, applications. *Acta Materialia*, 58(4):1152–1211, feb 2010.

[59] Hans Ziegler. *An introduction to thermomechanics*, volume 21. Elsevier, 2012.

[60] William D Nix and Huajian Gao. Indentation size effects in crystalline materials: a law for strain gradient plasticity. *Journal of the Mechanics and Physics of Solids*, 46(3):411–425, 1998.

[61] R Hill, EH Lee, and SJ Tupper. The theory of wedge indentation of ductile materials. *Proc. R. Soc. Lond. A*, 188(1013):273–289, 1947.

[62] XR Wang, S Malang, AR Raffray, and LA El-guebaly. Modular dual coolant pb-17li blanket design for aries-cs compact stellarator power plant. In *Fusion Engineering 2005, Twenty-First IEEE/NPS Symposium on*, pages 1–4. IEEE, 2005.

[63] AR Raffray, L El-Guebaly, S Malang, I Sviatoslavsky, MS Tillack, X Wang, ARIES Team, et al. Advanced power core system for the aries-at power plant. *Fusion Engineering and Design*, 82(2):217–236, 2007.

[64] Dale L Smith, Charles C Baker, Dai Kai Sze, Grover D Morgan, MA Abdou, Steven J Piet, KR Schultz, Ralph W Moir, and James D Gordon. Overview of the blanket comparison and selection study. *Fusion Technology*, 8(1P1):10–44, 1985.

[65] W Krauss, J Konys, and A Li-Puma. Tbm testing in iter: Requirements for the development of predictive tools to describe corrosion-related phenomena in hcll blankets towards demo. *Fusion Engineering and Design*, 87(5-6):403–406, 2012.

[66] Shahram Sharafat, Aaron T Aoyama, and Nasr Ghoniem. Assessment of the dcll tbm thermostructural response based on iter design criteria. *Fusion Science and Technology*, 60(1):264–271, 2011.

[67] Francesco Romanelli, P Barabaschi, D Borba, G Federici, L Horton, R Neu, D Stork, and H Zohm. A roadmap to the realization of fusion energy. *EFDA, Garching, Germany*, 2012.

[68] A. Del Nevo, E. Martelli, P. Agostini, P. Arena, G. Bongiovì, G. Caruso, G. Di Gironimo, P.A. Di Maio, M. Eboli, R. Giammusso, F. Giannetti, A. Giovinazzi, G. Mariano, F. Moro, R. Mozzillo, A. Tassone, D. Rozzia, A. Tarallo, M. Tarantino, M. Utili, and R. Villari. WCLL breeding blanket design and integration for DEMO 2015: status and perspectives. *Fusion Engineering and Design*, 124:682–686, nov 2017.

[69] Emanuela Martelli A. Del Nevo. Integration for wcll in 2015 / ddd 2015 for wcll (update of ddd 2014). Design Description Document 2015 for WCLL (update of DDD 2014), 2015.

[70] IO ITER. Iter structural design criteria for in-vessel components (sdc-ic).

[71] Shahram Sharafat, Aaron T. Aoyama, and Nasr Ghoniem. Assessment of the DCLL TBM thermostructural response based on ITER design criteria. *Fusion Science and Technology*, 60(1):264–271, jul 2011.

[72] G Aiello, J Aktaa, F Cismondi, G Rampal, J-F Salavy, and F Tavassoli. Assessment of design limits and criteria requirements for eurofer structures in tbm components. *Journal of Nuclear Materials*, 414(1):53–68, 2011.

[73] MS Tillack, PW Humrickhouse, S Malang, and AF Rowcliffe. The use of water in a fusion power core. *Fusion Engineering and Design*, 91:52–59, 2015.

[74] JG Stone, R Schleicher, CP Deck, GM Jacobsen, HE Khalifa, and CA Back. Stress analysis and probabilistic assessment of multi-layer sic-based accident tolerant nuclear fuel cladding. *Journal of Nuclear Materials*, 466:682–697, 2015.

[75] CP Deck, GM Jacobsen, J Sheeder, O Gutierrez, J Zhang, J Stone, HE Khalifa, and CA Back. Characterization of sic–sic composites for accident tolerant fuel cladding. *Journal of Nuclear Materials*, 466:667–681, 2015.

[76] Lance L Snead, Takashi Nozawa, Yutai Katoh, Thak-Sang Byun, Sosuke Kondo, and David A Petti. Handbook of sic properties for fuel performance modeling. *Journal of nuclear materials*, 371(1-3):329–377, 2007.

[77] LL Snead, T Nozawa, Monica Ferraris, Y Katoh, R Shinavski, and M Sawan. Silicon carbide composites as fusion power reactor structural materials. *Journal of Nuclear Materials*, 417(1-3):330–339, 2011.

[78] Antonella Li-Puma, Marianne Richou, Philippe Magaud, Marc Missirlian, Eliseo Visca, and Vincenzo Pericoli Ridolfini. Potential and limits of water cooled divertor concepts based on monoblock design as possible candidates for a demo reactor. *Fusion Engineering and Design*, 88(9-10):1836–1843, 2013.

[79] M Rieth, JL Boutard, SL Dudarev, T Ahlgren, S Antusch, N Baluc, M-F Barthe, CS Becquart, L Ciupinski, JB Correia, et al. Review on the efda programme on tungsten materials technology and science. *Journal of Nuclear Materials*, 417(1-3):463–467, 2011.

[80] Marianne Richou, Antonella Li-Puma, and Eliseo Visca. Design of a water cooled monoblock divertor for DEMO using eurofer as structural material. *Fusion Engineering and Design*, 89(7-8):975–980, oct 2014.

[81] E Gaganidze, C Petersen, E Materna-Morris, C Dethloff, OJ Weiß, J Aktaa, A Povstyanko, A Fedoseev, O Makarov, and V Prokhorov. Mechanical properties and tem examination of rafm steels irradiated up to 70 dpa in bor-60. *Journal of Nuclear Materials*, 417(1-3):93–98, 2011.

[82] G. Aiello, J. Aktaa, F. Cismondi, G. Rampal, J.-F. Salavy, and F. Tavassoli. Assessment of design limits and criteria requirements for eurofer structures in TBM components. *Journal of Nuclear Materials*, 414(1):53–68, jul 2011.

[83] Farrokh Najmabadi, RW Conn, ARIES TEAM:, CG Bathke, L Bromberg, ET Cheng, DR Cohn, PIH Cooke, RL Creedon, DA Ehst, et al. The aries-i tokamak reactor study. *Fusion Technology*, 19(3P2A):783–790, 1991.

[84] Sebastian Ruck and Frederik Arbeiter. Thermohydraulics of rib-roughened helium gas running cooling channels for first wall applications. *Fusion Engineering and Design*, 109:1035–1040, 2016.